I. High Pressure Melting of γ-Iron and the Thermal Profile in the Earth's Core

II. High Pressure, High Temperature Equation of State of Fayalite (Fe_2SiO_4)

Thesis by

George (Guangqing) Chen

In Partial Fulfillment of the Requirements
for the Degree of
Doctor of Philosophy

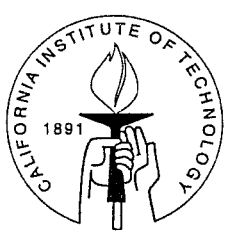

California Institute of Technology
Pasadena, California

1998

(Submitted August 11, 1997)

Acknowledgements

First of all, I'd like to thank my thesis advisor, Tom Ahrens, for his guidance, tolerance and support during my study and research at the Lindhurst shock-wave laboratory at Caltech. I am grateful for his giving me two very challenging and exciting research projects which constitute this thesis, as well as getting me interested in a variety of other topics. I have also benefited from interactions with other faculty members in several divisions, including Ed Stolper, John Beckett, Jeff Kimble, Tom Tombrello, Don Burnett, and James Knowles.

I'd also like to express my gratitude toward the technical staff of the lab, Papo Gelle, Mike Long, and Alberto Devora, without whose expertise and assistance this work would not be accomplished. I enjoyed many discussions with and benefited greatly from previous or current graduate students and visitors in the lab, including Tom Duffy, Jim Tyburczy, Greg Miller, Bill Anderson, Linda Rowan, Toshiko Takata, Wenbo Yang, Cangli Liu, Kathleen Holland, Raymond Hide and Satish Gupta. Sue Yamada and Margaret Vinci deserve special thanks for their diligent work.

I appreciate the collaboration of Mario Vassilliou who conducted the single crystal fayalite experiments and C. B. Finch at Oak Ridge National Laboratory who supplied the synthetic fayalite crystals. I thank John Beckett and Mike Baker for their help in fayalite synthesis and testing in furnaces, and Paul Carpenter and John Armstrong for their help in microanalysis of the samples. My office-mate Xiaoming Ding was constantly consulted on computer-related matters, and provided the PREM model in digital format.

My parents and my sister have always been extremely supportive and patient with me throughout my long study at Caltech, and offered good advice during difficult times. For the last two months of my work toward a Ph.D., I am also MBA (for Married But Apart). My thoughts are with my lovely wife Lilian, and I wish you will be with me soon.

Abstract

The melting curve of ϵ-iron in the pressure range of 100 to 300 GPa has been derived by computing Gibbs free energies at high pressures and high temperatures from thermodynamic and equations of state (EOS) data for the α-, ϵ- and liquid-phases. Our calculations indicate the melting curve of iron is very sensitive to the EOS of both the solid (ϵ) and melt phase. Our best estimate of the EOS parameters for ϵ-iron are: $\rho_0 = 8.775 \pm 0.012$ Mg/m^3, $K_{0T} = 205 \pm 4$ GPa, $K'_{0T} = 4.80 \pm 0.01$ (referenced to 12 GPa and 300 K). The calculation favors the melting curve of *Boehler* [1993] or *Saxena et al.* [1993]. Shock-wave experiments on pure iron preheated to 1573 K were conducted in 17–73 GPa range. The shock-wave equation of state of γ-iron at 1573 K initial temperature can be fit with $u_S = 4.102(0.015)$ km/s $+ 1.610(0.014)u_P$ with $\rho_0 = 7.413 \pm 0.012$ Mg/m^3. γ-iron's bulk modulus and its pressure derivative are 124.7±1.1 GPa and 5.44±0.06 respectively.

We present new data for sound velocities in the γ- and liquid-phases. In the γ-phase, to a first approximation, the longitudinal sound velocity is linear with respect to density: $V_p = -3.13(0.72) + 1.119(0.084)\ \rho$ (units for V_p and ρ are km/s and Mg/m^3 respectively). Melting was observed in the highest pressure (about 70–73 GPa) experiments at a calculated shock temperature of about 2775±160 K. This result is consistent with our calculated ϵ-iron melting curve which is close to those measured by *Boehler* [1993] and *Saxena et al.* [1993]. The liquid iron sound velocity data yield a Grüneisen parameter value for liquid iron of 1.63±0.28 at 9.37±0.02 Mg/m^3 at 71.6 GPa. The quantity $\gamma\rho$ from our data is 15.2±2.6 Mg/m^3, which is within the bounds of *Brown and McQueen* [1986] (13.3–19.6 Mg/m^3). Based on upward pressure and temperature extrapolation of our melting curve of γ-iron, the estimated inner core-outer core boundary temperature is 5500±400 K, the temperature at the core-mantle boundary on the outer core side is about 3930±630 K, and the thermal boundary layer at the core-mantle boundary has a temperature difference between 400 and 1400 K.

The shock-wave equation of state of initially solid (300 K) and molten (1573 K) fayalite (Fe_2SiO_4, Fa) are reported in the ranges 23 to 212 GPa and 5 to 47 GPa, respectively. The 300 K data appear to undergo a phase change in the 35–55 GPa range. The density of the high pressure phase (HPP) is consistent with a dense oxide mixture. Although the initially 300 K fayalite may melt along its Hugoniot, this is not explicitly detected. Fitting the HPP Hugoniot data in the shock velocity (u_S)-particle velocity (u_P) plane yields:

$$\rho_0 = 4.375(0.027)\ \mathrm{Mg/m^3}, \quad (1)$$

$$u_S = 4.07(0.22)\ \mathrm{km/s} + 1.43(0.06)\ u_P, \quad (2)$$

where ρ_0 is the initial density. The isentropic bulk modulus $K_{0S} = 72.4 \pm 8.0$ GPa, and its pressure derivative K'_{0S}=4.72±0.24.

The 1573 K data set yields:

$$\rho_0 = 3.750(0.018)\ \mathrm{Mg/m^3}, \quad (3)$$

$$u_S = 2.63(0.02)\ \mathrm{km/s} + 1.59(0.01)\ u_P, \quad (4)$$

and $K_{0S} = 25.9 \pm 0.4$ GPa, $K'_{0S} = 5.36 \pm 0.04$. The bulk modulus compares favorably with *Agee* [1992a]'s result (24.4 GPa), but the pressure derivative is quite different (10.1 from *Agee* [1992a]).

Above 50 GPa, the high pressure regime of the Hugoniot of the solid fayalite can be fit with oxide mixture models using stishovite and FeO (either LPP or HPP). The fayalitic liquid compression data above 40 GPa are well fit with ideal mixing of partial molar volumes of stishovite and FeO (LPP or HPP), in support of the hypothesis of *Rigden et al.* [1989].

A model basalt incorporating the liquid fayalite data shows the neutral buoyancy zone of basic silicate melts of plausible terrestrial compositions is at about 250–400

km depth based on the PREM Earth model.

Contents

List of Figures

List of Tables

Chapter 1 Introduction

1.1 Shock-Wave Experiments

High pressure properties of materials present a unique research field which is particularly interesting for geophysicists. The pressure at the center of the Earth is approximately 360 GPa, and at the core-mantle boundary (CMB) it is about 136 GPa. These pressures, when multiplied by the pressure-induced changes of atomic or ionic volumes in common minerals, give an energy on the order of an eV [*Bukowinski*, 1994]. This is comparable to typical molecular bond strengths, and valence electron energies. Hence pressure within the Earth, and the other terrestrial planets, may cause significant changes in valence electron orbitals, which may in turn affect the nature of bonding, structure, and physical properties of minerals. However, to seriously disrupt the shell structure of atoms, the pressure needed is in the order of 10 TPa. For example, the ground state energy of the hydrogen atom is 13.6 eV; divided by the Bohr volume, it yields the corresponding pressure of 14.7 TPa. Therefore, pressure-induced transitions are limited to the valence-shell modifications.

In the planetary interior, high pressures are accompanied by high temperatures. To free electrons from their ground states, the electron temperature needs to be on the order of 10^4 K as given by $kT \sim 1$ eV, where $k = 1.38 \times 10^{-23}$ J/K is the Boltzmann constant. Since the temperature throughout the Earth is well below 10^4 K, temperature has virtually no effect on the electronic structure of minerals within the Earth. However, the fraction of thermally excited electrons can contribute significantly to the specific heat of transition metals like iron [*Boness et al.*, 1986].

There are two complimentary experimental techniques in high pressure research: the diamond anvil cell (DAC) and shock-wave. The former allows static measurements on a variety of material properties, but is limited in sample size, is not reliable for pressures higher than ~70 GPa, and has problems achieving hydrostatic states at

above ~15 GPa. Heating in a DAC is possible by lasers or resistance, but temperature uniformity may be a problem; The latter permits relatively large samples on the order of centimeters and can reach high pressure (~ 300–400 GPa or higher) reliably, but because the dynamic nature of the experiments, the high pressure state is only maintained for a short time (on the order of microseconds). Besides high pressure study of material properties, shock-wave experiments have been used for a variety of applications; a few of which I have been involved with are (Appendix D): shock-induced chemical reactions, fracture and magnetization, impact-induced atmosphere depletion, and shock-wave attenuation.

In this thesis, I studied physical properties of two materials (iron and fayalite) of interest to geophysics under high pressures and high temperatures. First, the melting curve of iron under high pressures is directly related to the inner core-outer core temperature of the Earth as there are seismic evidences that the outer core is liquid and the inner core is solid. The iron's phase diagram is fairly well known only for the pressure range of about 0–50 GPa. Major disagreements (about 2000 K at 200 GPa) exist between results on the high pressure melting of iron from previous static [*Boehler*, 1993; *Saxena et al.*, 1993] and shock-wave measurements [*Brown and McQueen*, 1986; *Bass et al.*, 1987; *Yoo et al.*, 1993]. Consequently, their estimates for the Earth's temperatures at the inner core boundary (ICB) and outer core boundary (OCB) vary about 3000 and 1000 K, respectively.

In the second part, I report equation of state data of both solid and liquid fayalite, an end-member of upper mantle composition. Shock-wave equation of states of silicates, especially in their molten state, are essential to the understanding of both the evolution and the present structure of the Earth's mantle. Previously in our laboratory, *Rigden et al.* [1984, 1988], *Miller et al.* [1991a, b] and *Rowan* [1993] have investigated dynamic compression properties of various basaltic melts. This work is a continuation of the their work to evaluate the effect of the presence of ferrous iron in silicate melts.

1.2 Thesis Outline

The organization of the thesis is shown in Figure 1.1. There are two relatively independent parts: Shock-wave experiments on γ-iron centered at 1573 K, and shock-wave experiments on fayalite (solid and liquid). However, there are some common techniques shared between the two parts; they are included as Appendices A, B and C.

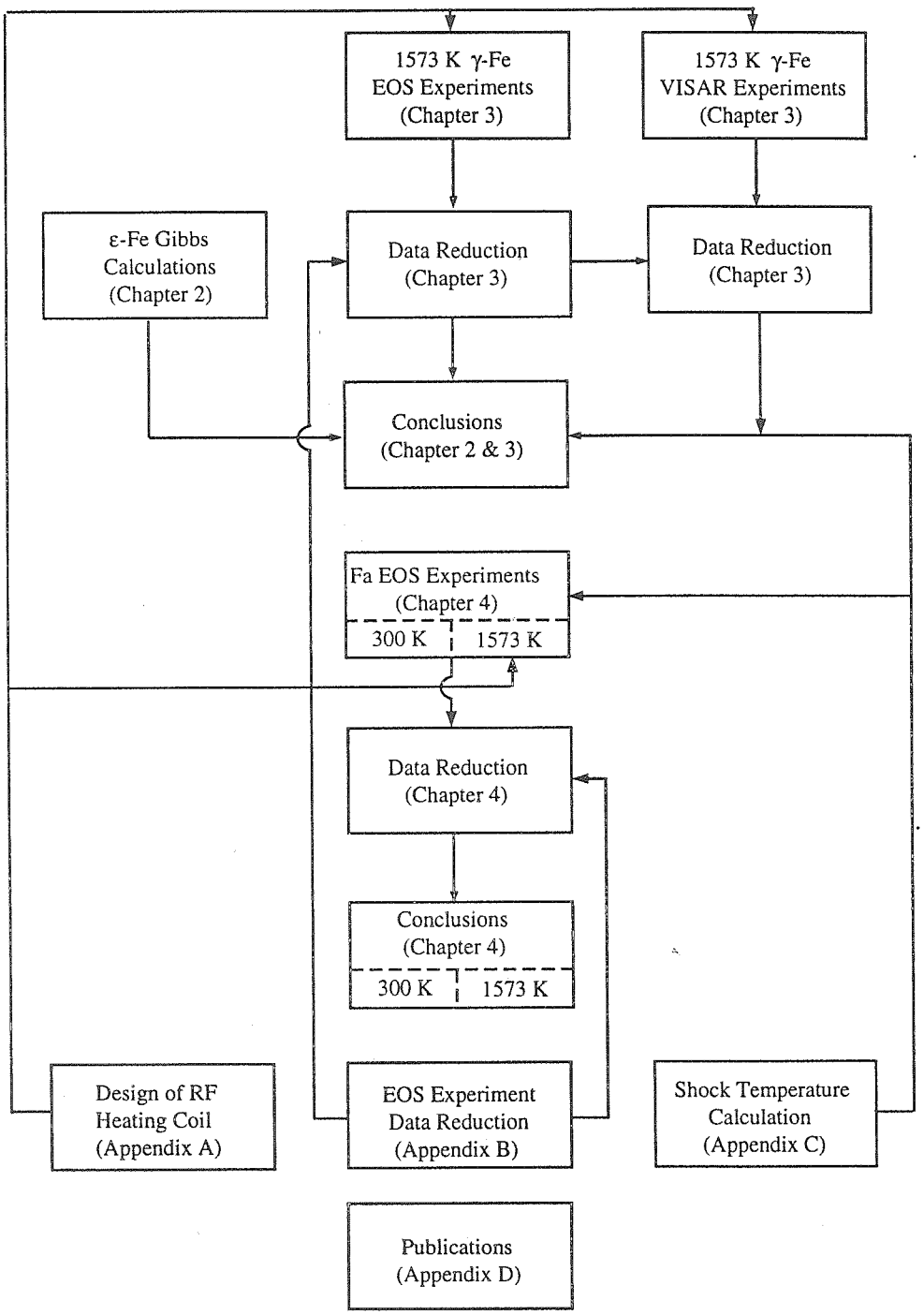

Figure 1.1: Organization of the thesis. The arrows show dependency between sections.

Chapter 2 Iron's Phase Diagram: Gibbs Free Energy Calculations

2.1 Abstract

The melting curve of ϵ-iron in the pressure range of 100 to 300 GPa has been derived by computing Gibbs free energies at high pressures and high temperatures from thermodynamic and equations of state (EOS) data for the α-, ϵ- and liquid-phases. Our calculations indicate the melting curve of iron is very sensitive to the EOS of both the solid (ϵ) and melt phase. Our best estimate of the EOS parameters for ϵ-iron are: $\rho_0 = 8.775 \pm 0.012$ Mg/m^3, $K_{0T} = 205 \pm 4$ GPa, $K'_{0T} = 4.80 \pm 0.01$ (referenced to 12 GPa and 300 K). The calculation favors the melting curve of *Boehler* [1993] or *Saxena et al.* [1993].

2.2 Introduction

Iron is considered to be the dominant component in both the liquid outer core and the solid inner core of the Earth; thus, the change in the melting temperature of iron with pressure is of considerable theoretical and experimental interest. Such a melting curve would provide a critical upper bound on the geotherm (the temperature as a function of depth) through the core. When corrected for the melting point depression resulting from the presence of impurities, the melting curve of iron-rich alloy represents a lower limit for the possible temperature distribution through the liquid outer core. The melting curve also gives an absolute upper limit on the temperature at the inner core-outer core boundary. As the inner core is likely to be nearly isothermal, the temperature at the inner core boundary may be taken, within present uncertainties, as a good approximation to that at the center of Earth.

In the P-T phase diagram of iron, phase boundaries are fairly well known only for the pressure range of about 0–20 GPa. The α (bcc) to ϵ (hcp) phase transition was discovered by *Bancroft et al.* [1956] using shock-wave methods, later studies [*Huang et al.*, 1987; *Akimoto et al.*, 1987; *Manghnani et al.*, 1987] established the details of the α-ϵ fields. The γ (fcc) phase transition and the α-γ-ϵ triple point was studied by *Bundy* [1965], *Omel'chenko et al.* [1969], *Mirward and Kennedy* [1979], *Boehler et al.* [1989] and *Besson and Nicol* [1990]; the γ-δ (bcc)-liquid triple point and melting at low pressures (below 5.2 GPa) was studied by *Strong et al.* [1973], among others. However, major disagreement exists between the extrapolation to high pressure of the melting curve of iron from previous static measurements (at up to 200 GPa) [*Boehler*, 1993; *Saxena et al.*, 1993], and the higher pressure (180–350 GPa) shock-wave measurements [*Brown and McQueen*, 1986; *Bass et al.*, 1987; *Yoo et al.*, 1993]. The difference is examined in detail in Figures 2.1 and 2.2.

2.2.1 The Higher Melting Curve

In Figure 2.1, results from *Williams et al.* [1987], *Yoo et al.* [1993], *Anderson and Ahrens* [1996] and *Brown and McQueen* [1986], which all agree on a relatively high melting curve, are shown. The *Williams et al.* [1987] data, which are most cited to represent this group, are a compilation of data from static heating in a diamond cell and shock temperature measurements [*Bass et al.*, 1987]. *Anderson and Ahrens* [1996]'s melting curve is based on the same *Bass et al.* [1987] data but used a different analyzing method. *Yoo et al.* [1993]'s melting curve is based on shock temperature measurements from about 180–350 GPa (melting occurs at about 6350 K and 235 GPa). The two open squares in Figure 2.1 are calculated shock temperatures of two discontinuities in the sound velocity measurements of *Brown and McQueen* [1986] along the principal Hugoniot. They interpreted the first discontinuity as the solid-solid phase change from the ϵ-phase to the γ-phase, and the second discontinuity as the melting of the γ-phase.

The γ-ϵ-liquid triple point is determined at about 330 GPa and 7500 K [*Williams*

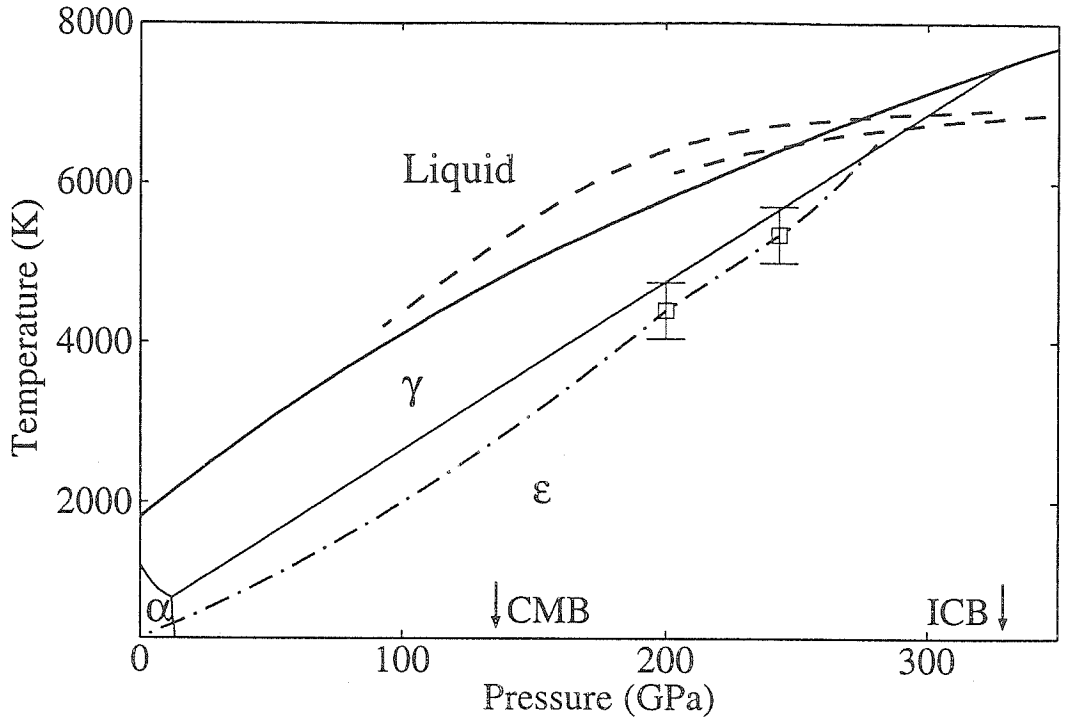

Figure 2.1: *Williams et al.* [1987] (heavy solid curves) and other researchers' phase diagram with a high temperature melting curve. The ϵ-γ phase boundary is from *Williams et al.* [1991]. Upper dashed line is from *Anderson and Ahrens* [1996], lower dashed line is from *Yoo et al.* [1993]. Dash-dotted line is calculated Hugoniot temperature of *Brown and McQueen* [1986]. Open squares indicate two sound velocity discontinuities in *Brown and McQueen* [1986]'s work. CMB marks the core-mantle boundary pressure (136 GPa), and ICB is the inner core boundary (329 GPa).

et al., 1991] to accommodate *Brown and McQueen* [1986]'s interpretation of the first discontinuity. Even so, there is still considerable discrepancy between *Brown and McQueen* [1986]'s shock temperature calculation and the measured shock temperatures at 200 and 243 GPa, at which the phase changes are expected to take place. Recently *Holland* [1997] found that the anvil material (Al_2O_3 and LiF) used in *Williams et al.* [1987]'s shock temperature experiments has lower thermal conductivity under high pressures than previously assumed, and the previous data could have been over-corrected for thermal diffusion and thus were too high. Their latest shock temperature measurements indicate a melting temperature which is compatible with that of *Brown and McQueen* [1986]. This work may provide an explanation to the internal inconsistency of the shock-wave measurements.

2.2.2 The Lower Melting Curve

A melting curve at considerably lower temperatures (by about 2000 K at 200 GPa, Figure 2.2) has been proposed by *Boehler* [1993] and *Saxena et al.* [1994], using diamond anvil cell (DAC) techniques. There are slight differences in the melting curve and the location of the γ-ϵ-liquid triple point, but the differences are small compared with those of the first group of researchers. Besides the lower temperature melting curve, the most striking feature in their phase diagram is the β-phase between the ϵ and the liquid phases [*Boehler*, 1993; *Saxena et al.*, 1993, 1995, 1996], which is proposed to have a double hcp structure [*Saxena et al.*, 1996]. Evidence for this phase includes a discontinuity in temperature rise with increasing laser power in a heated DAC [*Saxena et al.*, 1993], and X-ray diffraction studies [*Saxena et al.*, 1995, 1996]. *Boehler* [1993] attempted to attribute *Brown and McQueen* [1986]'s first discontinuity to the ϵ-β phase change, but as shown in Figure 2.2, the difference in temperature is not compatible with the explanation. Recently based on heated DAC experiments, *Yoo et al.* [1995] suggested a new ϵ' phase in the γ stability field (centered at about 40 GPa and 1500 K), but this result is more controversial than the existence of the β phase [*Saxena and Dubrovinsky*, 1997].

There is yet a third explanation for the first discontinuity observed by *Brown and McQueen* [1986]. *Belonoshko* [1997] suggested, based on molecular dynamics simulations, that it is related to melting instead of a separate phase change. This interpretation is also highly speculative.

In this chapter we attempt to theoretically determine the melting curve of iron from equations of state of the α-, ϵ- and liquid-phases by minimizing the Gibbs free energy in a thermodynamically consistent manner. The benefit of this approach can be twofold: (1) it is expected to yield results which demonstrate which of the previous high pressure melting curves are consistent with available thermodynamic and equations of state data, and (2) the calculations highlight thermodynamic quantities which need to be better determined in order to further constrain the melting curve.

The next chapter describes shock-wave experiments on preheated iron samples.

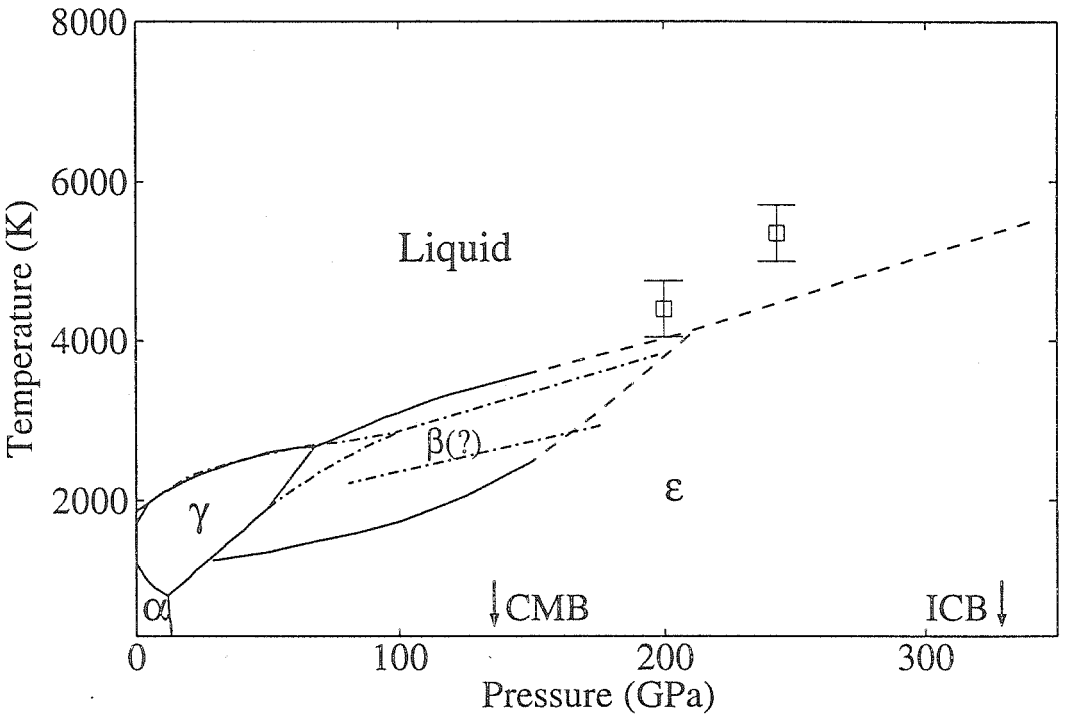

Figure 2.2: *Saxena et al.* [1994] (solid and dashed lines) and *Boehler* [1993] (dash-dotted lines)'s phase diagrams with a low temperature melting curve and a dhcp β phase. Dashed lines are extrapolations of *Saxena et al.* [1994]'s data below 150 GPa. Open squares indicate two sound velocity discontinuities in *Brown and McQueen* [1986]'s work.

We determined the initial density, shock-wave velocity and particle velocity in pre-heated (1573 K) iron using the equations of state (EOS) methods pioneered by *Rigden et al.* [1984]. Using our Velocity-Interferometer-System-for-Any-Reflector (VISAR) system we also measured compressional-wave velocity in shock compressed iron in the 17–73 GPa pressure range. The compressional-wave velocity provides an excellent diagnostic to detect melting under high pressures [*Brown and McQueen*, 1986; *Duffy and Ahrens*, 1994a, b]. Starting from the pre-shock temperature of 1573 K, upon shock pressure to 73 GPa, sound velocities are measured which are comparable with that expected from interpolation between the high pressure data of *Brown and McQueen* [1986], and 1 bar, high-temperature sound velocity measurement on liquid iron [*Nasch et al.*, 1994; *Kurz and Lux*, 1969; *Tsu et al.*, 1985]. In pressure-temperature (P-T) space the experiments described in the next chapter are compatible with the present theoretically derived melting curve.

2.3 Gibbs Free Energy Calculations

Two sets of equations are used in calculating Gibbs free energy (G) of a single phase as a function of P and T. These are discussed separately in the sections below. The two methods are thermodynamically equivalent. The first method is more convenient for equations of states given in terms of isothermal bulk modulus, K_{0T}, and its pressure derivative, K'_{0T} (*e.g.*, assuming data for α- and ϵ-phases from static isothermal experiments). The second method employs an EOS given in terms of the equivalent isentropic parameters K_{0S} and K'_{0S} (liquid iron phase). Here the subscripts T and S indicate isothermal and isentropic conditions. The equations of state of the three phases are listed in Table 2.1.

2.3.1 Calculation Using an Isotherm-Isobar Mesh

Gibbs energies of the α- and ϵ-phases of iron are calculated with this method. For parameters related to the two phases, refer to Sections 2.3.3 and 2.3.4.

Table 2.1: Optimal EOS for α-, ϵ- and liquid iron

Phases	Reference state[1]	Equation of state
α[2]	$P_0 = 1$ bar, T_0=300 K	$K_{0T} = 171$ GPa, $K'_{0T} = 4.0$
	$\rho_0 = 7.875$ Mg/m^3	α and C_P data are after
	$H_0 = 0$, $S_0 = 0$	*Robie et al.* [1979], $\delta = 4.0$
ϵ[3]	$P_0 = 12$ GPa, T_0=300 K	$K_{0T} = 205$ GPa, K'_{0T}=4.8,
	$\rho_0 = 8.775$ Mg/m^3	$\alpha_0 = 3 \times 10^{-5}$ K^{-1}
	$H_0 = 8.144 \times 10^4$ J/mol	$\beta = 2 \times 10^{-5}$ K^{-1}, $\delta = 3.2$
	$S_0 = -2.54$ J/K/mol	$C_V = c(C_l + C_e)$, $c = 0.98 - 0.3 \times (T - 273)/5000$
Liquid[4]	$P_0 = 1$ bar, T_0=1809 K	$K_{0S} = 109.7$ GPa, K'_{0S}=4.661
	$\rho_0 = 7.019$ Mg/m^3	$\gamma = 1.735 - 0.13 \times (\rho/\rho_0)^{-1.87} E$
	$H_0 = 7.21 \times 10^4$ J/mol	$C_V = C_k + C_{pot} + C_e$[5]
	$S_0 = 72.3$ J/K/mol	

1. H_0, S_0 are relative to α-phase at 300 K, 1 bar.
2. *Huang et al.* [1987].
3. This study.
4. *Anderson and Ahrens* [1994].
5. For exact forms of C_l, C_e, C_k and C_{pot}, see Equation 2.15 and *Anderson and Ahrens* [1994].

This approach was used by *Song and Ahrens* [1994] to evaluate the possibility of reactions between liquid iron in the outer core and silicates in lower mantle. In that paper, at any given pressure and temperature, Gibbs energies for the reactants and products were calculated and compared to determine the direction of reaction. Here we calculate and explicitly compare Gibbs energies of iron in different phases: the one that is lowest is the equilibrium phase under pressure P and temperature T. $G(P,T)$ is calculated from reference point $G(P_0,T_0)$, by first moving along the isobar to (P_0,T), then along the isotherm to the final state (P,T):

$$G(P,T) = H(P_0,T) - TS(P_0,T) + \int_{P_0}^{P} V(P',T)dP', \tag{2.1}$$

where the first two terms are

$$H(P_0,T) = H(P_0,T_0) + \int_{T_0}^{T} C_P(P_0,T')dT' \tag{2.2}$$

$$S(P_0,T) = S(P_0,T_0) + \int_{T_0}^{T} \frac{C_P(P_0,T')}{T'} dT' \tag{2.3}$$

$H(P_0,T_0)$ and $S(P_0,T_0)$ are enthalpy and entropy of the stable phase at the reference state (P_0, T_0), V and C_P are volume and specific heat at constant pressure.

For the last term on the right-hand side of Equation 2.1, $V(T,P')$ is again calculated on the P'-T mesh: First, $V(T_0,P')$ is calculated from, *e.g.*, third order Birch-Murnaghan equation of state

$$\begin{aligned} P' &= P_0 + \frac{3}{2}K_{0T}\left\{\left[\frac{V(P_0,T_0)}{V(P',T_0)}\right]^{7/3} - \left[\frac{V(P_0,T_0)}{V(P',T_0)}\right]^{5/3}\right\} \\ &\quad \times(1+\frac{3}{4})(K'_{0T}-4)\left[\left(\frac{V(P_0,T_0)}{V(P',T_0)}\right)^{2/3} - 1\right] \end{aligned} \tag{2.4}$$

given the volume, isothermal bulk modulus K_{0T} and its derivative K'_{0T} at the reference state (Table 2.1). Then it undergoes thermal expansion to the final state:

$$V(P',T) = V(P',T_0)\exp\left[\int_{T_0}^{T}\alpha(P',T')dT'\right]. \tag{2.5}$$

The thermal expansion coefficient $\alpha(P',T')$ is usually experimentally determined only at P' =1 bar. The pressure dependency assumed is:

$$\alpha(P',T') = \alpha(P_0,T')\left[\frac{V(P',T')}{V(P_0,T')}\right]^{\delta}, \tag{2.6}$$

where δ is the second Grüneisen parameter which is taken to be constant (see Table 2.1 for values).

For ϵ-iron, the temperature dependence of the thermal expansion coefficient is assumed to be linear with temperature at 1 bar:

$$\alpha(P_0,T') = \alpha(P_0,T_0)[1+\beta(T'-T_0)]. \tag{2.7}$$

The calculation is carried out numerically on a $N_P \times N_T$ mesh in the P-T space:

$P_i = P_0 + i \times \Delta P$, $T_j = T_0 + j \times \Delta T$ (i, j are indices of nodes). Evaluating Equations 2.1 to 2.5 numerically is fairly straightforward; For Equation 2.6, one needs to know $V(P' = P_i, T' = T_j)$, which requires $\alpha(P' = P_i, T' = T_j)$ to be known beforehand. Although the problem may be solved by iteration (together with Equation 2.5), we use an approximate solution for $\alpha(P', T')$ from $V(P_{i-1}, T_j)$ (which has been calculated at this point):

$$\alpha(P_i, T_j) = \alpha(P_0, T_j) \left[\frac{V(P_{i-1}, T_j)}{V(P_0, T_j)} \right]^{\delta}. \tag{2.8}$$

2.3.2 Calculation Using an Isentrope-Isometric Mesh

The calculation of the Gibbs energy of liquid iron employs:

$$G(P,T) = E(P,T) - TS(P,T) + PV(P,T). \tag{2.9}$$

At any P and T, E, S and V are calculated by first moving along an isentrope from (P_0, T_0) to (P_S, T_S), at which the internal energy is E_S and volume is $V_S (= V)$:

$$E_S(P_S) = E(P_0, T_0) - \int_{V_0}^{V_S} P_S dV \tag{2.10}$$

$$T_S(P_S) = T_0 \exp\left[- \int_{V_0}^{V_S} \left(\frac{\gamma}{V} \right) dV \right] \tag{2.11}$$

where V_S is again determined by third order Birch-Murnaghan EOS (same as Equation 2.4 except that K_{0T} and K'_{0T} in the equation are replaced with isentropic bulk modulus K_{0S} and its pressure derivative K'_{0S}). γ is the Grüneisen parameter for liquid iron; it has been fit as a function of internal energy (*Anderson and Ahrens* [1994], the exact form is in Table 2.1), *i.e.*, in Equation (2.11), $\gamma = \gamma(E_S)$. The integral can then be evaluated noting along the isentrope, $dE_S = -P_S dV$.

The second step is to move along an iso-volumetric line from (P_S, T_S) to (P, T). With $V(P,T)$ held at constant V_S, either P or T are variable. We treat the isentropic pressure P_S and final pressure P as dependent parameters. Therefore, $T = T(P, P_S)$.

The internal energy of the final state (E) is given by solving the Mie-Grüneisen equation:

$$\int_{E_S}^{E} \gamma(E')dE' = V_S(P - P_S), \tag{2.12}$$

then the following equation is solved for T:

$$\int_{T_S}^{T} C_V(T', V_S)dT' = E - E_S, \tag{2.13}$$

and S is

$$S = S_0 + \int_{T_S}^{T} \frac{C_V(T', V_S)}{T'}dT'. \tag{2.14}$$

Equations 2.12–2.14 give all the thermodynamic quantities needed to evaluate Equation 2.9, given values for K_{0S}, K'_{0S}, C_V and γ.

2.3.3 Gibbs Energy of α- and Liquid Iron

Huang et al. [1987] reported α-iron high-pressure compression data to 12.4 GPa with a reference state at 1 bar and 300 K. We used *Robie et al.* [1979]'s experimental α-iron C_P data (alternatively one can estimate theoretically by summing lattice, magnetic and electronic contributions [*Kerley*, 1993]).

For liquid iron, the reference state is at the melting point (1809 K) at 1 bar. H_0 and S_0 are calculated from the values of the α-phase at the same pressure and temperature, and the enthalpy change upon melting. We used the EOS parameters of liquid iron in *Anderson and Ahrens* [1994] (Table 2.1). This equation of state was obtained based on data from a wide range of experiments: ultrasonic, thermal expansion, and enthalpy data at 1 bar, pulse heating, shock-wave compression and sound velocity from STP to 10^3 GPa and 8000 K.

2.3.4 Gibbs Energy of ϵ-Iron

K_{0T} and K'_{0T} for ϵ-iron are obtained from analysis of X-ray diffraction under static compression [*Huang et al.*, 1987; *Mao et al.*, 1990]. Thermal expansion coefficient is poorly constrained; previous estimates from static experiments exist in the 150–450°C, 10–20 GPa region ($\sim$ 3–5$\times 10^{-5}$ K^{-1} [*Huang et al.*, 1987]), shock-wave data yield a mean value of α from 300 to $\sim$5200 K at 202 GPa ($\sim 9 \times 10^{-6}$ K^{-1} [*Duffy and Ahrens*, 1993]). They were used to constrain the pressure dependency of thermal expansion (Equation 2.8).

No experimental data is available for the specific heat of ϵ-iron. We calculated C_V by summing the contributions from the lattice (given by the Debye model) and from the electrons. For the electronic contribution (C_e), we adopted the theoretical results of *Boness et al.* [1986]. We assumed the following value for C_V:

$$C_V(P,T) = c\left[9R \times D\left(\frac{T_D}{T}\right) + C_e\right], \tag{2.15}$$

where D is the Debye function, and Debye temperature for ϵ-iron is 385 K [*Andrews*, 1973; *Kerley*, 1993]. Here c is an *ad hoc* parameter: if our model is correct, c is unity.

C_P is then calculated from C_V from the thermodynamic identity:

$$C_P = C_V + \alpha^2 V K_{0T} T. \tag{2.16}$$

The reference state is chosen to be (12 GPa, 300 K), at which the α-phase transforms to the ϵ-phase. The entropy change of the transition, ΔS, at 300 K is unknown, but from the Clausius-Claperon relation:

$$\Delta S = \Delta V \frac{dP}{dT}, \tag{2.17}$$

ΔV is the volume change during the α-γ phase change at 300 K [*Huang et al.*, 1987], $\frac{dP}{dT}$ is the slope of the phase boundary in P-T plane (reviewed by *Besson and Nicol* [1990]); and it is estimated the enthalpy change $\Delta H = T\Delta S$ is no more than $\sim$ 0.6 kJ/mol, or about 5% of the enthalpy increase of iron upon melting under 1 bar. In

absence of more accurate data, we set ΔH to zero in our calculations.

2.3.5 Melting Curve Between the ϵ- and Liquid Phases

After the Gibbs energies of the ϵ- and liquid-phases (G_ϵ and G_l) are calculated independently, the melting temperature is defined as the intersection of the two curves of Gibbs energy versus temperature at constant pressure. We keep the α- and liquid-phases EOS fixed and adjust the ϵ-phase EOS to fit experimentally determined melting curves [*Boehler*, 1993; *Saxena et al.*, 1993; *Williams et al.*, 1991]. The results are shown in Figures 2.3 to 2.5.

In the following sections we discuss the effects of various parameters (C_P, K_{0T}, α) of the ϵ-phase which are not well determined from experiments.

Specific Heat

We vary C_P by changing the parameter c in Equation 2.15. It has a pronounced effect on the slope of the $G_\epsilon(T)$ at a given pressure. The effect is nearly the same at different pressures. At c=1 (the theoretical value), $G_\epsilon(T)$ drops faster than $G_l(T)$ at higher pressures (200–300 GPa) such that they may never intersect. This is in clear contradiction with experimental data. The deviation of c from 1 indicates large anharmonicity in the close packed ϵ-phase or uncertainty in determination of the electronic specific heat.

Bulk Modulus

The bulk modulus controls the slope of $G_\epsilon(P)$ versus P at a given temperature. The effect decreases with increasing T due to K_{0T}'s temperature dependence, so K_{0T} also affects the slope of $G_\epsilon(T)$, though much less directly than C_P does. The effect can further be refined by varying K'_{0T} as discussed in Section 2.3.6.

Thermal Expansion

α has a similar effect on $G_\epsilon(P)$ at fixed pressures as C_P (lower values of α give steeper $G_\epsilon(P)$ versus T curves), but the change of slope has much stronger pressure dependence than that caused by C_P. Again, the effect can be subtly controlled with α's temperature dependence and pressure dependence as specified by Equations 2.6 and 2.7.

2.3.6 *P-T* Phase Diagrams of Iron

The diamond-anvil melting curves [*Boehler*, 1993; *Saxena et al.*, 1993] agree closely regarding the solid-liquid stability field (although they disagree about the stability region of a proposed, new β-phase; see Figure 2.2). *Saxena et al.* [1994] proposed the phase diagram shown in Figure 2.2 based on their experimental data and thermodynamic calculations similar to the present ones. Shock-wave data [*Bass et al.*, 1987; *Yoo et al.*, 1993] approximately agreed on a higher melting curve obtained completely or partially (data from *Bass et al.* [1987] are incorporated in *Williams et al.* [1991]). Recently *Anderson and Ahrens* [1996] revised shock temperature calculations of *Bass et al.* [1987] which derived a lower melting point at high pressures ($>$ 230 GPa), but not low enough to explain the difference between the extrapolated (low pressure) static melting curves and *Bass et al.* [1987]'s (high pressure) shock-wave data. The origin of the solid-solid transformation observed in the principal Hugoniot (at $\sim$ 200 GPa [*Brown and McQueen*, 1986]) before melting (at $\sim$ 243 GPa) is uncertain. Brown and McQueen interpreted it as the ϵ-γ transition (Figure 2.1), while *Boehler* [1993] believed it is between ϵ and β. *Anderson* [1994] offered a third scenario by suggesting yet another solid phase θ above 200 GPa and 4000 K. Structural studies of the β-phase are inconclusive. *Matsui* [1992] suggested it should have a body centered cubic (bcc) structure from his molecular simulations, but *Stixrude and Cohen* [1995] concluded bcc structure is unstable in the $\sim$ 150 GPa range from density functional theory. *Saxena et al.* [1996] suggested it has the double hcp structure. It is likely there is at least one phase between the ϵ and liquid stability fields in the pressure

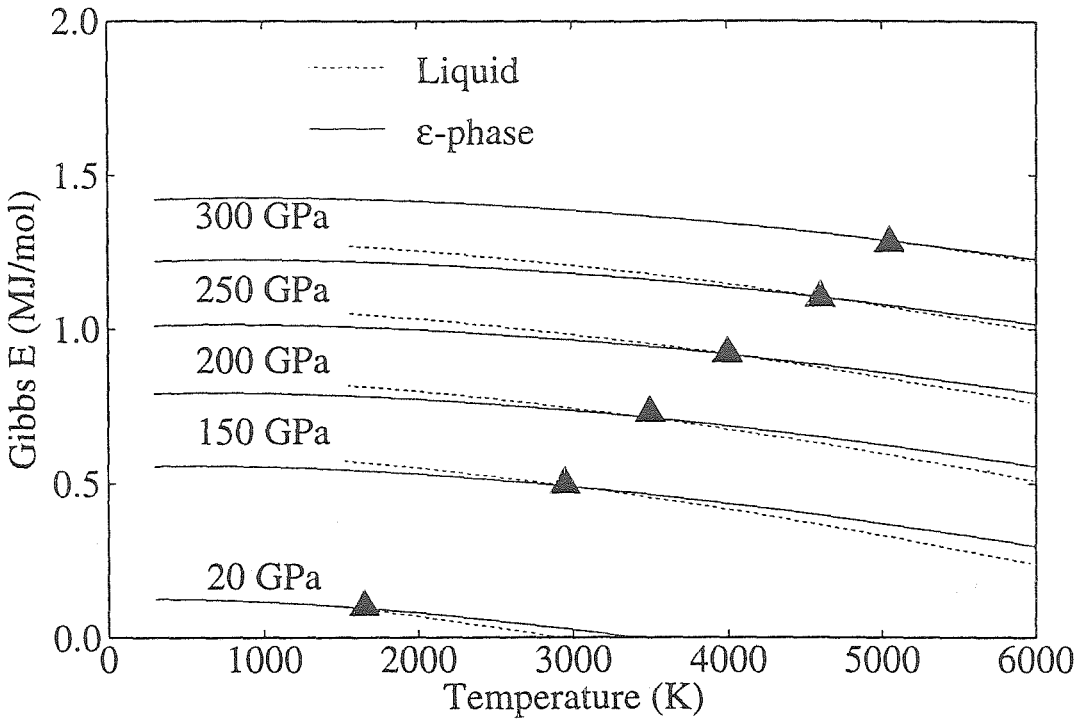

Figure 2.3: Gibbs free energies of the ϵ- and liquid iron as functions of pressure. Their intersections (melting points) change as we use the three sets of EOS parameters in Table 2.1 for ϵ-iron: Intersections are close to *Boehler* [1993]'s melting curve.

range of 100–300 GPa, but the EOS of the phase is unknown and hence calculating its fusion curve is infeasible. If such a phase does exist, the melting temperature of iron in this new phase should be higher than that of the ϵ-iron which is calculated here.

Our best estimate of the ϵ-liquid-phase line calculated from thermodynamic and equation of state data is given in Figure 2.6 and Table 2.1. Uncertainties in the ϵ-phase equation of state are difficult to estimate. The most critical parameters are the bulk modulus of the reference state, specific heat (characterized by c in Equation 2.15), and the thermal expansion coefficient. If we constrain the melting point at 300 GPa to within 300 K of our best fit, the tolerances on these three quantities are about 4 GPa, 0.01, and 3×10^{-6} K^{-1}, respectively.

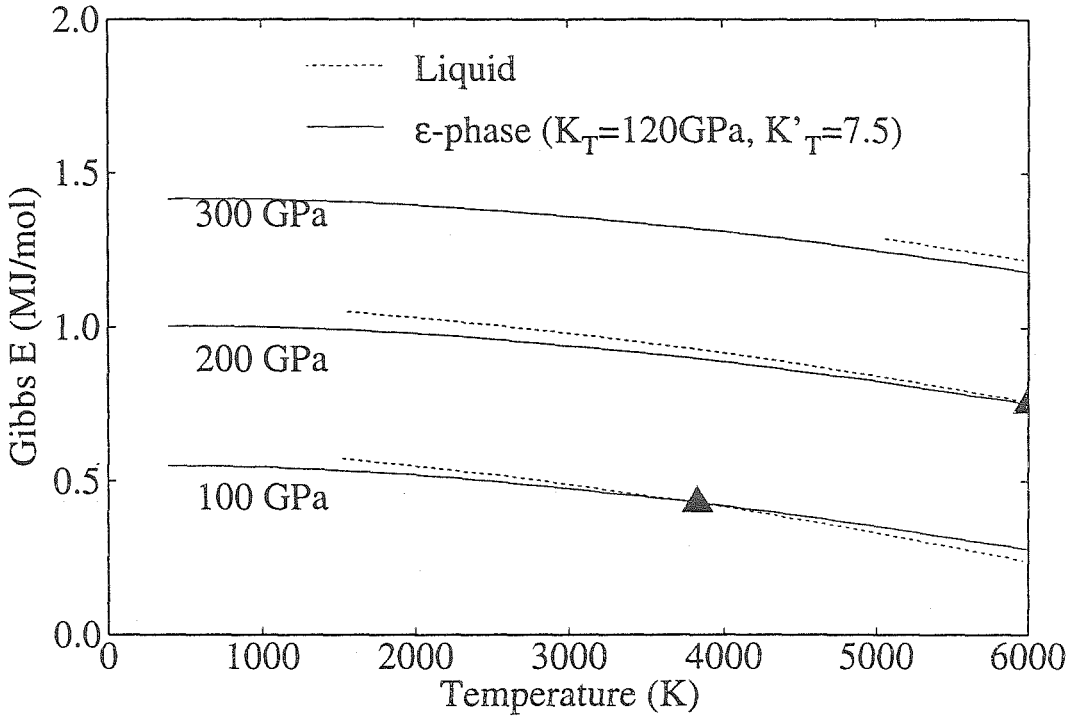

Figure 2.4: Gibbs free energies calculation to fit *Williams et al.* [1987]'s melting curve.

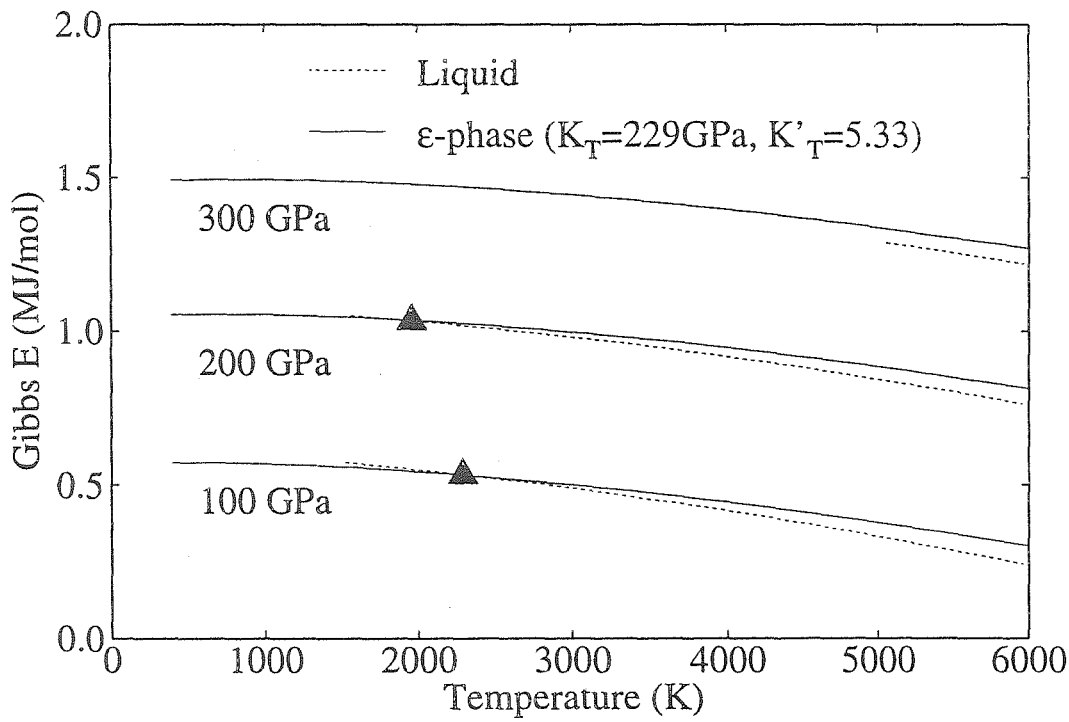

Figure 2.5: Gibbs free energies calculation using *Mao et al.* [1990]'s experimental compression data for ϵ-iron.

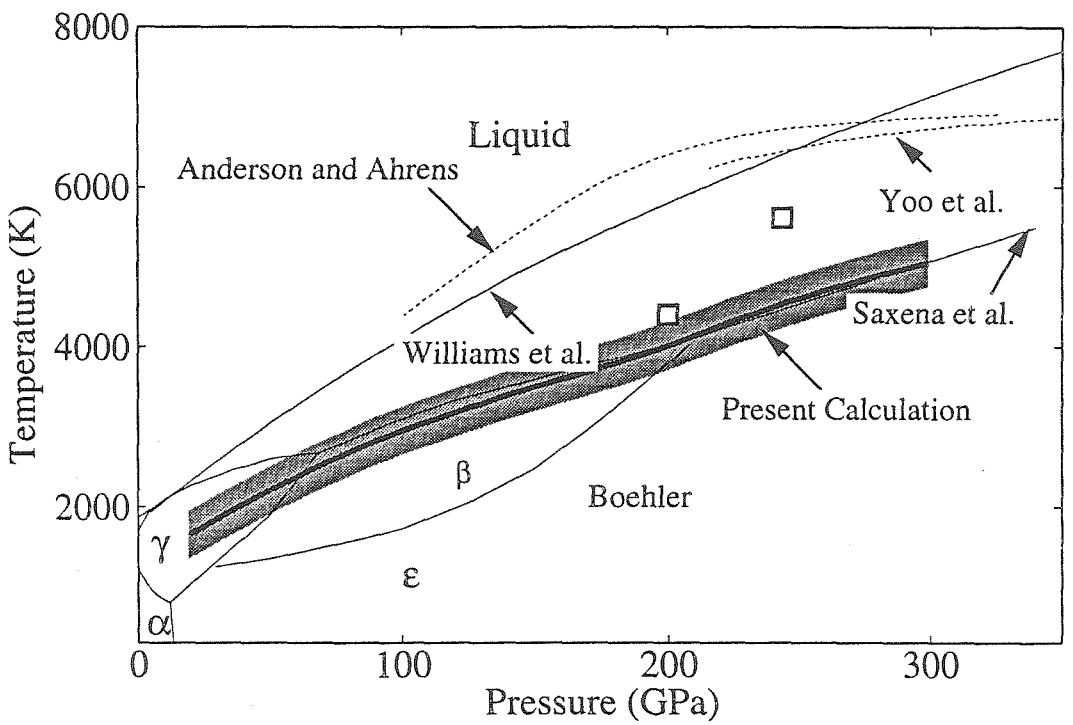

Figure 2.6: Present calculated ϵ-iron melting curve (heavy solid curve) in comparison to previously suggested phase diagrams. The gray band represents changes of Gibbs energy caused by varying parameters K_{0T}, c, and α by 4 GPa, 0.01, and 3×10^{-6} K^{-1} respectively from the optimal values for ϵ-iron in Table 2.1. *Boehler* [1993] and *Saxena et al.* [1993]'s melting curves are very close and are plotted and labeled collectively as "Saxena et al." The two squares at 200 and 243 GPa are calculated shock temperatures of solid-solid transition and melting along the principal Hugoniot of *Brown and McQueen* [1986] (the complete Hugoniot is shown in Figure 2.1).

2.4 Conclusion

The ϵ-liquid melting curve of iron presented in Figure 2.6 is in good agreement with *Boehler* [1993] and *Saxena et al.* [1993]'s data. The value of K_{0T} of ϵ-iron at 12 GPa and 300 K which will give a melting line in approximate agreement with *Boehler* [1993]'s data is 205 GPa (Table 2.1), significantly lower than the 264 GPa (with K'_{0T}=5) reported by *Huang et al.* [1987]. The 205 GPa bulk modulus value is closer to 229 GPa which was measured by *Mao et al.* [1990]. Mao's data, however, yields a melting curve too low in the 100–300 GPa range (Figure 2.5). Interestingly, values of $K_{0T} \simeq 120$ GPa and K'_{0T}=7.5 for ϵ-iron are required to fit *Williams et al.* [1987]'s data. Therefore, assuming the phase diagram and the equations of state of the α- and liquid-phases are approximately correct, our calculations favor *Saxena et al.* [1993] and *Boehler* [1993]'s melting curve over that of *Williams et al.* [1991]. Finally, in either fit, the specific heat of the ϵ-phase is lower than the theoretical value derived by *Boness et al.* [1986] ($c < 1$ in Equation 2.15).

Although we cannot completely delineate the effects of all variables on the Gibbs energy of the ϵ-phase, we note that to fit the *Williams et al.* [1991]'s data, the bulk modulus must be lowered to fit the melting point at 100 GPa ($\sim$4000 K). Although steepening the Gibbs energy temperature dependence (by, *e.g.*, increasing the value of C_P) would also raise the melting point at 100 GPa, it yields too high a melting point at 200 GPa. More experimental data on the β- and ϵ-phases (especially to better define the existence of the β-phase and to determine the ϵ-phase's thermal expansion coefficient) would lead to more definite conclusions from calculations such as presented here.

Chapter 3 Sound Velocities of γ- and Liquid-Iron Under Dynamic Compression

3.1 Abstract

Shock-wave experiments on pure iron preheated to 1573 K were conducted in 17–73 GPa range. The shock-wave equation of state of γ-iron at 1573 K initial temperature can be fit with $u_S = 4.102(0.015)$ km/s + $1.610(0.014)u_P$ with $\rho_0 = 7.413 \pm 0.012$ Mg/m^3. γ-iron's bulk modulus and its pressure derivative are 124.7±1.1 GPa and 5.44±0.06 respectively.

We present new data for sound velocities in the γ- and liquid-phases. In the γ-phase, to a first approximation, the longitudinal sound velocity is linear with respect to density: $V_p = -3.13(0.72) + 1.119(0.084)\ \rho$ (units for V_p and ρ are km/s and Mg/m^3 respectively). Melting was observed in the highest pressure (about 70–73 GPa) experiments at a calculated shock temperature of about 2775±160 K. This result is consistent with our calculated ϵ-iron melting curve which is close to those measured by *Boehler* [1993] and *Saxena et al.* [1993]. The liquid iron sound velocity data yield a Grüneisen parameter value for liquid iron of 1.63±0.28 at 9.37±0.02 Mg/m^3 at 71.6 GPa. The quantity $\gamma\rho$ from our data is 15.2±2.6 Mg/m^3, which is within the bounds of *Brown and McQueen* [1986] (13.3–19.6 Mg/m^3). Based on upward pressure and temperature extrapolation of our melting curve of γ-iron, the estimated inner core-outer core boundary temperature is 5500±400 K, the temperature at the core-mantle boundary on the outer core side is about 3930±630 K, and the thermal boundary layer at the core-mantle boundary has a temperature difference between 400 and 1400 K.

3.2 Preparation

The pure iron targets are in a single machined disk shape, the "driver plate" is 2 mm thick and 38 mm in diameter, the central "top hat" is 4 mm thick and 13 mm in diameter (Figure A.2). The target is heated via an induction coil (Appendix A) placed around the top hat. The temperature is monitored until just before impact with a two-color infrared pyrometer (Williamson 8120S-C-WD2) which in turn was calibrated against a thermocouple (Figure 3.1).

Two dual-color pyrometers (Williamson 8120S-C-WD2 (temperature range: 1000–2000°C, used in the experiments) and Ircon R-20C10-0-0-0-00-0/000) have been calibrated in a Deltech furnace against a Pt-Pt/10%Rh thermocouple. The pure iron target was placed in a CO_2-H_2 gas flow such that iron was stable in the temperature range of the measurements (1306–1673 K from thermocouple reading), except when the target was deliberately oxidized to observe the effect of surface oxidation on thermal radiation detected by the pyrometer. The thermocouple was calibrated at melting point of gold (1337.4 K) and was found to read 2.7 K low. The accuracy is estimated ± 1 K.

Several factors that might cause error in pyrometer reading were investigated during the calibrations, including non-normal pyrometer viewing angle, surface oxidation, IR absorption of CO_2 in gas flow (through which the samples were observed by the pyrometers), systematic errors in the pyrometers, and IR transmission and reflection properties of windows and mirrors in the pyrometer light path. The last two factors were found to be the major causes of uncertainty. Thin quartz or Pyrex windows and gold mirrors can greatly reduce errors of the last type. Corrections for residual errors were made to the pre-shock temperatures of the shock-wave experiments. To summarize, the pyrometers were able to determine the sample temperature to within about 10 K after the thermocouple calibrations.

The spatial variation in temperature in target is estimated and measured to be about 52 K at pre-shock temperature 1573 K (Appendix A).

The experiments are of two types: EOS and VISAR. Detailed descriptions of the

two types of experiments can be found in *Miller et al.* [1988] and *Duffy and Ahrens* [1994a] respectively, and they are briefly explained in the following sections.

3.3 EOS Experiments at 1573 K

These experiments have been conducted on the 40 mm propellant gun at Caltech in the 17–74 GPa range (Figure 3.1, Table 3.1). The equation of state experiments monitor optical reflectivity on the (stepped) back surface of the target which decreases rapidly upon shock arrival. In experiments we measure initial density (using the measurement of initial temperature and iron's density-temperature relationship *Touloukian* [1970]), shock-wave velocity and projectile velocity, and derive particle velocity, shock pressure and the high pressure specific volume by the impedance matching method (Appendix B). The properties of the impactor materials and data sources are given in Table 3.2.

The results are plotted in Figures 3.2 and 3.3. Although melting may have occurred in the highest pressure experiments, all the u_S-u_P data can be fit with a linear function:

$$u_S = 4.102(0.015)\ \text{km/s} + 1.610(0.014)\ u_P. \tag{3.1}$$

For reference, the principal u_S-u_P relationship of iron in the ϵ phase is [*Brown and McQueen*, 1986]:

$$u_S = 3.955(0.028)\ \text{km/s} + 1.58(0.011)\ u_P, \tag{3.2}$$

with an initial density of 7.850 Mg/m^3 (for α-iron at STP).

With initial density at 1573 K of 7.413(0.012) Mg/m^3 [*Touloukian*, 1970] (the uncertainty is estimated from the pre-shock temperature uncertainty of about 52 K (Appendix A)), and using the relations between c_0, s and K_{0S}, K'_{0S} [*Ruoff*, 1967]:

$$K_{0S} = \rho_0 c_0^2, \tag{3.3}$$

$$K'_{0S} = 4s - 1, \tag{3.4}$$

Table 3.1: Hugoniot data for γ-iron centered at 1573 K (initial density is 7.413±0.012 Mg/m^3).

Shot	Flyer Plate			Fe Sample Thicknesses[1]		Shock Velocity	Particle Velocity	Pressure	Density	Shock Temperature[2]
	Material	Thickness[1] (mm)	Impact Velocity (km/s)	Driver (mm)	Total (mm)	(km/s)	(km/s)	(GPa)	(Mg/m^3)	(K)
946	Al	2.731	1.432	1.953	5.925	4.873	0.482	17.4	8.246	1883
		(0.003)	(0.005)	(0.008)	(0.002)	(0.009)	(0.002)	(0.1)	(0.005)	(69)
944	Ta	2.794	1.574	1.988	5.950	5.717	0.974	41.4	8.957	2272
		(0.003)	(0.006)	(0.018)	(0.003)	(0.020)	(0.004)	(0.2)	(0.011)	(142)
978	Ta	5.161	1.976	1.976	5.966	5.940	1.220	53.9	9.354	2445
		(0.003)	(0.006)	(0.004)	(0.003)	(0.026)	(0.004)	(0.2)	(0.017)	(176)
992	Ta	2.649	2.146	2.054	6.099	6.255	1.311	60.9	9.401	2607
		(0.003)	(0.007)	(0.003)	(0.003)	(0.010)	(0.005)	(0.2)	(0.012)	(145)
980	Ta	2.720	2.230	2.087	6.099	6.149	1.375	62.8	9.567	2643
		(0.003)	(0.007)	(0.003)	(0.002)	(0.040)	(0.006)	(0.3)	(0.026)	(149)
989	Ta	2.756	2.378	2.057	6.022	6.364	1.457	69.0	9.650	2767
		(0.003)	(0.008)	(0.030)	(0.005)	(0.022)	(0.006)	(0.3)	(0.017)	(161)
945	Ta	2.751	2.513	1.980	5.888	6.527	1.537	74.4	9.733	2820
		(0.003)	(0.010)	(0.006)	(0.003)	(0.020)	(0.007)	(0.4)	(0.018)	(161)

1. Measured at room temperature.
2. Calculated in Section 3.4.2. Uncertainties include those in experimental measurements and calculation to high pressure.

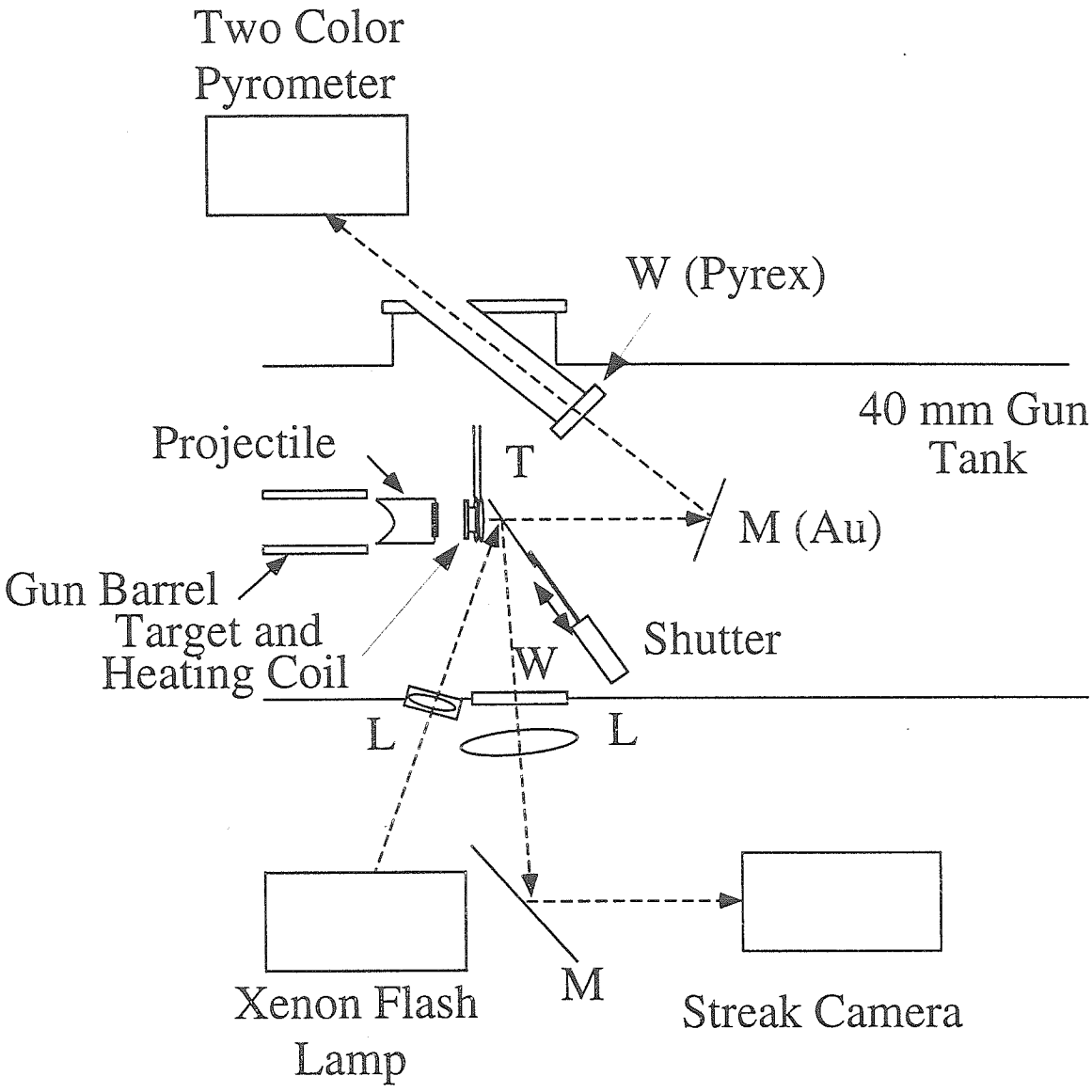

Figure 3.1: Experimental assemblies for EOS experiments. Iron target is preheated with RF induction coils and temperature is monitored by pyrometer. Abbreviations: W: window; L: lens; M: mirror; M (Au): gold mirror; T: EOS turning mirror. About 1 second before launching projectile, EOS turning mirror is inserted in front of the target free-surface via a compressed air-operated piston [*Rigden et al.*, 1988].

Table 3.2: Equation of states of flyer plate materials.

Material	ρ_0 (Mg/m^3)	c_0 (km/s)	s
Ta[1]	16.650	3.293	1.307
	(0.030)	(0.005)	(0.025)
Al 2024[2]	2.784	5.330	1.34
	(0.005)	(0.050)	(0.02)
Al 6061[2]	2.683	5.349	1.34
	(0.003)	(0.056)	(0.20)

1. *Mitchell and Nellis* [1981]
2. *Marsh* [1980]

the u_S-u_P relation gives:

$$K_{0S}^{1573\ \mathrm{K}} = 124.7(1.1)\ \mathrm{GPa}, \tag{3.5}$$

and

$$K'_{0S} = 5.44(0.06) \tag{3.6}$$

for γ-iron. We note that Equations 3.3 and 3.4 assume the Murnaghan relation in the density-pressure space [*Ruoff*, 1967].

3.4 Sound Velocity Measurements at 1573 K

The VISAR (Velocity Interferometer System for Any Reflector, Figure 3.4) was originally described by *Barker and Hollenbach* [1972]. This technique uses a modified Michaelson interferometer to measure the Doppler-shift of a laser beam reflected from the surface of the moving target. The VISAR works by introducing a 1-2 ns delay between the two beams of the interferometer through the use of etalon bars in one leg. At the same time, the mirror positions are adjusted so that the two end mirrors appear to be coincident from the point of view of the detector. This technique extends the use of interferometry to spatially incoherent sources while at the same time maintaining the time delay which is necessary to record velocity information. The VISAR system we used has incorporated the push-pull modification of *Hemsing*

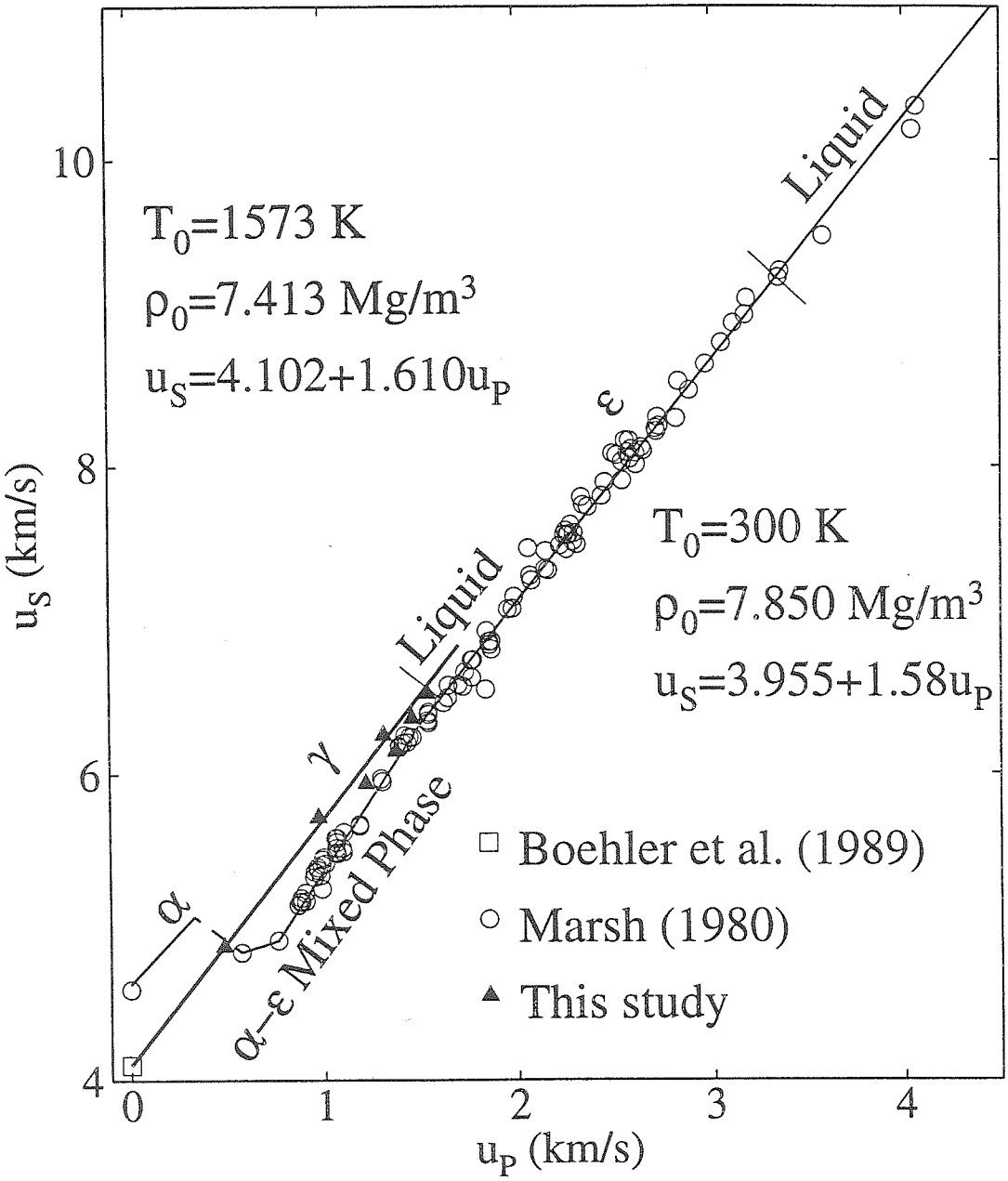

Figure 3.2: u_S-u_P relation of high temperature (1573 K) iron (heavy solid line). The principal shock-wave data (light solid line) are also shown for comparison. The α-phase Hugoniot centered at STP is from *Barker and Hollenbach* [1974]. Dashed line between the α-phase and the mixed phase indicates the states are not achievable experimentally.

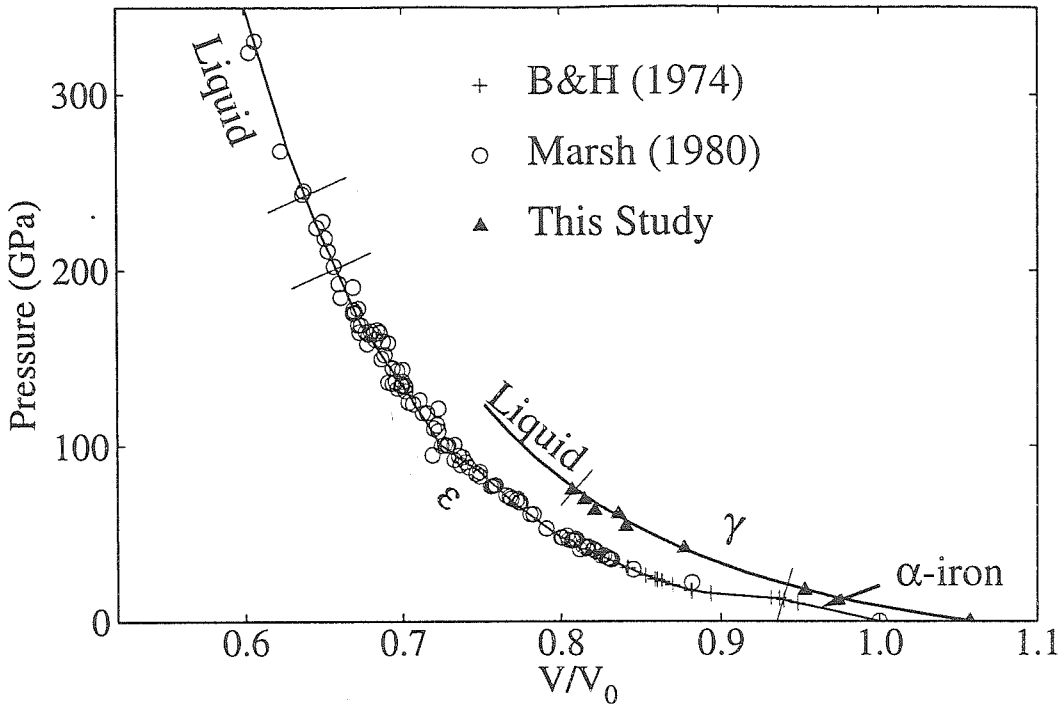

Figure 3.3: High temperature, γ-iron (1573 K) Hugoniot (heavy line) of this study compared to the α-iron principal Hugoniot. Specific volume is normalized to that of iron at STP V_0. B&H stands for *Barker and Hollenbach* [1974].

[1979], which introduces a 90° phase shift between the p- and s-polarized components of the returned light and permits separate recording of the two components. The advantages of this technique are: First, the ambiguities in the sign of the acceleration are removed. When the sign of the acceleration reverses, the leading polarization component reverses as well. Furthermore, the loss of velocity resolution near fringe peaks and troughs is eliminated since when one component is near an inflection point, the other is near its midpoint, where velocity resolution is maximized.

The relationship between the reflector velocity, u, and the fringe count, F, is given by *Barker and Hollenbach* [1972]:

$$u(t - \tau/2) = kF(t), \tag{3.7}$$

where k is the fringe constant, which is given by *Barker and Hollenbach* [1974]:

$$k = \frac{\lambda_0}{2\tau(1+\Delta\nu/\nu_0)(1+\delta)}, \tag{3.8}$$

where the incident laser wavelength, λ_0=514.5 nm, $(1+\delta)$ is a correction term related to dispersion in the etalons, and $(1+\Delta\nu/\nu_0)$ is a correction term that accounts for the change in the reflective index of the shock-compressed window material [*Barker and Hollenbach*, 1970]. For our experiments where windows are not used, this term is unity. $(1+\delta)$ has been determined by *Barker and Hollenbach* [1974] to be 1.0339 at $\lambda = 514.5$ nm. The delay time τ is determined from:

$$\tau = \frac{2h}{c}(n - \frac{1}{n}), \tag{3.9}$$

where $h = 189.92$ mm is the etalon thickness, $n = 1.468 \pm 0.003$ [*Duffy*, 1992] is the etalon refractive index, and c is the speed of light. From Equations 3.8 and 3.9, the fringe constant is determined to be 225 m/s/fringe for our experiments.

In our experiments the free-surface of the iron target or the molybdenum cap first accelerates upon shock arrival, then decelerates when the release wave from the back of the flyer plate has propagated to the free-surface. The initial release velocity (which equals to compressional sound velocity in solids and bulk sound velocity in liquids) in shock compressed γ- or molten iron can be calculated from the time interval between the acceleration and deceleration of the free-surface. The arrangement is modified from *Duffy and Ahrens* [1994a] for the high temperature environment of our experiments.

Difficulties with high temperature iron VISAR experiments include:

1. The surface of iron samples suffers adverse alteration under high temperature and high pressure; there are a number of possible causes:

   (a) Oxidation during heating. In the typical vacuum in the gun tank ($\sim 100\mu$m Hg), iron oxidizes fairly quickly;

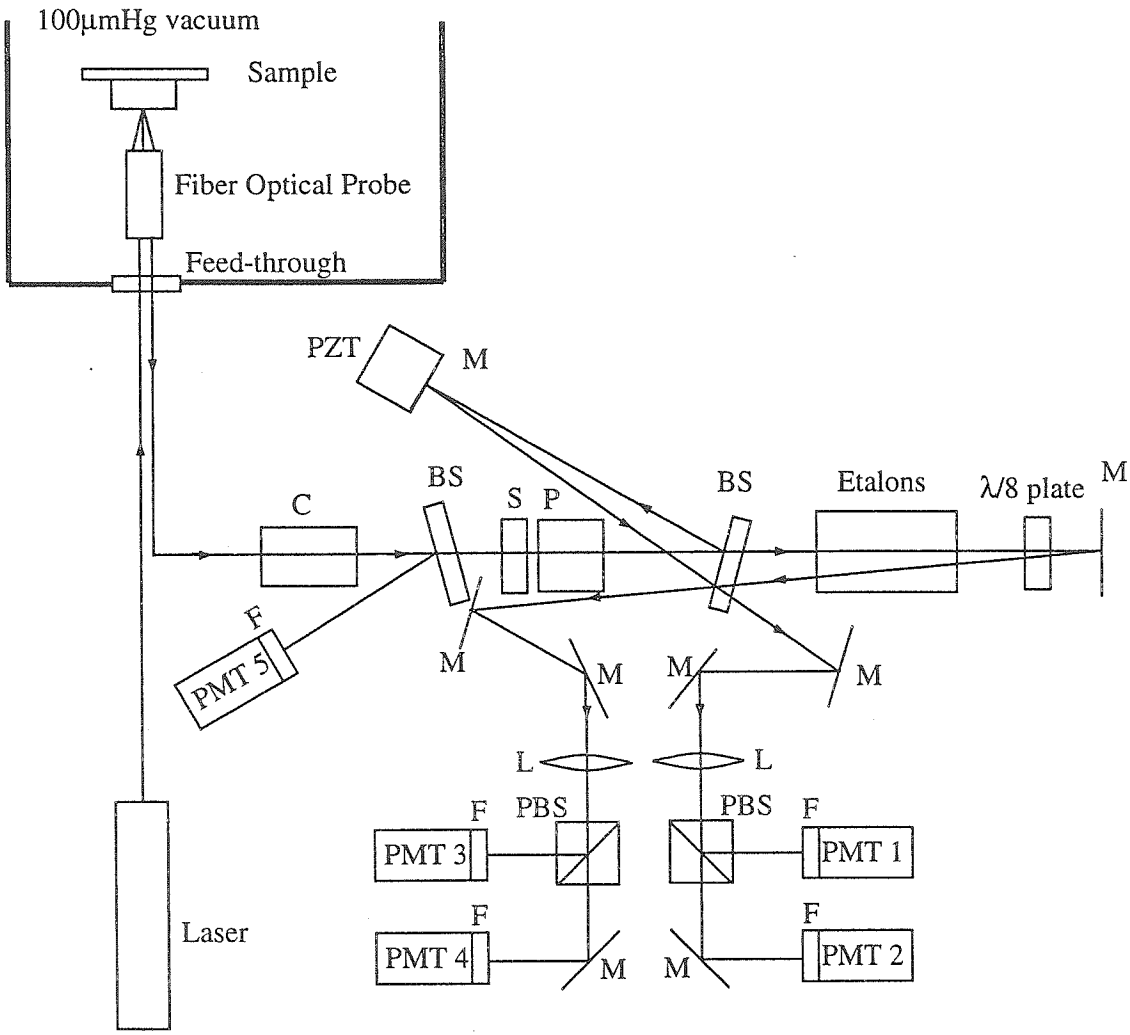

Figure 3.4: VISAR experimental diagram. Abbreviations are: PMT: photomultiplier tube; M: mirror; L: lens; F: Laser line filter; S: polarization scrambler; PZT: piezoelectric transducer; P: Glan-Thomson prism; BS: beam splitter; PBS: polarizing beam splitter cube. Laser is a Lexel model 95 argon ion laser. Detailed description and function of components are given in *Duffy* [1992].

(b) The α to γ phase transition at 1196 K may change the surface texture of the sample;

(c) The initial temperature (1573 K) is close to iron's melting point, and some jetting may occur upon the shock arrival [*Yang and Ahrens*, 1995].

To counter these problems, we used a 0.5 mm thick molybdenum cap on the rear surface of the iron as the diffuse VISAR reflector, and bled reducing gas near the target (Figures 3.5 and 3.6). Mo, with its higher melting point at 1 bar and being less oxidation prone, is a better VISAR reflector than iron.

2. Different thermal expansions of the metal sample and the ceramic target holder can crack the ceramic or change target position at 1573 K. We used belleville washers in the target fixture (Figure 3.5) to maintain a constant compression force (about 7 newtons) squeezing the ceramic holder and the iron-molybdenum target together.

3. Radiant heating from the target would rapidly deform the plastic lens used in VISAR fiber optical probes. We used hot mirrors and heat-absorbing glass (for their sources, see caption of Figure 3.6) in front of the probe. We also mounted the probe assembly on a compressed air-driven piston [*Rigden et al.*, 1988] to retract the probe during heating. We tested the VISAR signal at 1573 K before launching the projectile. We also split off about 10% of the reflected laser to monitor the reflected light intensity change upon shock arrival at the Mo free surface.

4. Usually it is advantageous to have a window attached to the surface at which the particle velocity is recorded with VISAR. Although the window is generally not a perfect impedance match with the target and causes partial release or reshock, the target adjacent to it will partially maintain the high pressure state and the forward rarefaction wave would induce a more pronounced particle velocity decrease. However, among the most common used window materials, LiF has a melting point of 1118 K [*Lide*, 1993–1994, p. 4-70], too low for our

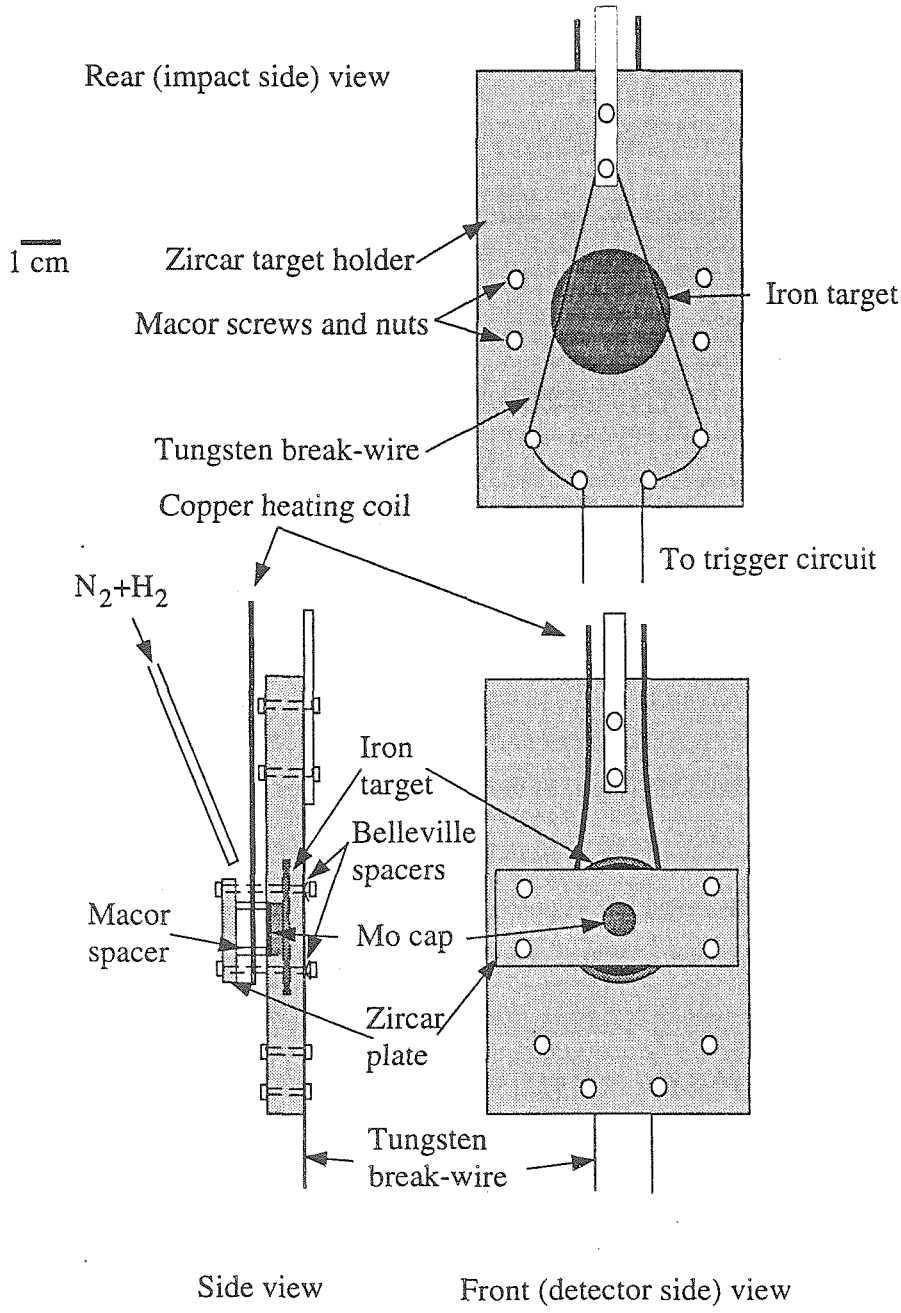

Figure 3.5: Drawing of target assembly for measuring sound velocity in preheated iron. Belleville washers are from McMaster-Carr, model 9716K45. The break wire is made of tungsten of 0.076 mm diameter (Alfa Aesar Co., #00457). It is clamped with slight tension with ceramic screws and nuts, flush with the impact side of the ceramic target holder. The distance from the break wire to the driver plate is usually 5–6 mm.

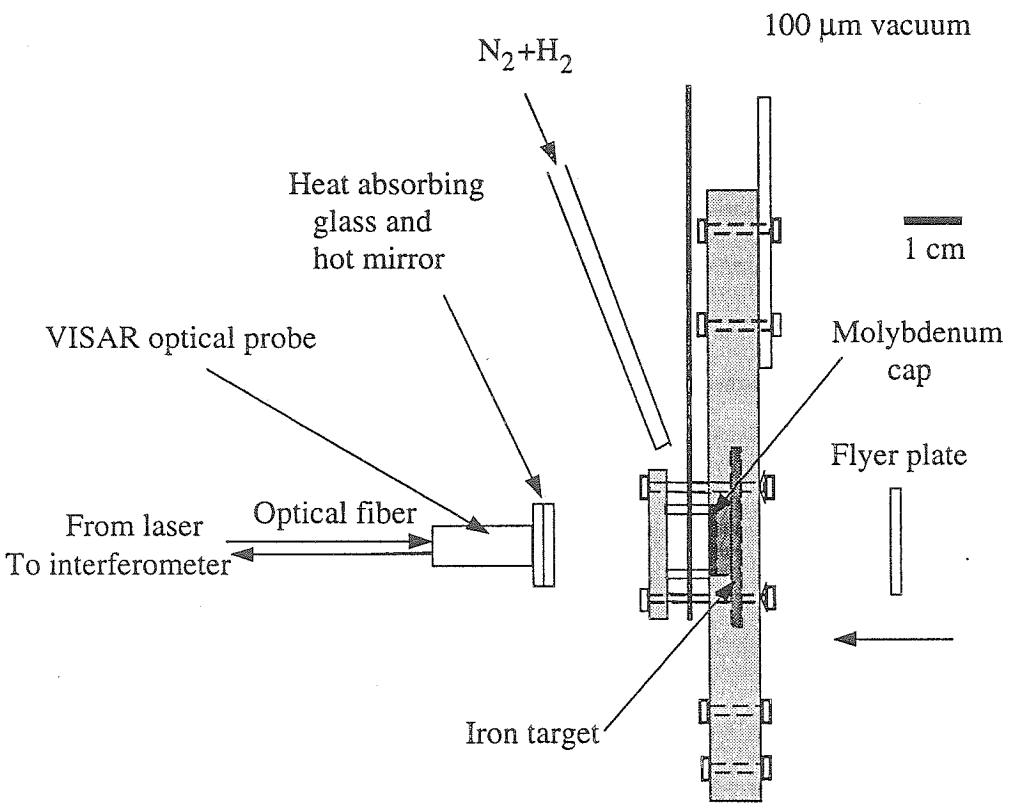

Figure 3.6: Experimental arrangement for conducting sound speed measurements in preheated iron. Sources of the parts are: Heat absorbing glass: CVI Laser Corp., model #SKG-5-2x2, 2 mm thick; Hot mirror: ZC&R extended hot mirror, 3.0 mm thick; VISAR probe: Valyn International, #FOP-300.

preheated experiments. Sapphire (Al_2O_3) has a higher melting point (2288 K [*Lide*, 1993–1994, p. 4-36]) and is an excellent impedance match for Fe, but it has been found that it can not be used for VISAR experiments above 15 GPa (the reason is unknown) [*Barker and Hollenbach*, 1974]. Therefore, we resorted to observing velocity changes at the free surface. These changes are fairly small, but as we will discuss in the following section, they are recorded without ambiguity.

5. The digital oscilloscopes used in the experiments have recording window of 8, 16 and 64 μs; therefore, a signal shortly before the impact occurs is necessary to trigger the oscilloscopes. In room temperature VISAR experiments, trigger pins affixed on the driver plates and pulse forming circuits serve as oscilloscope triggers. However, trigger pins that can withstand high temperature are not available at present. We developed a break-wire system (Figure 3.5) that has been found to be reliable for high temperature experiments at 1573 K.

The experimental conditions are listed in Table 3.3.

3.4.1 Data Reduction and Experimental Results

The Lagrangian time-distance diagram for shock-wave propagation in our iron targets is shown in Figure 3.7. VISAR scope record from Shot 1008 is shown in Figure 3.8. The shock arrival, sustained shocked state, and initial release wave arrival are very clear in the record.

The experimental scope records are first reduced to the free surface velocity profiles (Figure 3.9) using a computer program modified from a program used by *Duffy* [1992]. The major modification is due to the change in experimental arrangement: we now reduce the two pairs of out-of-phase PMT channels (PMT 1 and 3, and PMT 2 and 4 in Figure 3.4) to two channels by subtracting within each pair with a differential amplifier; therefore, there are two (instead of four) digital records $d_1(t)$ and $d_2(t)$ from

Table 3.3: Initial conditions for VISAR experiments.

Shot	Flyer			Sample			Molybdenum Cap	
	Material	Thickness (mm)	u_{fp} (km/s)	ρ_0 (Mg/m^3)	Thickness (mm)	Temperature (K)	ρ_0 (Mg/m^3)	Thickness (mm)
1014	Al (6061)	1.742(2)	1.290(10)	7.834(2)	6.030(2)	1567	10.19(1)	0.460(2)
961	Al (2024)	1.013(2)	1.455(10)	7.855(2)	6.005(2)	1574	–	–
1013	Al (6061)	1.923(5)	1.997(10)	7.853(6)	6.071(4)	1561	10.22(1)	0.455(1)
1003	Fe	2.047(2)	1.965(10)	7.853(2)	6.076(3)	293	–	–
1007	Ta	1.184(1)	1.987(10)	7.858(3)	6.088(3)	1567	10.17(2)	0.479(1)
1010	Ta	1.164(4)	2.388(30)	7.856(3)	6.040(1)	1565	10.23(2)	0.442(2)
1008	Ta	1.046(3)	2.439(10)	7.857(3)	6.040(1)	1565	10.15(1)	0.476(1)
1011	Ta	1.115(2)	2.452(10)	7.813(8)	6.048(1)	1566	10.26(1)	0.476(1)
1015	Ta	1.084(3)	2.455(20)	7.843(2)	5.875(2)	1565	10.22(1)	0.470(3)

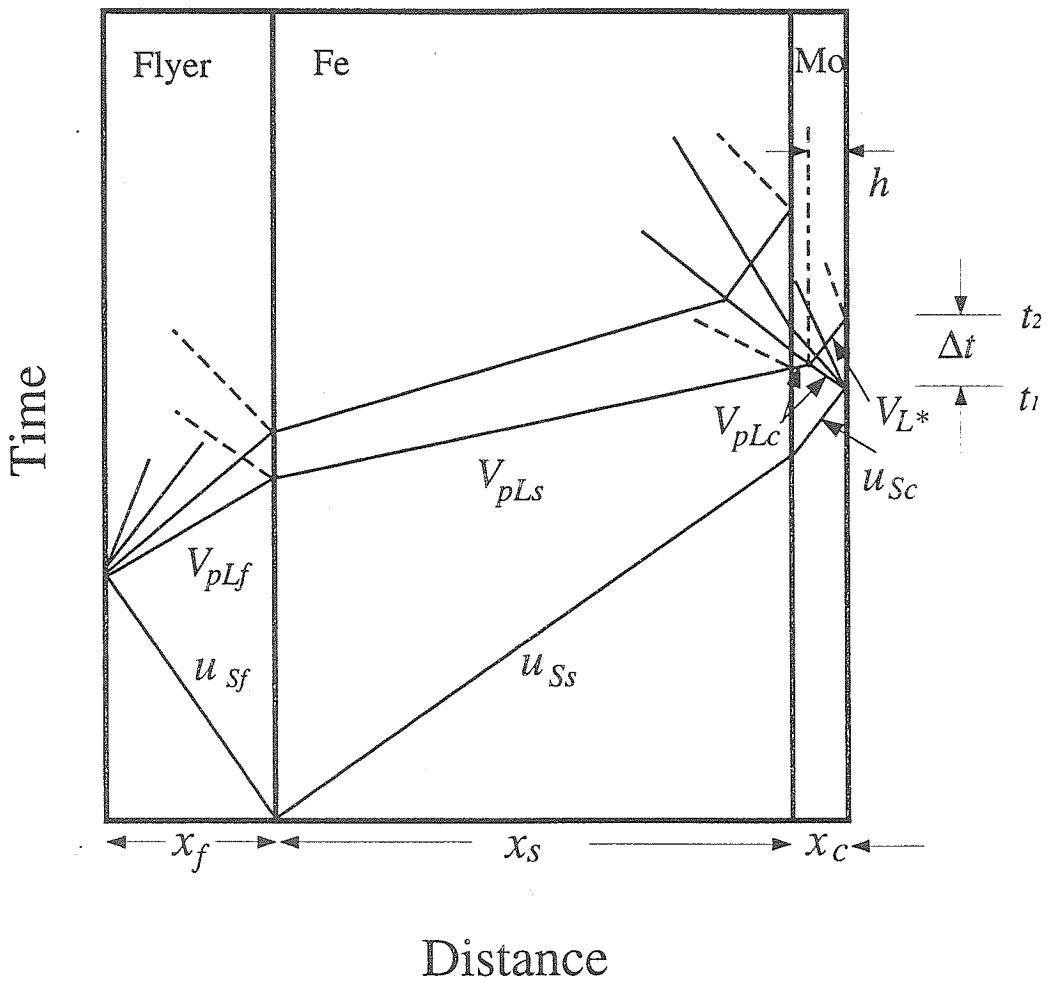

Figure 3.7: Lagrangian x-t diagram for the VISAR experiments. t_1 indicates shock arrival. t_2 indicates initial rarefaction wave arrival. $\Delta t = t_2 - t_1$, h is spalling thickness. Not all shots have molybdenum cap.

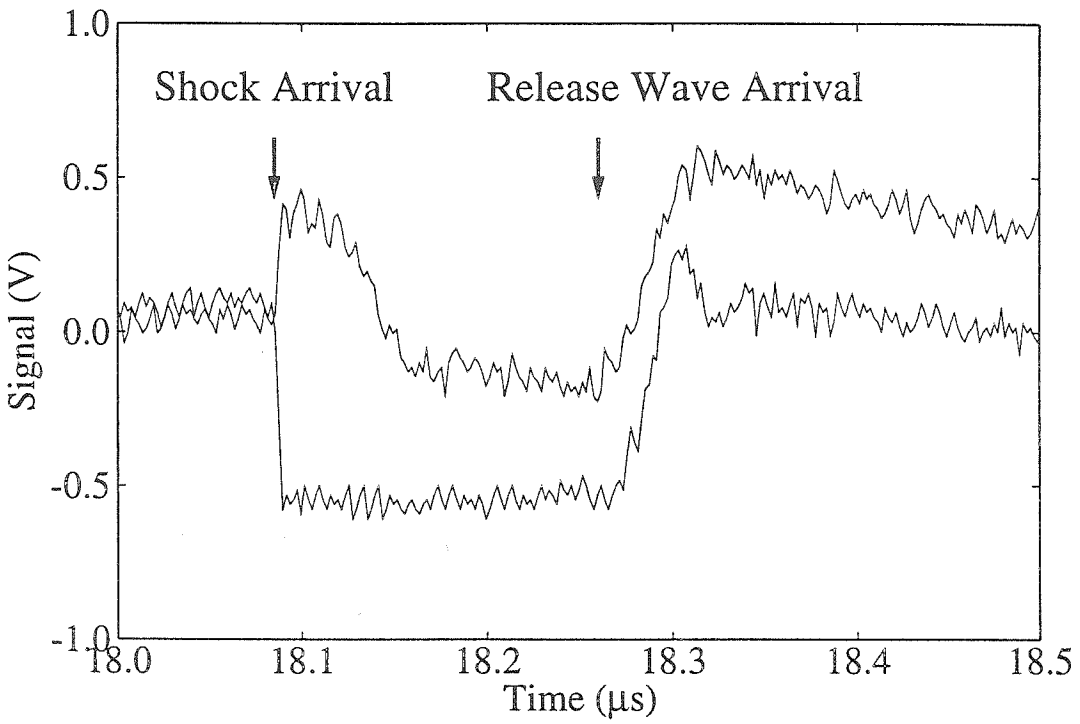

Figure 3.8: VISAR record of Shot 1008. First change in signal amplitude corresponds to shock arrival at free-surface of the Fe/Mo target assembly. Plateau in signal corresponds to the free-surface motion after shock arrival. Second signal amplitude change corresponds to rarefaction wave arrival. Origin of time axis is arbitrary.

Table 3.4: Coefficients of polynomial fits (Equation 3.11) to Hugoniot longitudinal sound velocities.

Material	d_0	d_1, $(\times 10^{-2})$	d_2, $(\times 10^{-2})$
Al 6061[1]	1.8810	1.9252	2.2054
Ta[1]	1.4298	-2.6315	2.0542
Mo (1673 K)[2]	4.9812	34.0633	7.4654

1. *Duffy and Ahrens* [1992].
2. Fit to [*Duffy and Ahrens*, 1994b].

each experiment. The velocity is determined using the equation:

$$V(t) = k\left[\tan^{-1}\left(\frac{d_2(t) - d_1(t)\cos\phi}{d_1(t)\sin\phi}\right) - \psi_0\right], \tag{3.10}$$

where $\phi \approx 90°$ is the phase angle between the two channels, ψ_0 is the initial random phase at $t = 0$, and k is the fringe constant in velocity per angular degree.

After the velocity profile is obtained, the time between the shock-wave arrival and the initial release wave arrival is measured. The first rarefaction wave arrival is taken as the first data point after which the free-surface velocity is consistently lower than the average plateau velocity (Figure 3.9 inset). Such determined δt has an uncertainty of about 2-3 ns. To calculate the sound velocity in high pressure iron from Δt in Figure 3.7, we must utilize our knowledge of equations of state and longitudinal sound velocities in Al 6061, Ta and Mo (1573 K). For Mo at 1573 K, we used the 1673 K data by *Miller et al.* [1988] and *Duffy* [1992]. An empirical functional form used to fit the sound velocity dependence on pressure is the following [*Wang*, 1988]:

$$\ln V_X = d_0 + d_1 \ln P + d_2 \ln^2 P, \tag{3.11}$$

where the subscript $X = P$ or B for longitudinal or bulk velocities, respectively. The parameters of the fits are given in Table 3.4 for pressure expressed in GPa and velocity expressed in km/s. The uncertainties of the fits are generally within 2%. The fitted sound velocities in the pressure range of this study are plotted in Figure 3.10.

The spallation zone (the layer of thickness h in Figure 3.7) for most experiments

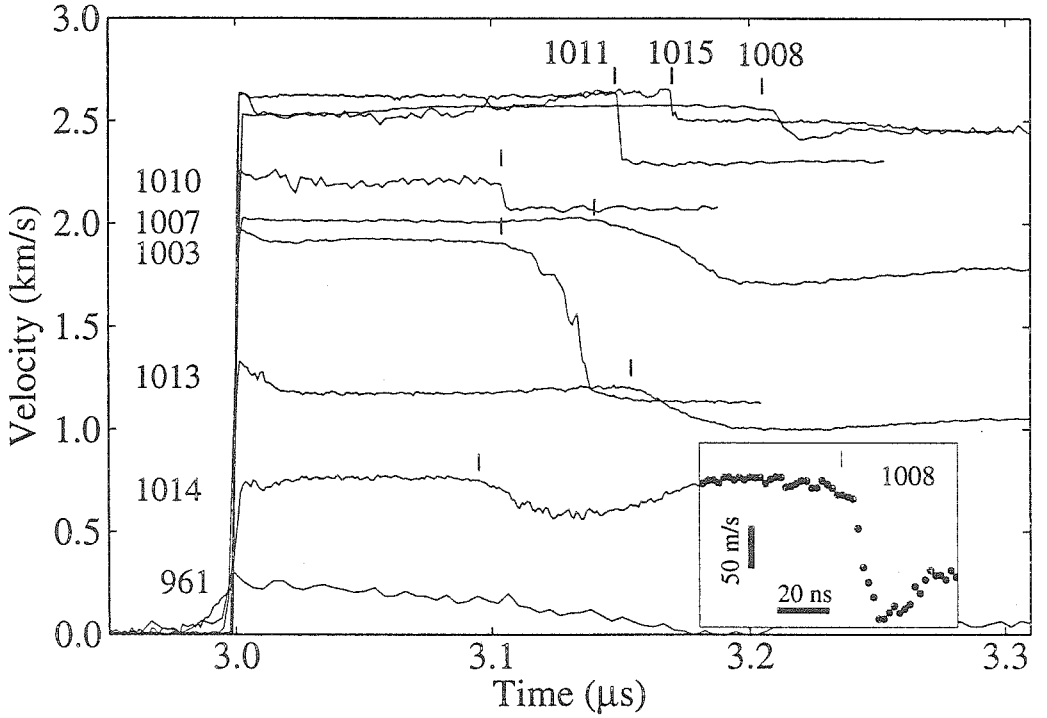

Figure 3.9: Free-surface velocity profiles from VISAR experiments. Shot numbers are shown near each wave profile. Vertical lines indicate initial unloading arrivals. Particle velocities are within 4% of the impedance match solutions. Origin of time axis is arbitrary. Inset: detailed plot of the first release wave arrival for shot 1008.

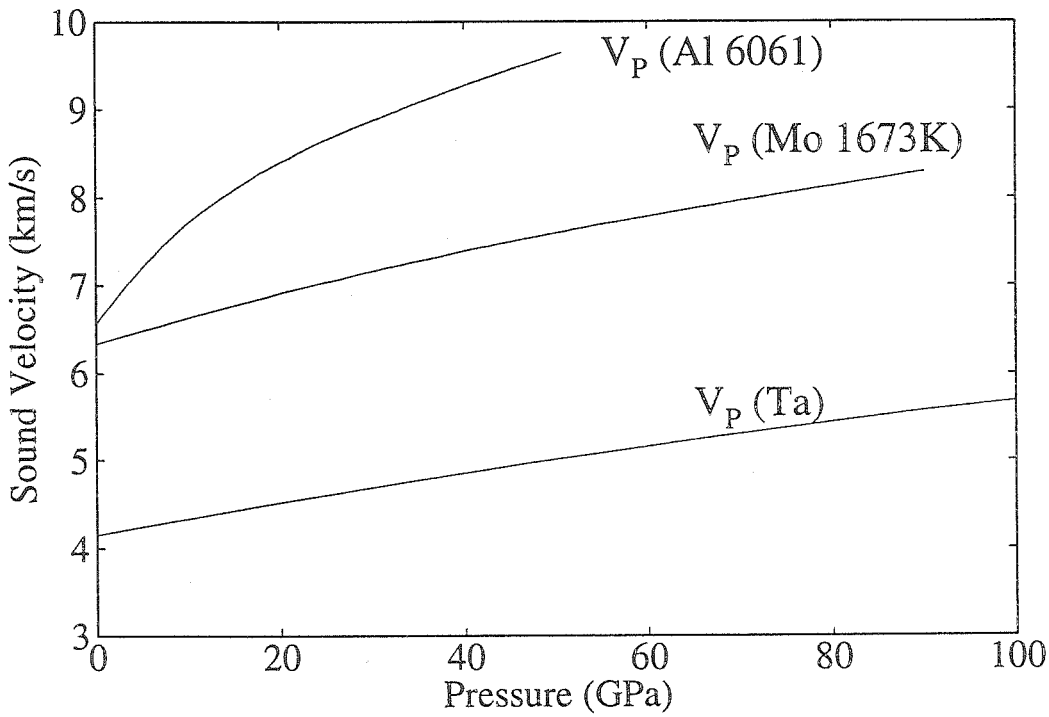

Figure 3.10: Sound velocities of materials used in high temperature iron experiments: aluminum 6061, tantalum, and molybdenum at 1673 K. References: Al 6061: Ultrasonic: *Thomas* [1968], 9–44 GPa: [*Asay and Chhabildas*, 1981; *Duffy and Ahrens*, 1994b]; Mo (1673 K): Ultrasonic: *Katahara et al.* [1979], 12–81 GPa: [*Duffy and Ahrens*, 1994b]; Ta: Ultrasonic: *Marsh* [1980], 83 GPa: [*Asay et al.*, 1986], 150–430 GPa: [*Brown and Shaner*, 1984].

are inside the Mo cap, but for shot 1008 it is inside the iron sample. We first consider the case where the spallation is inside Mo. In this case,

$$\Delta t \leq x_c(\frac{1}{u_{Sc}} + \frac{1}{V_{L*}}). \tag{3.12}$$

The equations of the timing relations in Figure 3.7 can be written as:

$$\Delta t = h(\frac{1}{u_{Sc}} + \frac{1}{V_{L*}}), \tag{3.13}$$

$$x_f(\frac{1}{u_{Sf}} + \frac{1}{V_{pLf}}) + \frac{x_s}{V_{pLs}} + \frac{x_c - h}{V_{pLc}} = \frac{x_s}{u_{Ss}} + \frac{x_c}{u_{Sc}} + \frac{h}{V_{pLc}}, \tag{3.14}$$

for meaning of the symbols, refer to Figure 3.7. The subscript L refer to the Lagrangian sound speeds, which are related to the Eulerian sound speeds by:

$$V_{Lx} = V_{Ex}(\rho_x/\rho_{0x}), \tag{3.15}$$

where x is an attribute of f (flyer), s (sample), or c (cap). ρ_x is the density of the material at shocked state, and ρ_{0x} is its initial density. There is an approximation in Equation 3.14: The third term on the left side is the travel time of the release wave through the entire iron sample, but because iron and molybdenum are not a perfect impedance match, there is a zone at the interface on the iron side that is re-shocked to a higher pressure. Since this zone thickness is small, and the impedance mismatch between iron and molybdenum is not great, the difference in release velocity can be safely ignored.

The solution for Equations 3.13 and 3.14 is:

$$V_{pLs} = \frac{x_s}{x_s/u_{Ss} + x_c/u_{Sc} + (2h - x_c)/V_{pLc} - x_f/V_{pLf} - x_f/u_{Sf}}, \tag{3.16}$$

$$h = \frac{\Delta t}{1/V_{pLc} + 1/V_{L*}}. \tag{3.17}$$

In the case where spallation occurs inside iron, we have derived another set of

equations analogous to Equations 3.13 and 3.14, for which the solution is:

$$V_{pLs} = \frac{-b - \sqrt{b^2 - 4ac}}{2a}, \tag{3.18}$$

$$h = \frac{\Delta t}{1/V_{pLs} + 1/V_{Ls*}}, \tag{3.19}$$

where

$$a = \frac{1}{2}\left(\frac{x_f}{V_{pLf}} + \frac{x_f}{u_{Sf}} - \frac{x_s}{u_{Ss}} - \frac{x_c}{u_{Sc}} - \frac{x_c}{V_{pLc}}\right), \tag{3.20}$$

$$b = V_{Ls*}\left(a + \frac{x_c}{V_{pLc}} + \frac{x_c}{V_{L*}} - \Delta t\right) + \frac{x_s}{2}, \tag{3.21}$$

$$c = \frac{x_s V_{Ls*}}{2}. \tag{3.22}$$

The reduced sound velocity and spallation thickness data are listed in Table 3.4.1.

3.4.2 Phase Determination

The 1573 K Hugoniot in pressure-volume space is shown in Figure 3.3 together with the (α-phase) principal Hugoniot. The high-temperature Hugoniot obtained so far (up to 74 GPa) is shifted from the principal Hugoniot by a nearly constant factor (volume change due to thermal expansion and the $\alpha \rightarrow \gamma$ phase change at 1 bar, which is about 5.7%). As the solid-liquid transition is not prominent in the P-V space, pressure-volume equation of state experiments are not adequate for detecting melting.

The initial release wave velocity data in the laboratory (Eulerian) reference frame are plotted in Figure 3.11 as a function of shock pressure. Also plotted in the figure are previous measurements by *Brown and McQueen* [1986] and *Nasch et al.* [1994] for ϵ-, γ- and liquid iron. It can be seen there is a sharp drop in sound velocity at about 70 GPa, and the 72 GPa (Shot 1008) datum agrees very well with liquid iron data interpolated between *Brown and McQueen* [1986]'s shock-wave data and *Nasch et al.* [1994]'s ultrasonic data. Therefore, we infer the steep drop in sound velocity at 70±2 GPa corresponds to the melting of γ-iron along its Hugoniot centered at 1573

Table 3.5: Sound velocity in γ- and liquid iron.

Shot	Δt (ns)	Pressure (GPa)	V_P (Flyer) (km/s)	V_P (Mo Cap) (km/s)	V_P (Fe) (km/s)	Spalling Thickness[1] (mm)	Shock Temperature[2] (K)	Density (Mg/m^3)
1014	95	15.2	8.10	6.86	6.08	0.28	1848 (65)	8.13
961	0.0	17.4	5.99	–	> 5.69	0.0	1883 (69)	8.23
1013	152	25.6	8.68	7.18	6.12	0.45	2012 (81)	8.51
1003[3]	104	42.5	–	–	–	–	–	–
1007	139	54.8	5.09	7.88	7.31	0.44	2455 (176)	9.29
1010	103	69.6	5.30	8.16	7.74	0.33	2767 (161)	9.58
1008	207	71.6	5.33	8.21	6.55	0.17	2780 (161)	9.62
1011	145	72.1	5.33	8.21	7.22	0.47	2795 (161)	9.63
1015	170	72.4	5.33	8.22	6.80	0.06	2812 (161)	9.64

1. Spallation occurred in Mo for all but Shot 1008.
2. Calculated in Section 3.4.2. Uncertainties include those in experimental measurements and calculation to high pressure.
3. Room temperature experiment.

K.

It is puzzling to notice that the present γ-iron sound velocity data seem to lie slightly above the extrapolation of *Brown and McQueen* [1986]'s data (the middle dashed line in Figure 3.11), as the elastic moduli usually decrease with temperature. We believe the velocities measured correspond to those of γ-iron because:

1. The present data set definitely start in the γ-iron field because of the initial high temperature. This portion of the phase diagram is well determined (Figures 2.1 and 2.2). The recently proposed ϵ'-phase [*Yoo et al.*, 1995] is reported to occur at about 40 GPa and 1500 K. However, this result has not been verified; therefore, the γ-phase is the only stable phase of iron in this P-T range.

2. *Boehler et al.* [1989] measured static compressibility of the γ-Fe at pressures up to 42 GPa and temperatures between 1200–2100 K. The fit to their data yields $K_{0T} = 127$ GPa and K'_{0T}=2.2. Using the density of iron at 1573 K and neglecting the correction from K_T to K_S, we calculate the bulk sound velocity to be 4.1 km/s. To calculate the longitudinal sound velocity of γ-iron, we need to know its Poisson's ratio ν, which has not been measured at present. We assume it is close to the Poisson's ratio of α-iron at 293 K and 1 bar. This is calculated from the relationship between V_b and the shear wave speed V_s:

$$V_p = V_s\sqrt{\frac{2-2\nu}{1-2\nu}}, \tag{3.23}$$

with V_p=5.94 km/s and V_s=3.26 km/s [*Marsh*, 1980], Equation 3.23 gives ν = 0.284 for α-iron. Assuming the same value for γ-iron, the longitudinal sound velocity calculated from:

$$V_b = V_p\sqrt{\frac{1+\nu}{3(1-\nu)}} \tag{3.24}$$

is 5.30 km/s. This value is reasonable compared to our low pressure sound velocity data of 6.08 km/s at 15.2 GPa. Ignoring the difference between the

Hugoniot and the isentrope, we estimate

$$\left(\frac{\partial V_p}{\partial P}\right)_S = \frac{6.08 - 5.30}{15.2} = 5.13 \times 10^{-2} \text{ (km/s/GPa)} \tag{3.25}$$

for γ-iron at 1573 K.

3. There have been different opinions about the origin of the first velocity drop in *Brown and McQueen* [1986]'s sound velocity data along the principal Hugoniot [*Boehler*, 1993; *Belonoshko*, 1997].

   We now believe the first drop in sound velocity at 200 GPa is not due to the ϵ- to γ-phase transition as *Brown and McQueen* [1986] originally inferred. Rather, it could be a kink due to the melting of iron as suggested by *Belonoshko* [1997], or a solid-solid phase change to a dhcp phase [*Saxena et al.*, 1995, 1996]. It is impossible to clarify this controversy based on our data. In summary we conclude that γ-iron shocked along a Hugoniot centered at 1573 K melts at 70±2 GPa.

Shock temperatures of the γ-iron are calculated (Appendix C) and plotted in Figure 3.12 in reference to the different melting curves. The major uncertainties in the calculation rise from the specific heat and the Grüneisen parameter at high pressures. The parameters used in the calculation are listed in Table 3.6. The Grüneisen parameter of 1.73 for γ-iron at 1573 K and 1 bar, calculated using Equation C.5, is very close to that of α-iron (1.72) at STP (calculated from $\rho_0 = 7.850$ Mg/m^3, thermal expansion $\alpha_0 = 3.54 \times 10^{-5}$ K^{-1} [*Touloukian*, 1970], $C_{P0} = 447.3$ J kg^{-1} K^{-1}, and $K_{0T} = 171$ GPa [*Huang et al.*, 1987]). Previously reported values for α-iron are 1.7 [*Boehler and Ramakrishnan*, 1980] and 1.69 [*McQueen et al.*, 1970]. C_{V0} at 1 bar, 1573 K is calculated from C_{P0} using the equation:

$$C_{V0} = C_{P0}/(1 + \alpha_0\gamma_0 T), \tag{3.26}$$

which gives $C_{V0} = 0.979 C_{P0} = 665.7$ J kg^{-1} K^{-1}. This value is 49.1% greater than the $3R$ value. For reference, we note C_P of α-iron varies from $3R$ at 293 K to $10R$ at

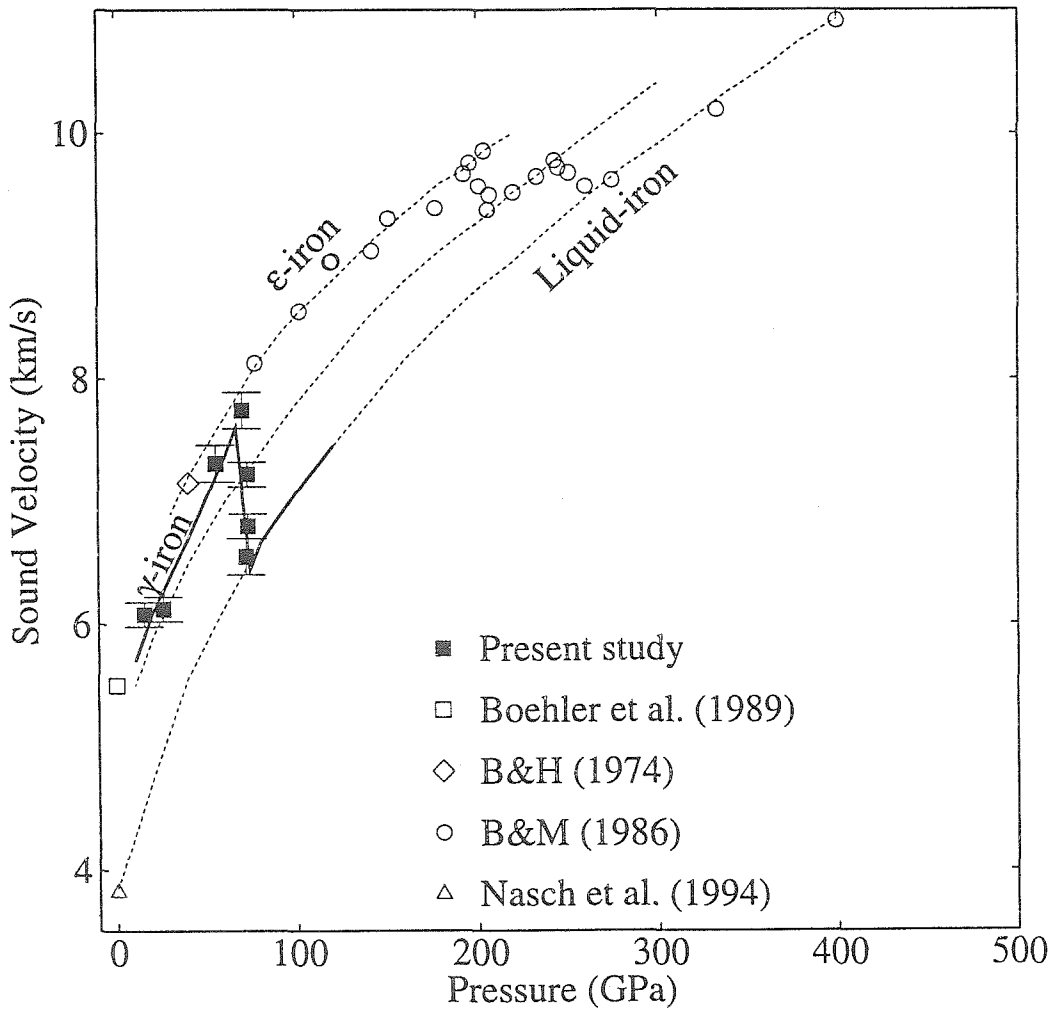

Figure 3.11: Sound velocity measurements. Present data indicate γ-iron melts at about 70±2 GPa. Abbreviations: B&H: *Barker and Hollenbach* [1974]; B&M: *Brown and McQueen* [1986].

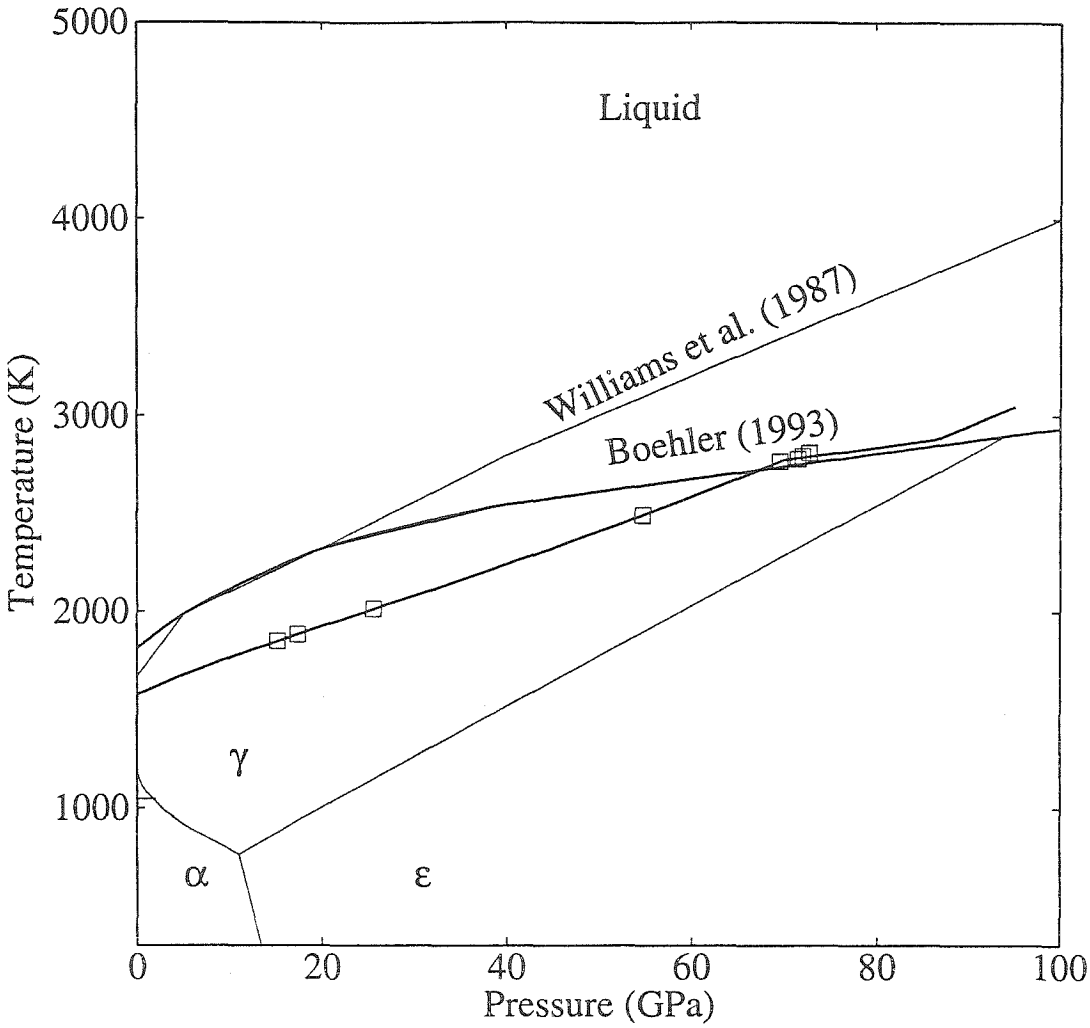

Figure 3.12: Calculated shock temperature versus pressure for 1573 K shock-wave experiments on iron.

1042 K (the Curie point) [*Robie et al.*, 1979]. We attempted three calculations with different values of the two parameters C_V and γ. The calculated temperatures up to 70 GPa (the incipient melting pressure) are listed in Table 3.7. The temperature difference at 70 GPa can be as large as 260 K. However, this is probably an overestimate of uncertainty in our calculation since C_V is unlikely to decrease to $3R$ at high pressures. We think the temperature difference due to different $\gamma(V)$ functions (about 110 K, Table 3.7) may be a more reasonable measure of the uncertainty in the calculation. Combining the 50 K uncertainty in initial temperature, we estimate the melting temperature of γ-iron at 70 GPa to be 2775±160 K.

Table 3.6: Parameters for γ-iron at 1 bar, 1573 K.

ρ_0 (Mg/m^3)	7.413(20)	*Touloukian* [1970]
α_0 (K^{-1})	6.99×10^{-5}	*Touloukian* [1970][1]
c_0 (km/s)	4.102(15)	This study
s	1.610(14)	This study
C_{P0} (J kg^{-1} K^{-1})	679.82	*Robie et al.* [1979]
Latent heat of melting (J/kg)	2.472×10^5	*Robie et al.* [1979]
γ_0	1.73(0.18)	This study

1. Multiplied by a factor of 3 to convert from linear to volumetric thermal expansion coefficient.

γ-iron does not appear to super-heat when it crosses the melting point along the Hugoniot as inferred to occur in ϵ-iron by *Yoo et al.* [1993] but not by *Holland* [1997]. Thus the Hugoniot follows the melting curve between the incipient melting pressure $P_{\rm im}$ to the complete melting pressure $P_{\rm cm}$. To calculate $P_{\rm cm}$, we assume the latent heat of melting ΔH at high pressure is the same as that at 1 bar (Table 3.6). We first calculate Hugoniot temperature of γ-iron to above the melting curve without taking into account the effect of melting, *i.e.*, the temperature of a hypothetical metastable γ-phase. Complete melting occurs at a $P_{\rm cm}$ such that:

$$\Delta S(P_{\rm cm}) = \int_{T_m(P_{\rm cm})}^{T_H} \frac{C_V dT}{T}, \tag{3.27}$$

where $T_m(P_{\rm cm})$ and T_H are melting point and the metastable Hugoniot temperature at $P_{\rm cm}$, respectively, and

$$\Delta S(P_{\rm cm}) = \frac{\Delta H}{T_m(P_{\rm cm})} \tag{3.28}$$

is the entropy change associated with melting at $P_{\rm cm}$. Using $C_V = C_{V0}$ for γ-iron, we obtained $P_{\rm cm}$=86.4 GPa. An alternative assumption that the entropy increase associated with melting is constant yields $P_{\rm cm} = 104.2$ GPa.

Our conclusion that γ-iron shocked from initial temperature of 1573 K is in the liquid field at 70 GPa and 2775 K is consistent with the calculated ϵ-iron melting curve (Figure 2.6), in support of the phase diagram proposed by *Saxena et al.* [1996]. Iron's phase diagram with present uncertainties of the phase boundaries is shown in

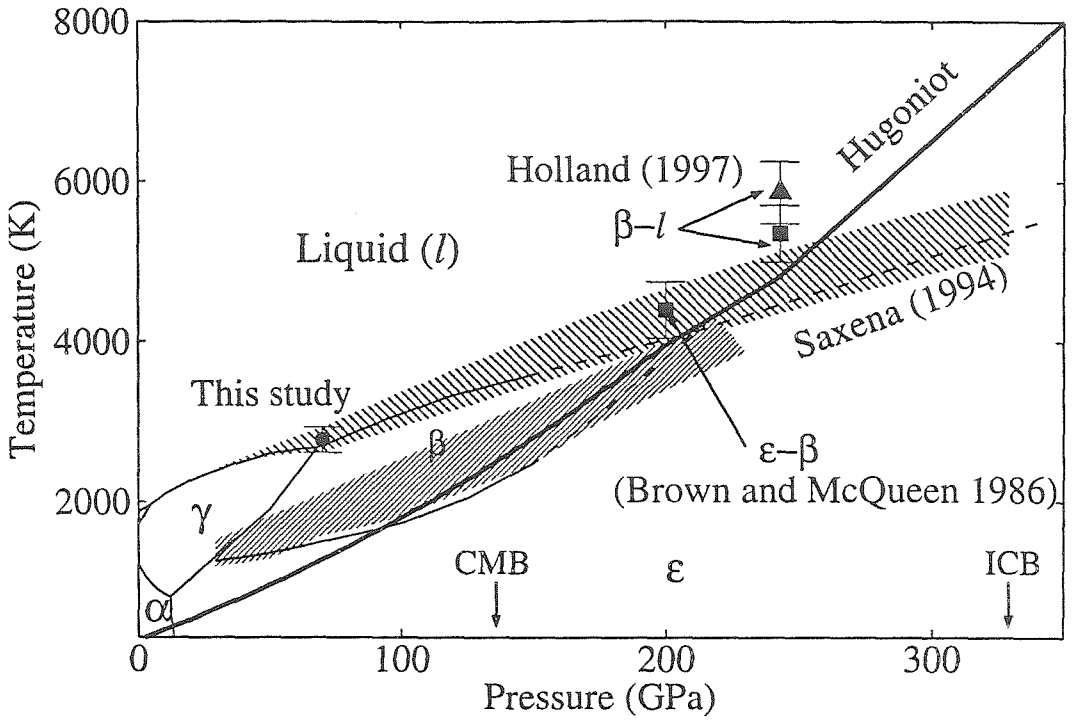

Figure 3.13: Proposed phase diagram of iron. The hachured bands represent uncertainties of phase boundaries. We suggest that the Hugoniot crosses the ϵ-β phase boundary at 200 GPa, and the β-liquid phase boundary at 243 GPa. The solid triangle is *Holland* [1997]'s temperature measurement of the β-liquid transition; The two solid squares are *Brown and McQueen* [1986]'s calculated shock temperatures for what they proposed to be the ϵ to γ and γ to liquid transitions. We now believe these are the ϵ to β and β to liquid transitions.

Figure 3.13. Compared with the phase diagram suggested by *Brown and McQueen* [1982], the melting curve is lowered by about 500 K at 243 GPa, and the β-phase replaces the previously suggested γ stability regime above about 70 GPa.

In Figure 3.14, we also plot the sound velocity as a function of density of γ-iron. Our data and the datum calculated from *Boehler et al.* [1989] indicate that, to a first approximation, the longitudinal sound velocity of γ-iron is linear with respect to density in the pressure range studied. The linear fit is:

$$V_p = -3.13(0.72) + 1.119(0.084)\ \rho, \tag{3.29}$$

with V_p in km/s and ρ in Mg/m^3. This is similar to the results for the bulk sound velocity of lead [*Boness et al.*, 1988].

Table 3.7: Calculated shock temperature of γ-iron initially at 1573 K. Results from three models are presented. In all three, γ_0=1.73.

Pressure (GPa)	Shock Temperature (K)		
	$\gamma\rho$=const $C_V = C_{V0}$	$\gamma\rho$=const $C_V = 3R$	γ =const $C_V = C_{V0}$
10^{-4}	1573	1573	1573
5	1673	1673	1675
10	1763	1765	1769
15	1845	1852	1858
20	1924	1939	1945
25	2002	2028	2031
30	2081	2121	2129
35	2160	2218	2207
40	2241	2319	2298
45	2323	2425	2390
50	2409	2536	2485
55	2457	2653	2581
60	2587	2774	2680
65	2681	2900	2781
70	2775	3032	2884

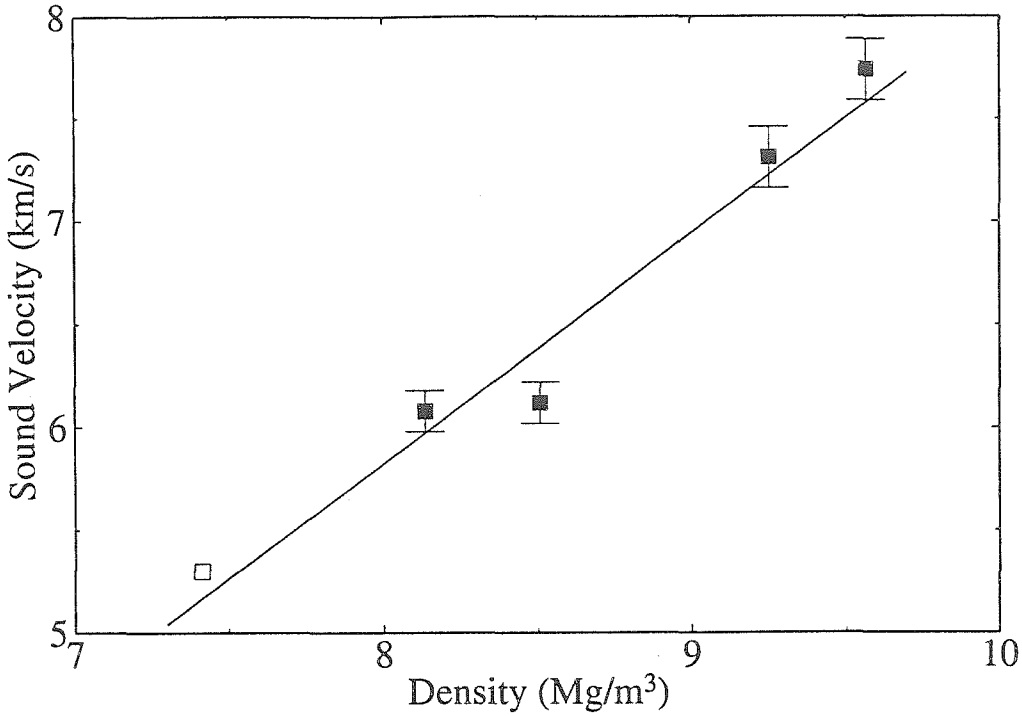

Figure 3.14: Sound velocity versus density for shocked γ-iron initially at 1573 K. The open square is calculated from *Boehler et al.* [1989]; the solid squares are from this study.

3.4.3 Grüneisen Parameters of the Liquid and γ-Phase

From our linear relationship between shock-wave velocity u_S and particle velocity u_P (Equation 3.1), the Grüneisen parameter γ for liquid iron can be calculated from the bulk sound velocity V_b using the following equation [*Brown and McQueen*, 1986]:

$$\gamma = \frac{\rho_0[1 + s\eta + R^{*2}(s\eta - 1)]}{\rho s\eta^2} \tag{3.30}$$

where $\eta = u_P/u_S$, $R^* = \rho V_b/(\rho_0 u_S)$. This equation was derived by noting:

$$\left(\frac{\partial E}{\partial P}\right)_V = \frac{(\partial E/\partial V)_H - (\partial E/\partial V)_S}{(\partial P/\partial V)_H - (\partial P/\partial V)_S}, \tag{3.31}$$

where the subscripts H and S indicate the derivatives are evaluated along the Hugoniot and the isentrope, respectively. The Rankine-Hugoniot relations are used for evaluating the derivatives to yield Equation 3.30.

The present value of V_b=6.55 km/sec gives γ=1.63$\pm$0.28 at $\rho = 9.37 \pm 0.02$ g/cm^3,

Table 3.8: The thermodynamic Grüneisen parameter for liquid iron.

P (GPa)	ρ (Mg/m^3)	γ	Reference
10^{-4}	7.019(0.002)	1.72(0.11)	*Anderson and Ahrens* [1994]
0.2	5.5	1.34(0.27)	*Hixson et al.* [1990]
0.2	6.0	1.55(0.31)	*Hixson et al.* [1990]
0.2	6.5	1.75(0.35)	*Hixson et al.* [1990]
71.6(1.0)	9.37(0.02)	1.63(0.28)	This study
277.4(18.4)	12.64(0.35)	1.42(0.27)	*Brown and McQueen* [1986]
331.5(9.4)	13.02(0.08)	1.40(0.27)	*Brown and McQueen* [1986]
397.1(10.2)	13.42(0.08)	1.30(0.27)	*Brown and McQueen* [1986]

which is comparable with *Brown and McQueen* [1986]'s data of $\gamma \sim 1.5$ for liquid iron in the density range of 12 to 14 Mg/m^3, and *Hixson et al.* [1990]'s liquid iron data between 5.5 and 6.5 Mg/m^3 (Table 3.8, Figure 3.15). The present result yields $\gamma\rho$=15.2±2.6 Mg/m^3, which is within the bounds of *Brown and McQueen* [1986] (13.3–19.6 Mg/m^3).

Since the longitudinal sound velocity V_p is measured for the solid γ-phase, the above equation cannot be used unless the Poisson's ratio ν is known and V_b can be derived from V_p (Equation 3.24). Poisson's ratio is strongly dependent on pressure and has been modeled in *Falzone and Stacey* [1980]. However, we found the value of γ varies drastically with small changes in ν. Therefore, determination of γ-phase Grüneisen parameter with pressure is not attempted.

3.5 Application to the Earth

Seismic data indicate that the Earth's outer core (at pressures of 136 to 329 GPa) has liquid properties and that the inner core (above 329 GPa) is solid. The calculated ϵ-iron densities just below melting temperatures at inner core pressure are a few percent higher than the PREM model [*Dziewonski and Anderson*, 1981] densities. *Jephcoat and Olson* [1987] suggested that the inner core must contain a few percent of a light element such as sulfur. A light component reduces both the iron density and the melting temperature. The degree of eutectic melting depression is uncertain.

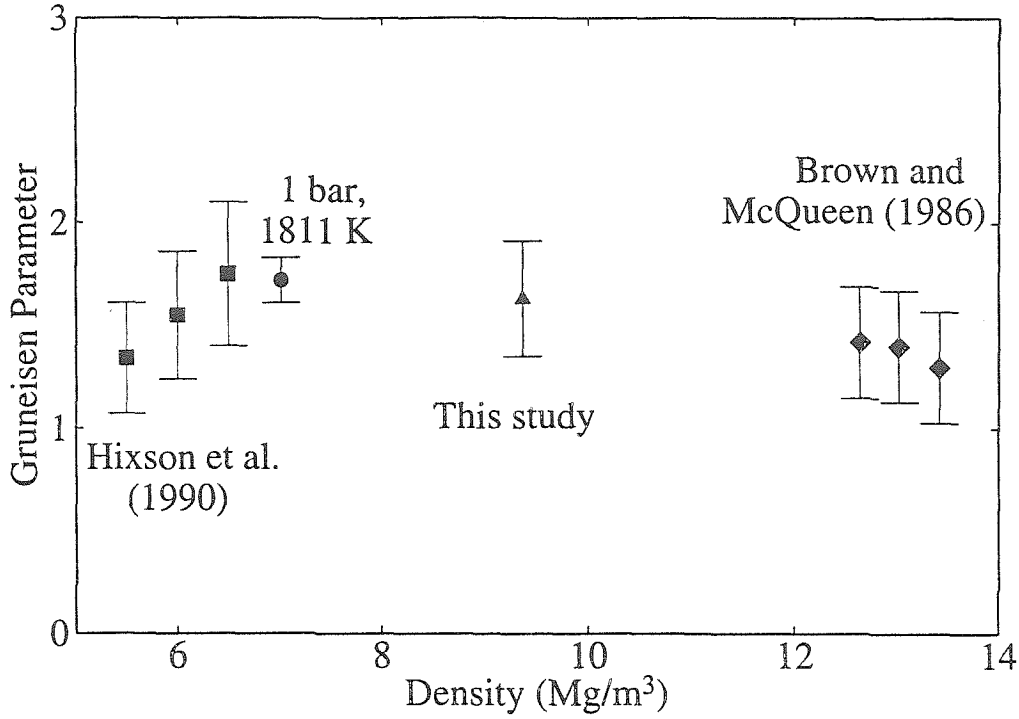

Figure 3.15: Thermodynamic Grüneisen parameter γ of liquid iron versus density. The 1 bar, 1811 K datum is from *Anderson and Ahrens* [1994].

However, the work of *Anderson and Ahrens* [1996] for melting point depression of FeO, FeS, and FeS_2, and *Holland* [1997] for Fe-Cr-Ni indicate that this depression is in the 500–1000 K range. Based on *Boehler* [1993]'s extrapolation of iron's melting curve in Figure 2.2 to higher pressures, we suggest that the inner core temperature is 5500±400 K.

The core-mantle temperature on the outer core side must be higher than the melting temperature at 136 GPa, *i.e.*, in excess of 3700±200 K. Another estimate can be obtained by isentropically decompressing liquid iron alloy from its melting point at the ICB to the CMB using Equation 2.11. The base of the approximation is that the outer core material convects closely following the isentrope. In Equation 2.11, T_0 is the ICB temperature (5500±400 K), and the density profile in the outer core is given by the PREM model, and $\gamma = 1.63 \pm 0.28$ (this study) and assumed to be constant with density as the dependence is much weaker than ρ^{-1} (Figure 3.15). Such calculated temperatures in the outer core are shown in Figure 3.16. The CMB temperature is estimated at 3930±630 K. For comparison, the melting curve of iron

under outer core pressure is calculated according to the Lindemann law [*Poirier*, 1991]:

$$\frac{d\ln T_m}{dP} = \frac{2}{K_S}(\gamma - \frac{1}{3}), \tag{3.32}$$

where Tm is the melting temperature. γ and K are parameters for the solid phase (possibly the β-phase). In absence of the data, we used values of K_{0T}, K'_{0T} and calculated γ=1.57 (Equation C.5) for ϵ-iron (Table 2.1). The result is shown in Figure 3.16 as the dotted line. This extrapolation could be further lowered by melting point depression from alloying.

Temperature is relatively well determined in the crust and the upper mantle. The mantle geotherm consists of adiabatic regions in which the temperature only increases slightly with depth and of thermal boundary layers in which large increases in temperature occur over a few hundred kilometers depth interval. Two geotherms are shown in Figure 3.16 ("hot" and "cold") as given in *Jeanloz and Morris* [1986]. Temperature in the mantle is calculated from the pressure of the α to β transition of $(Mg_{0.9}Fe_{0.1})SiO_4$ that is correlated with the sharp increase of ~6% of longitudinal wave velocity at a depth of ~400 km (this depth varies little over the various regions of the Earth except within subduction zones, where it occurs at lower pressures and temperatures (shallower depths)), giving rise to the "cold" limb of the convecting adiabatic mantle profile of Figure 3.16. The "hot" limb which is less well defined corresponds to regions of low P-wave velocity in the lower mantle such as occur beneath the SW Pacific [*Woodhouse and Dziewonski*, 1984; *Williams and Garnero*, 1996] that may correspond to higher heat flow possibly associated with upwelling lower mantle material. The "cold" geotherm gives the temperature $T_{\rm CMB}$ at the top of the mantle boundary (D″) layer of about 2500 K, the "hot" geotherm increases the temperature in the lower mantle by 500-1000 K. Other estimates of the $T_{\rm CMB}$ range from 2550 to 2750 K [*Shankland and Brown*, 1985; *Boehler*, 1982]. From $T_{\rm CMB}$ and our estimate of the outer core temperature, we suggest a thermal boundary layer difference that could range from 400 to 1400 K at the core-mantle boundary.

We note *Holland* [1997] gave somewhat different estimates of the core tempera-

tures (Figure 3.16). The melting temperature of iron at 243 GPa along its principal Hugoniot was measured and extrapolated to 329 GPa using the Lindemann law. A temperature of 6200±400 K was inferred for the ICB. The temperature at the top of the outer core was then inferred by adiabatic decompression to be 5100±400 K. This yields a thermal boundary layer temperature difference of up to 2600 K at the CMB.

3.6 Conclusion

Preheated EOS and VISAR experiments are proven to be valuable techniques to obtain absolute values of sound velocities in the γ- and liquid-phases and hence melting of iron. Our data suggest that γ-iron preheated to 1573 K melts at 70±2 GPa and 2775±160 K. In agreement with the Gibbs energy calculations, our experimental results are compatible with *Saxena et al.* [1993]; *Boehler* [1993]'s melting curve. Grüneisen parameter for liquid-phase at 71.6 GPa is determined to be 1.63±0.28.

Based on extrapolation of *Boehler* [1993]'s melting curve, we estimate the inner core temperature to be 5500±400 K, and the core-mantle temperature on the outer core side is about 3930±630 K. The latter gives a thermal boundary layer ranging from 400 to 1400 K at the core-mantle boundary.

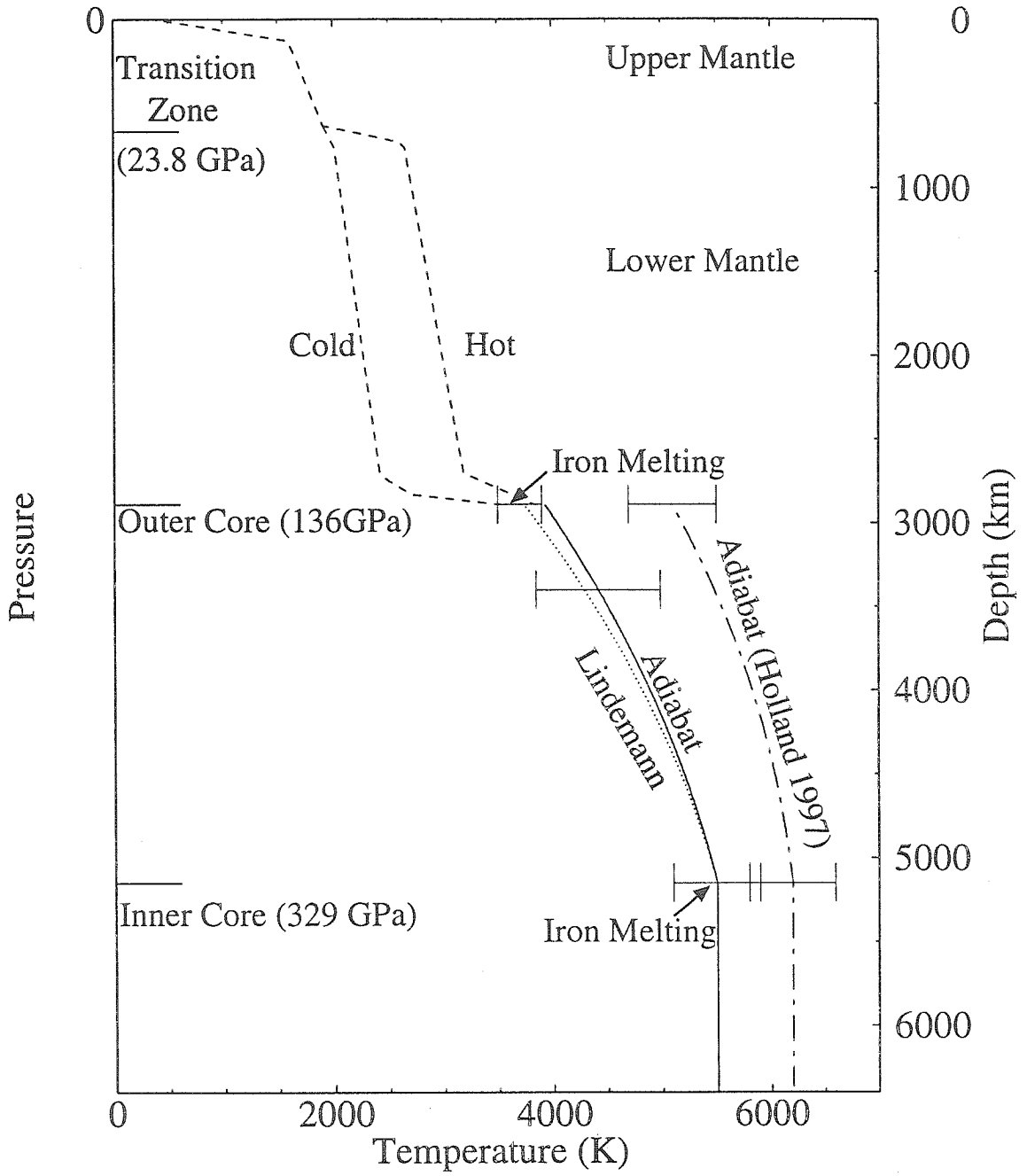

Figure 3.16: Summary of experimental constraints on the present, horizontally averaged temperature as a function of depth (geotherm) and pressure through the crust, mantle and core. See Section 3.5 for discussion of the "hot" and "cold" geotherms. The geotherms in the crust and mantle are from *Jeanloz and Morris* [1986]. The geotherms in the outer core were calculated along liquid iron's isentrope centered at *Boehler* [1993] and *Holland* [1997]'s melting temperatures of iron at the ICB pressure. The dotted line in the outer core is iron's melting curve calculated from the ICB temperature according to Lindemann law. Note that it is at lower temperature than the adiabat.

Chapter 4 Shock-Wave Equation of State of Fayalite

4.1 Abstract

The shock-wave equation of state of initially solid (300 K) and molten (1573 K) fayalite (Fe_2SiO_4, Fa) are reported in the ranges 23 to 212 GPa and 5 to 47 GPa, respectively. The 300 K data appear to undergo a phase change in the 35–55 GPa range. The density of the high pressure phase (HPP) is consistent with a dense oxide mixture. Although the initially 300 K fayalite may melt along its Hugoniot, this is not explicitly detected. Fitting the HPP Hugoniot data in the shock velocity (u_S)-particle velocity (u_P) plane yields:

$$\rho_0 = 4.375(0.027)\ \mathrm{Mg/m^3}, \tag{4.1}$$

$$u_S = 4.07(0.22)\ \mathrm{km/s} + 1.43(0.06)\ u_P, \tag{4.2}$$

where ρ_0 is the initial density. The isentropic bulk modulus $K_{0S} = 72.4 \pm 8.0$ GPa, and its pressure derivative K'_{0S}=4.72±0.24.

The 1573 K data set yields:

$$\rho_0 = 3.750(0.018)\ \mathrm{Mg/m^3}, \tag{4.3}$$

$$u_S = 2.63(0.02)\ \mathrm{km/s} + 1.59(0.01)\ u_P, \tag{4.4}$$

and $K_{0S} = 25.9 \pm 0.4$ GPa, $K'_{0S} = 5.36 \pm 0.04$. The bulk modulus compares favorably with *Agee* [1992a]'s result (24.4 GPa), but the pressure derivative is quite different

(10.1 from *Agee* [1992a]).

Above 50 GPa, the high pressure regime of the Hugoniot of the solid fayalite can be fit with oxide mixture models using stishovite and FeO (either LPP or HPP). The fayalitic liquid compression data above 40 GPa are well fit with ideal mixing of partial molar volumes of stishovite and FeO (LPP or HPP), in support of the hypothesis of *Rigden et al.* [1989].

A model basalt incorporating the liquid fayalite data shows the neutral buoyancy zone of basic silicate melts of plausible terrestrial compositions is at about 250–400 km depth based on the PREM Earth model.

4.2 Introduction

The densities of silicate melts at high pressures provide important constraint as to the nature of igneous processes at depth in the Earth and other planets [*Rigden et al.*, 1984, 1988, 1989; *Miller et al.*, 1991a, b; *Rowan*, 1993; *Agee and Walker*, 1988a, b; *Agee*, 1990, 1993; *Agee and Walker*, 1993] and into the structural changes that melts undergo with increasing pressure [*Waff*, 1975; *Matsui and Kawamura*, 1980, 1984; *Matsui et al.*, 1982; *Ohtani et al.*, 1985; *Stolper and Ahrens*, 1987]. At 1 bar, melt densities are well modeled by linear (*i.e.*, ideal) mixing of the volumes of oxide components except for Fe_2O_3, Al_2O_3, and SiO_2 (stishovite), and possibly TiO_2 [*Bottinga and Weill*, 1970; *Lange and Carmichael*, 1987]. It is likely that in these exceptional cases the cation is tetrahedrally coordinated in the melt at low pressures but the crystalline oxide is based on octahedral coordination. Available data [*Rigden et al.*, 1989; *Miller et al.*, 1991a] suggest that this is a good approximation at elevated pressures as well. If this approximation is valid, then the densities of silicate melts at high pressures can be calculated given measurements of the volumes of selected liquid end members. A particularly important end member is the fayalite component because naturally occurring basic to ultrabasic liquids, particularly those in equilibrium with the mantle at high pressure, are typically rich in normative olivine. Moreover, it has been suggested that fayalite liquid [*Jackson et al.*, 1993] and glass [*Williams et al.*,

1990] undergoes interesting structural changes with increasing pressure, whereby the Fe^{2+}, predominantly tetrahedrally coordinated by oxygen at low pressures [*Jackson et al.*, 1993], undergoes, like Si^{4+}, a change to predominantly octahedral coordination at elevated pressures (Mg^{2+} in $MgSiO_3$ and Mg_2SiO_4 liquids and glasses at 1 bar are also tetrahedrally coordinated with oxygen [*Waseda and Toguri*, 1977; *Yin et al.*, 1983; *Kubicki and Lasaga*, 1991] and have been suggested to transform to octahedral (or higher) coordination at higher pressure [*Kubicki and Lasaga*, 1991]); If this model is correct, this effect will have a significant signature in the pressure-density systematics of molten Fe_2SiO_4, which will be of importance in precise modeling of the densities of silicate melts at depth in the Earth.

The behavior of the fayalite liquid component has been somewhat controversial. Calculations based on partial molar volumes of oxides by *Bottinga and Weill* [1970] and *Bottinga et al.* [1982] yield the isothermal bulk modulus ranging from 25.6 to 44 GPa. *Herzberg* [1987a] suggested K_{0T}=33±2 GPa and K'_{0T}=4 as the optimal parameters to fit experimental data of fayalite's fusion curve below 10 GPa [*Lindsley*, 1967; *Akimoto et al.*, 1967; *Ohtani*, 1979]. A lower K_{0T} (as low as 28.3 GPa) and higher K'_{0T} (7) yields a melting curve which is also compatible with the experimental fusion curve but was deemed unlikely by *Herzberg* [1987a]. *Herzberg* [1987b] further calculated that olivine crystals would be denser in naturally occurring magmas at about 8 GPa. This calculation was contradicted by *Agee and Walker* [1993]'s experiments of olivine flotation in komatiite, which appeared to be more compressible than *Herzberg* [1987b] calculated, in agreement with the equation of state determined with shock-wave experiments [*Miller et al.*, 1991a]. Using ultrasonic measurements, *Rivers and Carmichael* [1987] obtained K_{0S}=21.4 GPa for molten fayalite; *Rigden et al.* [1989] suggested, based on their study on anorthosite-diopside, that fayalitic liquid density should approach the ideal mixing density of dense-packed oxides (FeO and stishovite) at about 40 GPa. Such derived K'_{0T} is 11.2 with K_{0T} = 20.5 GPa; *Agee* [1992b] determined from his "sink and float" experiments K_{0T} = 24.4 GPa and K'_{0T}=10.1 (all values are for temperature of 1673 K, except *Agee* [1992b]'s data were obtained at 1773 K). The density of fayalitic liquid under high pressure is central to

the hypothesis by *Stolper et al.* [1981] that olivine crystals are neutrally buoyant in basic melts in the upper mantle which, in turn, is important to the understanding of the early differentiation of a molten chondritic Earth and the formation of olivine-rich shallow mantle.

Shock-wave techniques have been demonstrated to provide determination of the densities of silicate melts at elevated pressure and temperature [*Rigden et al.*, 1984, 1988, 1989; *Miller et al.*, 1991a, b; *Rowan*, 1993] and thus are expected to help resolve the issues surrounding the equation of state of the fayalitic liquid component mentioned in the previous paragraph.

In this chapter, we describe experiments to determine the equations of state of fayalitic liquid shocked to pressures of up to 47 GPa from an initial state of 1573 K, 1 bar and of single crystal fayalite shocked to pressures of up to 212 GPa from an initial state of 300 K, 1 bar. We then compare our results with previous determinations and apply them to predication of the densities of basic to ultrabasic silicate melts at depth in the Earth.

4.3 Sample Preparation

The single crystalline samples were grown at Oak Ridge National Laboratory [*Finch et al.*, 1980]. Their composition, determined by electron microprobe analysis, are reported in Table 4.1.

In our previous shock-wave experiments on liquid silicates, the starting material was a silicate glass, obtained by mixing and fusing oxides. These were generally simple to prepare and to obtain homogeneous chemistry [*Rigden et al.*, 1989; *Miller et al.*, 1991a]. However, fayalitic glass is difficult to prepare [*Kusabiraki and Shiraishi*, 1981; *Sur and Cooney*, 1989; *Williams et al.*, 1990; *Williams and Cooney*, 1990]. We instead developed a two-stage process: 1. Preparation of fayalite powder from the oxides, and 2. hot-pressing the powder into polycrystalline pellets.

Hematite (Allied Chemical, 99.0%) and quartz (Johnson Matthey, 99.999%) were first baked for 24 hr in alumina crucibles at 800°C to drive off moisture. The samples

were then transferred to desiccators that were evacuated immediately and left to cool for a few hours. The hematite and quartz were weighed out in several ~6 g batches, each matching the stoichiometry of fayalite to within 10 ppm. Each batch of quartz and hematite was then ground in ethanol in an agate mortar for about 5 hr. After drying the mixture with flowing air, it was pressed into pellets (about 1.2–1.5 g each) in an evacuated stainless steel die using a hydraulic press at a stress of about 40 bars for a few minutes; ethanol or distilled water were used as "binders" in this process. The pellets were then sintered (up to 4 at a time) for 1 day in an MgO boat at 1273 K (this temperature is high enough to allow reaction to fayalite via solid-state diffusion). The sintering was conducted at 1 bar, at an oxygen fugacity intermediate between the iron-wüstite (IW) and the quartz-fayalite-magnetite (QFM) buffer, controlled by an H_2-CO_2 gas flow [*Sato*, 1970]. The sintered product was ground to powder, pressed into pellets, and sintered again. After three cycles of pelletizing, sintering and grinding (the last grinding was in distilled water), the powder was commercially hot-pressed (Cercom Inc., Vista, CA) in a carbon crucible at 1273 K at a pressure of 345 bars for about 30 min.

SEM images of the samples before and after hot-pressing are shown in Figures 4.1 and 4.2. The hot-pressed disks have a bulk density of 4.25 Mg/m^3, about 3% lower than the measured Archimedian density of 4.375 Mg/m^3 (measured with Toluene), and the value of 4.38 Mg/m^3 given by *Bass* [1995] or 4.402 Mg/m^3 given by *Smyth and McCormick* [1995], which was based on X-ray measurement of cell volume. Using Caltech's JEOL electron microprobe (JXA-733) and X-ray diffraction (XRD) to analyze these pellets, we found them to contain more than 90% fayalite. The major contaminants are SiO_2, FeO, and Fe, of which only Fe was not present in the pre-hot-pressed material. The reason is likely that f_{O_2} during hot-pressing, controlled by the graphite crucible, was lower than that of the iron-wüstite buffer at least at some locations. We infer the SiO_2, FeO, and Fe present were unreacted material as opposed to products of partial breakdown of fayalite as the quartz grain sizes were quite large (~10–100 μm). Although it appears there was an excess of quartz in the hot-pressed material (Figure 4.3), an accurate mineral inventory is difficult to com-

pile from SEM images as Fe and FeO grains were much smaller and more scattered than SiO_2 grains. However, the samples were all pre-melted in a pre-heating step (see below) and became much more homogeneous. All unreacted grains disappeared. The composition of pre-heated samples was measured and found to be very close to the theoretical stoichiometry.

The hot-pressed fayalite disks were cored into pellets of about 1 cm in diameter and 3 mm in thickness, and placed into molybdenum capsules for the experiments. The capsules were electron-beam-welded commercially (Advanced Technology Co., Pasadena, CA), using the procedure described in [*Rigden et al.*, 1989]. Prior to mounting in the experimental assemblies, the welded capsules were heated in a furnace at 1573–1673 K at an oxygen fugacity two log units below IW for 20 minutes in order to melt the enclosed fayalite and to test for leakage. After cooling to room temperature, some of the capsules were cut open to determine the degree of interaction between the fayalitic liquid and the molybdenum container. The quenched fayalitic liquid and the molybdenum capsule were both analyzed using a Tracor Northern detector (TH-3/54-6901, operated at 15 kV) attached to an SEM. The composition of the bulk sample after the heating step is quite homogeneous except some interstitial phases which represent a very small percentage (estimated < 1 vol.%) of the material (Table 4.1). The presence of a 10 μm thick, Fe-enriched boundary at the edge of the Mo capsule demonstrates that interactions between the capsule and sample occurred on the time scale of this heating step. The layer has a well-defined boundary and the Fe content within the layer is quite uniform (Fe/Mo atomic ratio$\sim$1), indicating a separate, intermetallic phase. We also observed the alloyed layer breaking off from the capsule edge at some places. The amount of FeO lost from the sample, calculated from mass balance based on the analysis of the inner surface area of the capsule amounts to only 0.3 wt.% of that in the starting material. No presence of molybdenum was detected in the fayalite crystals; however, it is possible that molybdenum is concentrated in the interstitial phases, which were not examined.

The capsules were underfilled with the cored, hot-pressed fayalite because we found that when they were nearly filled initially, the capsule bulged and sometimes

Table 4.1: Compositions of single crystalline fayalite samples for 300 K experiments and polycrystalline samples for 1573 K experiments after heating in Mo containers, in weight percentage determined from microprobe analysis.

Oxides	Single Crystal[1]	Polycrystal[1]	Theoretical
Na_2O	—	0.15	
MgO	0.00	0.05	
Al_2O_3	0.08	0.17	
SiO_2	31.09	28.10	29.49
K_2O	—	0.02	
CaO	0.00	0.02	
TiO_2	0.00	0.19	
FeO	71.30	70.89	70.51
Cr_2O_3	0.03	0.09	
MnO	0.02	0.07	
NiO	0.00	0.04	
Total	102.52	99.79	100.00

1. Averaged from 6 spots each. For polycrystalline fayalite, the measurements were made using a focused beam on homogeneous portions of several samples, percentages of SiO_2 and FeO varied by ±1%.

even burst. Despite being underfilled, after the preheating there was usually a slight bowing of the capsule cap. The cap was always repolished after preheating to remove any curvature; this led to a thickness difference between the edge and center of the molybdenum cap of about 0.3 mm. The effect of this thickness difference on the shock record is discussed below.

Because of the underfilling, the capsules initially contain voids, most of which accumulated into a large (on the order of mm in diameter) bubble near the part of the capsule that was at the top during the preheating. This bubble, unlike the micro-cavities in Figure 4.3 which are presumably quench products, if positioned in the portion of the target viewed by the streak camera, would greatly affect the shock arrival time *Miller et al.* [1991a]. Consequently, we developed a screening method using flash X-ray radiographs to locate these bubbles in the preheated samples so as to avoid them in the actual experiments; the image of one capsule with a large bubble is shown in Figure 4.4. The obvious advantage of this technique, compared with the earlier examination method of cutting open sample capsules, is the test is

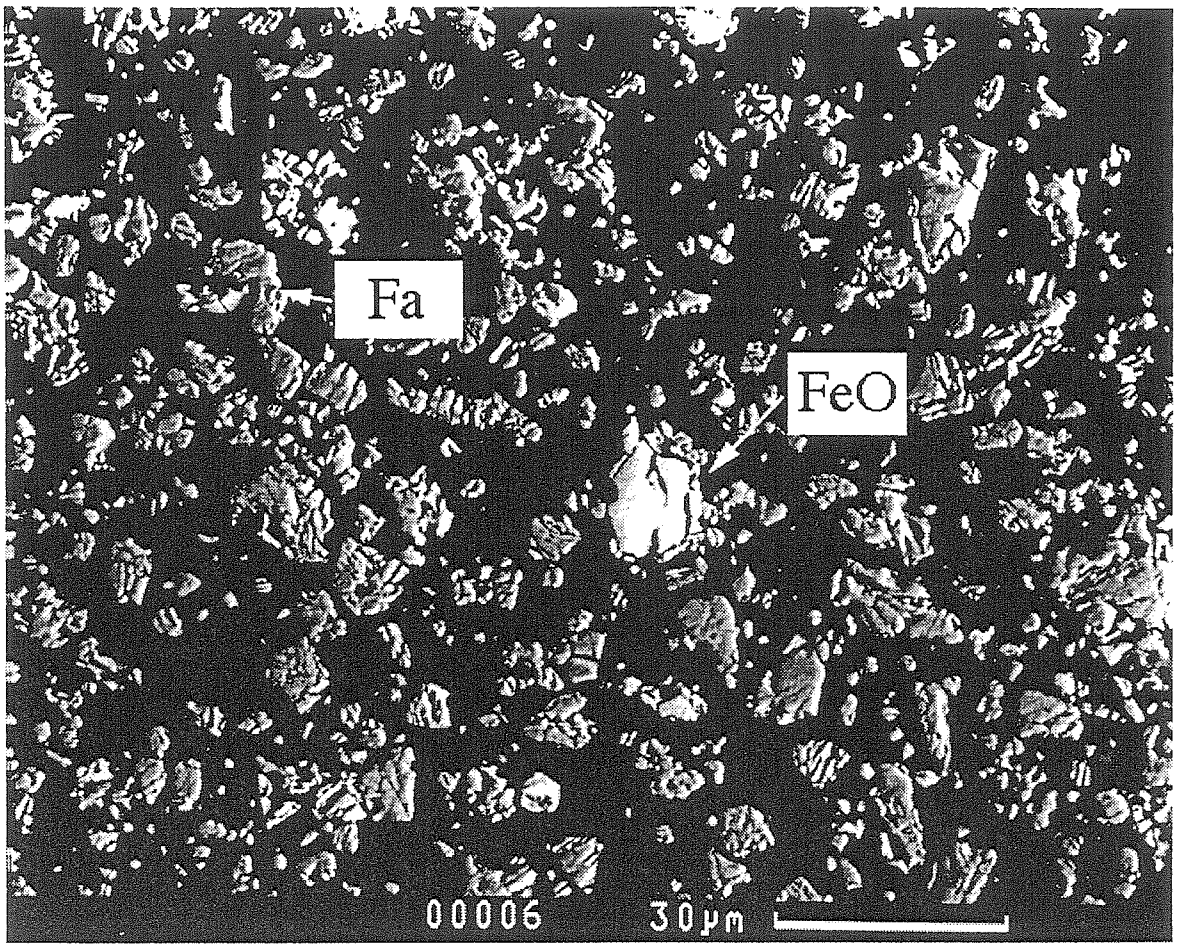

Figure 4.1: Scanning electron microscope (SEM, model Camscan Series II) image of synthesized fayalite powder, before hot-pressing. There is also unreacted quartz in the material (but not present in this image). The black area is epoxy used for SEM mounting.

non-destructive and thus can be applied to the actual samples used in the experiments.

4.4 Shock-Wave Techniques

Shock-wave experiments were performed at Caltech in the pressure range of 5–212 GPa either on the 40 mm propellant gun or the two-stage light gas gun. Equation of state parameters of the standard materials used in the experiments are listed in Table 4.2.

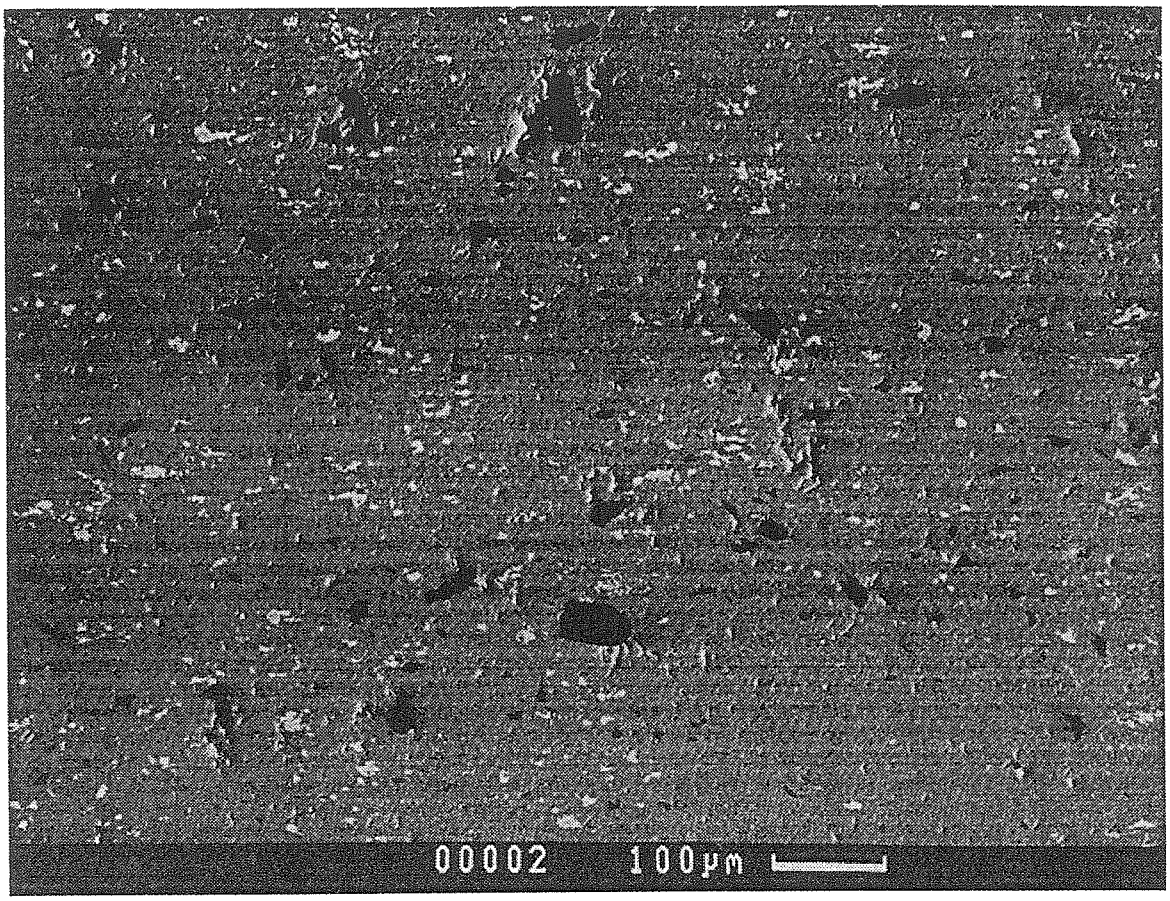

Figure 4.2: SEM image of fayalite sample after hot-pressing, matrix is fayalite, light contrast grains are Fe or FeO, and black grains are SiO_2.

Table 4.2: Equation of state parameters of some standard materials used in the present study.

Material	ρ_0 (Mg/m^3)	c_0 (km/s)	s	Note
Al2024	2.784(0.005)	5.330(0.050)	1.34(0.02)	
W	19.235	4.040	1.23	
Cu	8.930	3.940	1.489	
Ta	16.650	3.293	1.307	
Lexan	1.193(0.002)	2.449(0.044)	1.498(0.003)	$u_P < 2.605$ km/s, $u_S < 6.351$ km/s
FQ[1]	2.204	1.086	1.599	
Mo	9.95	4.78	1.42	1673 K

1. Fused quartz.

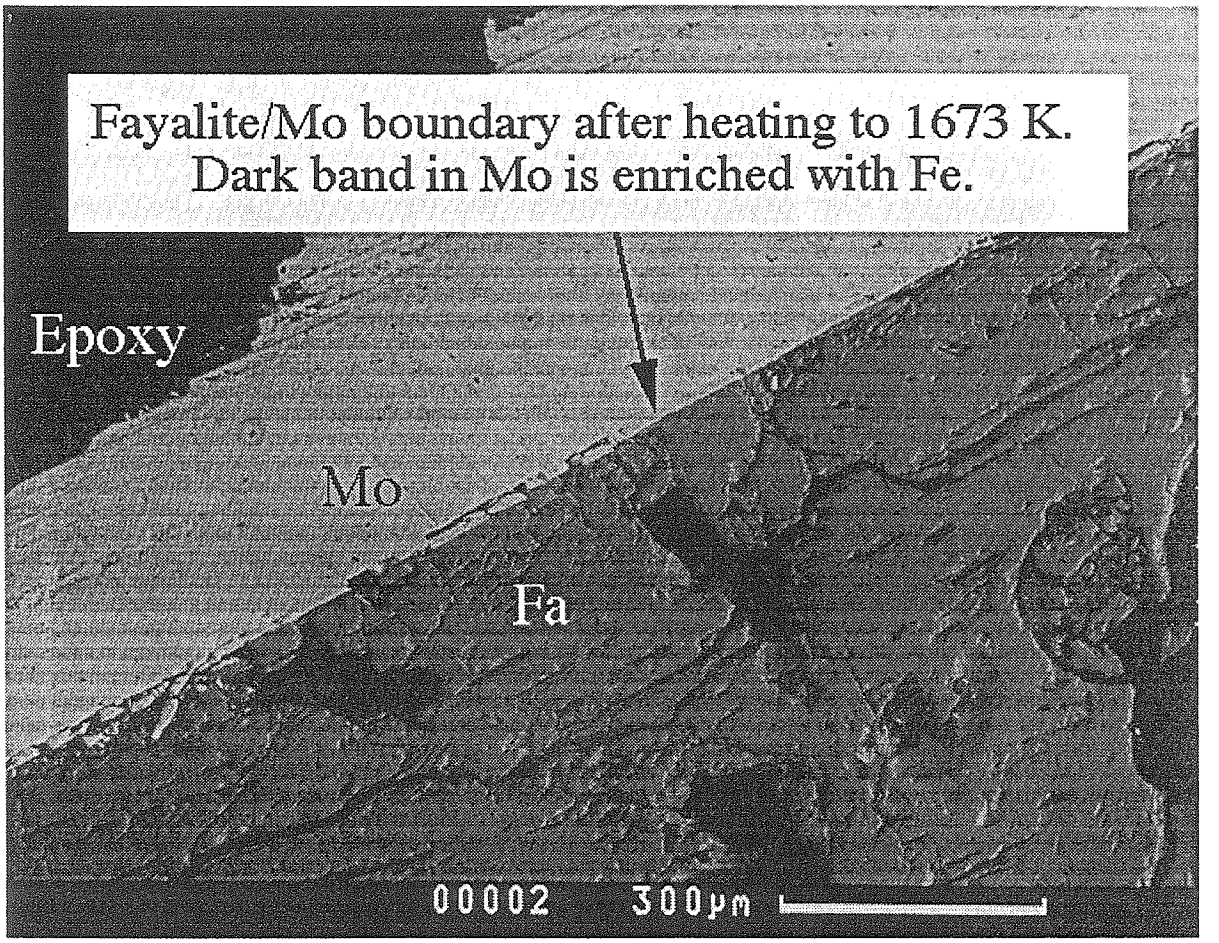

Figure 4.3: SEM image of fayalite sample after pre-melting in a molybdenum capsule. The quenched melt is homogenized fayalite, with some micro-cavities which probably resulted from the quench.

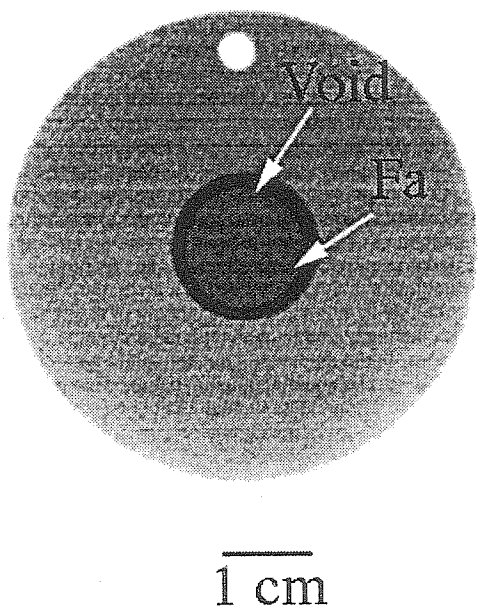

Figure 4.4: X-ray radiograph of fayalite sample/molybdenum capsule used in experiment 998 before the experiment. The lighter area inside the inner circle is a void. Target is maintained at upright position for shock experiment. The X-ray tube used is Hewlett Packard model #130-529000 charged to 105 kV. Welded and preheated capsules are place 16 cm in front of the tube head, and shadow graphs are recorded on ASA3000 Polaroid films.

4.4.1 Experiments on Single Crystal Fayalite Initially at 300 K

Aluminum-coated mirrors (with fused quartz or lexan backings) were epoxied onto the rear surface of the fayalite samples, each of which was mounted such that the shock propagation direction would be in the direction of the *a* axis. A Beckman & Whitley streak camera (on the 40 mm gun) and a TRW image converter streak camera (on the two-stage light-gas gun) recording at 3 and 25 mm/μs writing rate were used to record reflected light from the surfaces of the mirrors (Figure 4.5). A prism in the Beckman & Whitley camera rotated continuously and the streak image of shock propagating in the sample was captured by using a laser interruption-triggered, 100 μs duration xenon flash lamp. The TRW camera was electrically triggered by shorting pins (Figure 4.5) about 0.2 μs before projectile impacts target, and about 50 μs after the xenon flash lamp was triggered by break-wire. The driver arrival mirrors and sample buffer were illuminated by the xenon lamp. The reflected light was observed through a narrow (0.2 mm) slit by the cameras. Upon the arrival of the shock-wave, each mirror loses its specular reflectance. The light cutoffs on the streak camera film were used to measure shock velocities in the fayalite samples and in the buffers. Using the Rankine-Hugoniot equations [*Duvall and Fowles*, 1963], the shock and release states in the fayalite samples are calculated (Appendix B). Our techniques were described in greater detail in *Vassiliou and Ahrens* [1982] and *Ahrens* [1987].

4.4.2 Experiments on Fayalitic Liquid Initially at 1573 K

For each experiment, the target (fayalitic liquid within molybdenum capsules) was mounted in a ceramic holder and heated with an induction coil (Appendix A), powered by a 10 kW Lepel radio frequency heater. The gun tank vacuum was evacuated to below 100 μm Hg. In some experiments, a N_2-H_2 gas was bled into the tank near the target to inhibit surface oxidation; in these experiments, the tank vacuum was below 110μm. The coil design differed from that used in previous pre-heated experiments [*Rigden et al.*, 1984] in that 3 mm (outer diameter) copper tubing was used

Table 4.3: Shock experiments and results of fayalite at 300 K initial temperature.

Experimental Condition					Hugoniot State				Release State			
Shot	Flyer/ Driver Material	Buffer Material	Archimedian Density (Mg/m^3)	Impact Velocity (km/s)	Shock Velocity (km/s)	Particle Velocity (km/s)	Pressure (GPa)	Density (Mg/m^3)	Shock Velocity (km/s)	Particle Velocity (km/s)	Pressure (GPa)	Density (Mg/m^3)
999[1]	Al2024/ Al2024	Lexan	4.380 (0.002)	1.96 (0.001)	7.05 (0.26)	0.754 (0.02)	23.3 (0.4)	4.90 (0.03)	4.17 (0.73)	1.15 (0.49)	5.7 (3.9)	4.70 (0.87)
1000[1]	W/ Al2024	FQ[1]	4.386 (0.002)	2.03 (0.01)	6.95 (0.18)	1.51 (0.012)	46.2 (0.9)	5.61 (0.05)	4.63 (0.12)	2.21 (0.08)	22.6 (1.4)	5.03 (0.16)
110	Cu/Cu	FQ	4.394 (0.006)	4.63 (0.01)	8.20 (0.08)	2.87 (0.01)	103.3 (0.8)	6.76 (0.05)	7.62 (0.05)	4.10 (0.03)	68.9 (1.0)	5.19 (0.1)
120	Cu/Cu	FQ	4.360 (0.023)	5.30 (0.002)	8.71 (0.08)	3.29 (0.01)	124.7 (0.8)	7.00 (0.06)	8.71 (0.13)	4.79 (0.08)	91.9 (2.9)	4.7 (0.3)
116	Ta/Ta	FQ	4.380 (0.01)	5.171 (0.006)	9.02 (0.11)	3.58 (0.01)	141.4 (1.7)	7.26 (0.06)	9.16 (0.25)	4.87 (0.17)	98.17 (6.1)	5.68 (0.33)
113	Ta/Ta	FQ	4.390 (0.006)	5.38 (0.005)	9.44 (0.17)	3.69 (0.02)	153.0 (2.1)	7.21 (0.1)	9.39 (0.2)	5.22 (0.13)	108.0 (4.9)	5.24 (0.39)
099	Ta/Ta	FQ	4.378 (0.005)	5.77 (0.005)	9.79 (0.05)	3.95 (0.007)	169.4 (0.7)	7.34 (0.03)	9.19 (0.1)	5.09 (0.06)	103.2 (2.4)	6.41 (0.12)
107	Ta/Ta	FQ	4.393 (0.006)	6.25 (0.01)	10.15 (0.1)	4.27 (0.01)	190.5 (1.5)	7.59 (0.07)	10.4 (0.15)	5.86 (0.09)	134.2 (4.1)	5.67 (0.28)
161	Ta/Ta	FQ	4.364 (0.001)	6.494 (0.001)	10.33 (0.11)	4.44 (0.01)	200.3 (2.1)	7.65 (0.06)	— —	— —	— —	— —
126	Ta/Ta	FQ	4.389 (0.024)	6.51 (0.005)	10.57 (0.1)	4.57 (0.02)	211.9 (1.6)	7.73 (0.08)	10.56 (0.1)	5.96 (0.06)	138.7 (2.8)	6.40 (0.15)

1. 40mm shots on Caltech synthesized polycrystalline fayalite.

2. Fused quartz.

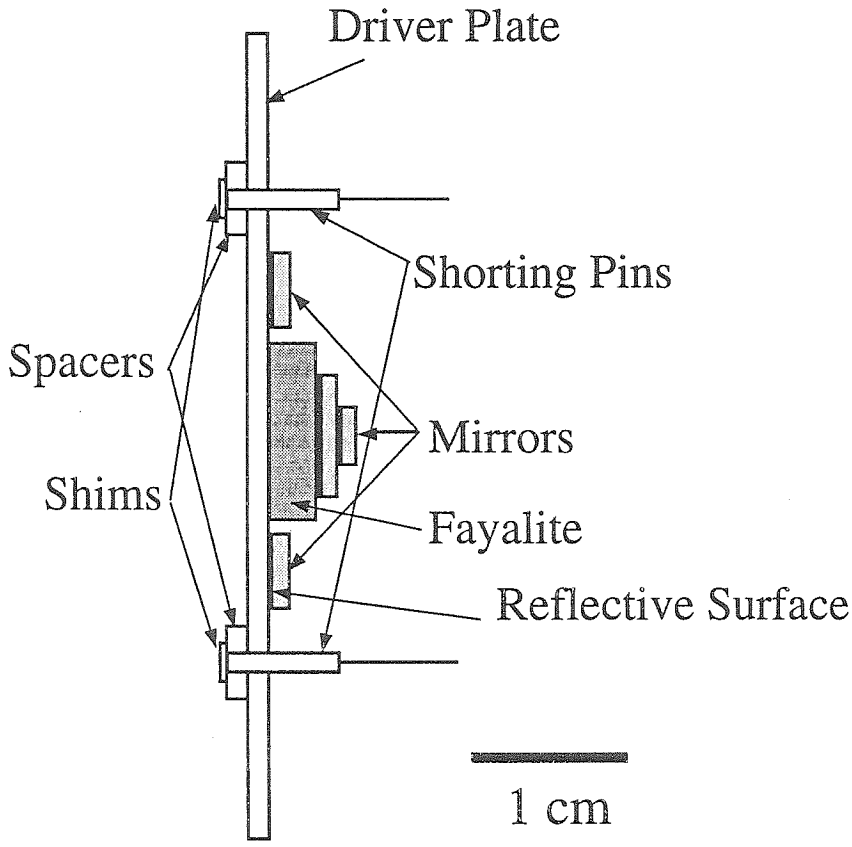

Figure 4.5: Fayalite sample assembly for 300 K initial temperature shock experiments. Specular reflectivity of mirrors was sharply reduced upon shock arrivals at the respective surfaces and were recorded as light cutoffs on streak camera record. When the projectile impacted the shims, the shorting pins activated a pulse forming circuit, and the electric pulses were used to determine projectile deformation and tilt, and trigger the TRW image converter camera on the light-gas gun.

to decrease the inner diameter of the coil to about 25 mm (Appendix A). We found this resulted in a more uniform temperature field in the target than in the configuration used by *Rigden et al.* [1984] and *Miller et al.* [1991a]. We also used a two-color pyrometer (Williamson 8120S-C-WD2) for temperature measurement instead of the previously used thermocouples since they are prone to break upon oxidation or reaction with molybdenum. At 1573 K, measurements with the pyrometer over the entire metal portion of the sample assembly indicated a temperature difference over the entire target was usually less than 30 K. The central portion, for which temperatures were reported, was more uniformly heated (within 10 K). The target assembly is shown schematically in Figure 4.6.

4.5 Experimental Results

4.5.1 Experiments on Single Crystal Fayalite Initially at 300 K

Results for compression of fayalite from 300 K are summarized in Table 4.3 and Figures 4.8 and 4.9. Results on natural, less pure, polycrystalline, Rockport fayalite [*Marsh*, 1980] are shown for comparison.

In the low pressure range ($P < 50$ GPa), shot 1000 (the filled square at higher u_P in Figure 4.8) agrees well with Los Alamos shock wave data for Rockport fayalite [*Marsh*, 1980], but shot 999 (the filled square at lower u_P in Figure 4.8) shows a higher shock velocity. We speculate that the disagreement is due to a higher yield strength in our sample (note the LASL material was natural and contained minor impurity minerals). The combined data set of our light gas gun, 40 mm gun experiments, and the *Marsh* [1980] data suggests the onset of a phase transition at about 35 GPa and is completed at about 55 GPa. *Bassett and Ming* [1972] reported fayalite breaks down to wüstite and stishovite when statically compressed to about 25 GPa and 3000°C. Shock-wave data, of course, do not give structural information of the high-pressure-phase, but it could be the same phase transition. The difference in pressure could be due to kinetics effects. *McQueen et al.* [1967] conducted shock-wave measurements on two

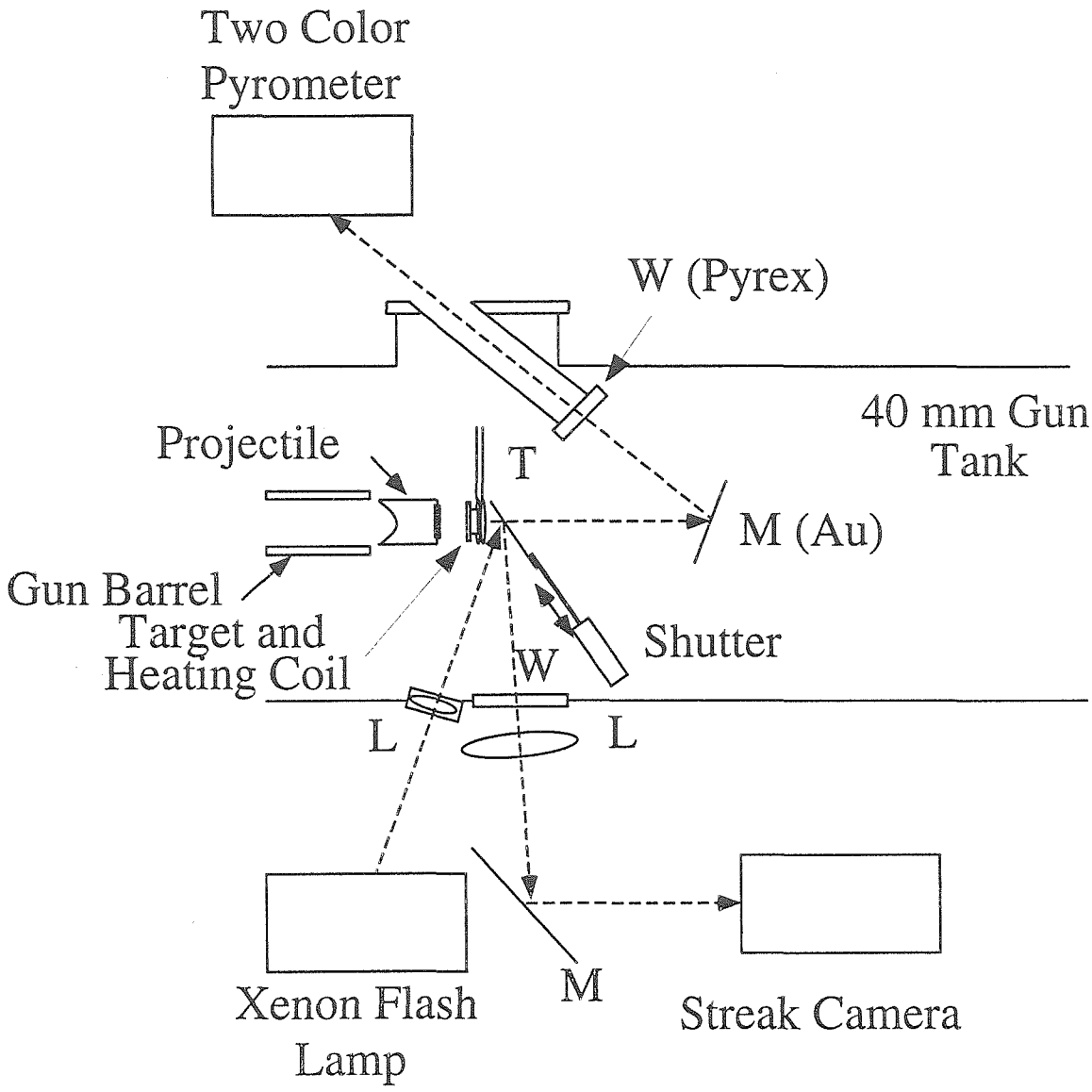

Figure 4.6: Experimental arrangement for the 1573 K shock-wave experiments. Symbols: *M*: mirror; *W*: window; *L*: lens. During heating, the compressed air driven shutter was retracted to protect the turning mirror, and allowed thermal radiation from the target to be reflected from the gold mirror to the pyrometer for temperature monitoring. The gold mirror and the Pyrex window ensured a nearly constant transmission of infrared radiation. When the target reached 1573 K, the shutter extended and placed the turning mirror into position, the projectile interrupted laser beams placed across holes in and immediately at the muzzle of the gun barrel (not shown). Signals from laser obstruction triggered the xenon flash lamp. The reflected light versus time from the polished rear surface of the target was recorded by the streak camera (Beckman & Whitley 339B).

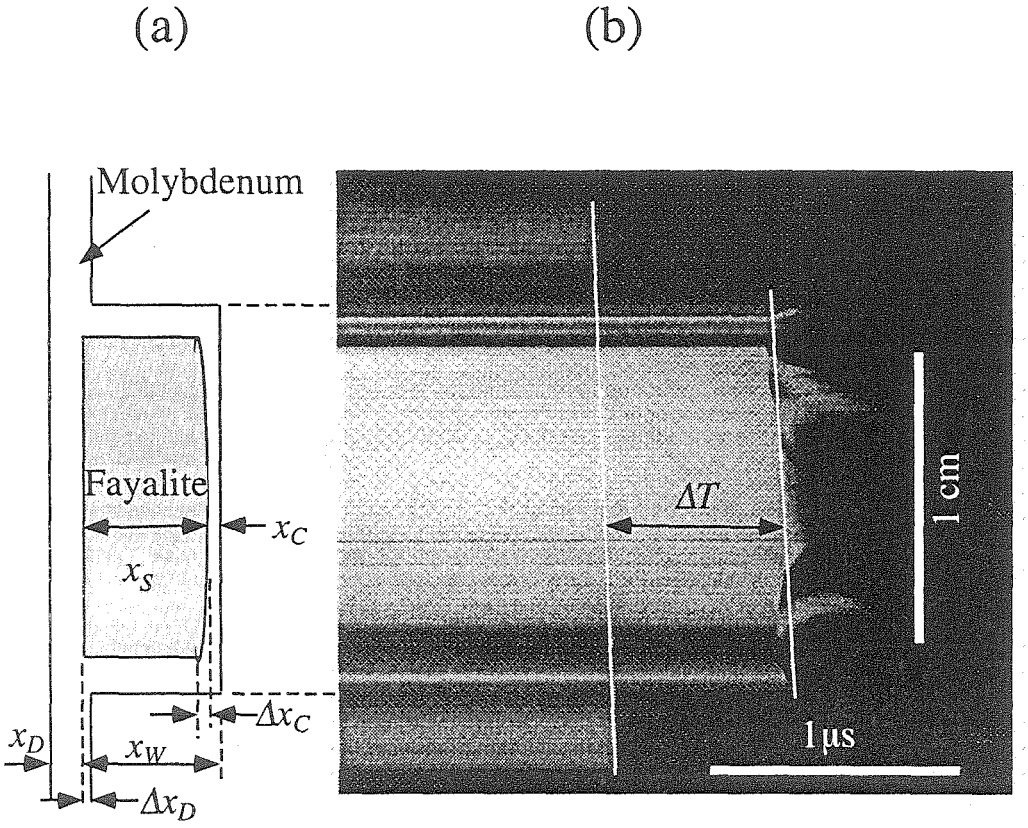

Figure 4.7: Streak camera record of experiment 998. Schematic of target is drawn to aid understanding of the streak record. Shock-wave propagated through extra distance of the fayalite capsule at the center of the target and its arrival on the rear surface of the Mo cover was delayed relative to that on the driver plate. This time difference is recorded on film as the longer middle streak. ΔT was used to derive shock velocity in the fayalite sample. See text for details.

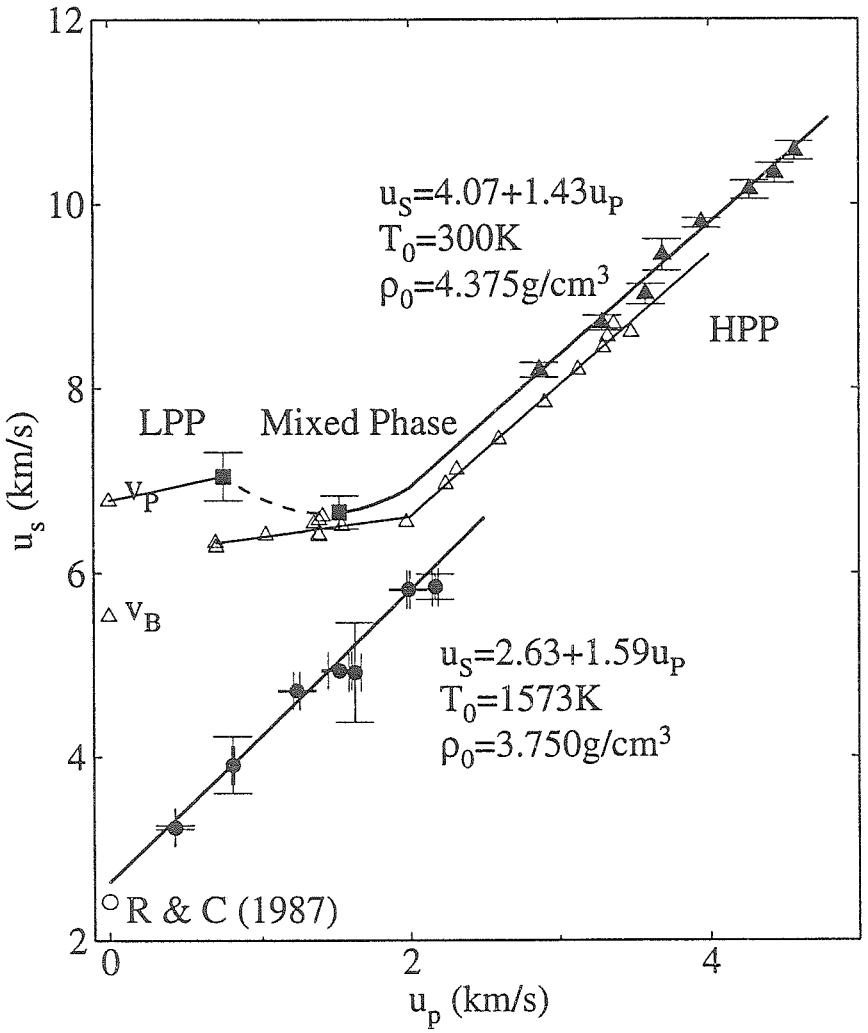

Figure 4.8: Experimentally determined u_S-u_P relation for solid (triangles) and molten fayalite (circles). Open triangles at $u_P > 0$ are LASL data [*Marsh*, 1980] on Rockport fayalite (ρ_0=4.245 Mg/m^3) and fit with $u_S = 3.77 + 1.42\ u_P$ for $u_P > 1.96$ km/s. Open triangles at $u_P = 0$ are compressional and bulk sound velocities of solid fayalite calculated from density and bulk and shear moduli data in *Bass* [1995]. Open circle at u_P=0 is interpolated ultrasonic data of *Rivers and Carmichael* [1987]'s two measurements on liquid fayalite at 1503 K and 1653 K. Filled symbols are data from this study: circles are experiments at an initial temperature of 1573 K, triangles are experiments on single crystal fayalite initially at 300 K, and squares are experiments using polycrystalline fayalite initially at 300 K.

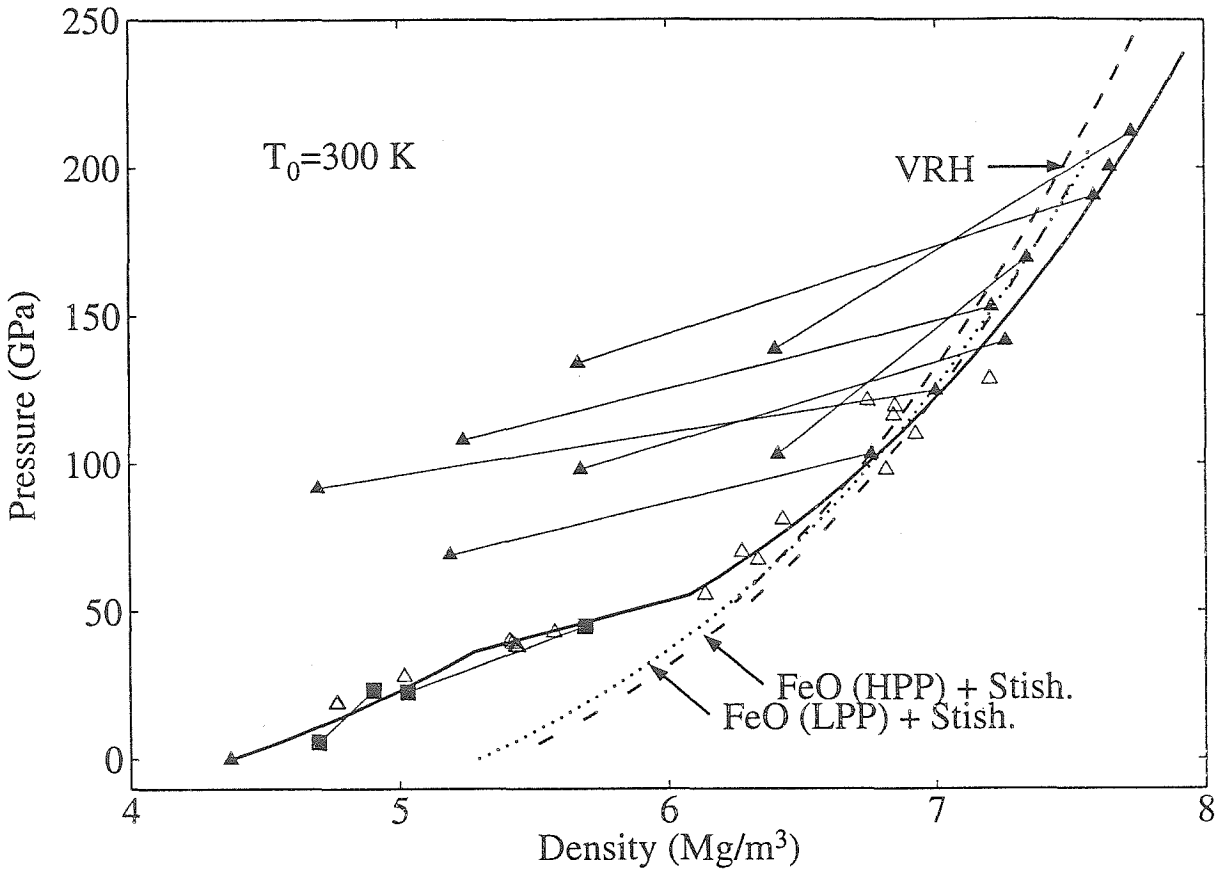

Figure 4.9: Shock-wave compression of fayalite at 300 K. Symbols have same meaning as in Figure 4.8. Lower pressure symbols of the connected pairs are release states. Three fits to the Hugoniot are shown: The curve labeled VRH is a VRH mixture of HPP FeO and stishovite, the other two curves are ideal oxide mixtures with correspondingly labeled components.

dunites, whose compositions are about 90% fayalite by molar fraction. Their data are not shown in Figure 4.8 because the initial densities of their samples (3.32–3.85 Mg/m^3) are significantly lower than fayalite crystal density, but they also observed a change of slope in the u_S-u_P relation corresponding to shock pressures in the 40–50 GPa range.

The release adiabat data shown in Figure 4.9 are associated with large uncertainties. The datum at 46.2 GPa lies close to the Hugoniot, indicating the phase change is reversible.

4.5.2 Experiments on Fayalitic Liquid Initially at 1573 K

Experiments were conducted at 1573 K because this initial temperature is about 900 K above the melting point of pure Fe_2SiO_4 (1478 K) and it was assumed that although the shock-temperature-pressure states may cross into the regime of solid media, the molten material would remain a super-cooled liquid as super-cooling is often observed in silicates. However, it should be noted that attempts to induce via shock amorphous Fe_2SiO_4 have been unsuccessful (Q. Williams, private communication).

Results of the seven successful experiments of fayalitic liquid are listed in Table 4.4. Reduction of the data measured on the streak records yielding shock velocities (Table 4.4) is based on the same principles as the room temperature experiments (Appendix B). There is, however, an added complexity that the cutoff interval ΔT measured from the streak camera film (Figure 4.7b) corresponds to the propagation of shock-wave through the molten fayalite sample and the Mo cover plate (Figure 4.7a). Also, due to polishing of the inside surfaces of the capsule, the thickness of the driver plate at the center of the capsule is slightly less than that outside. Therefore:

$$\Delta T = x_S/u_S^{Fa} + x_C/u_S^{Mo} - \Delta x_D/u_S^{Mo}. \tag{4.5}$$

We use the equation of state data of molybdenum at 1673 K (ρ_0=9.950 Mg/m^3, c_0=4.780 km/s, s=1.420) [*Duffy and Ahrens*, 1994a] for the driver plate and capsule cap. The temperature coefficient of compressional sound velocity is between 0.17–0.37

m/s/K in the 12–81 GPa pressure range [*Duffy and Ahrens*, 1994b], which we use as an estimate for the temperature coefficient of shock velocity. The 100 K difference in initial temperature gives a shock velocity difference of about $2\text{–}4\times10^2$ m/s. In the lowest pressure shot (#995) the corresponding difference in travel time through the Mo cap is less than 0.01μs. The difference decreases with shock pressure and is included in the uncertainties of the travel time measurements. The shock velocity and particle velocity reported in Table 4.4 are then calculated iteratively [*Miller et al.*, 1991a] as follows:

1. Measure the time interval indicated in Figure 4.7 as ΔT;
2. Assume an initial u_S-u_P relationship for the fayalite sample;
3. Calculate the impedance match solutions of shock pressure and particle velocity between the flyer and the molybdenum driver plate, the driver plate and the fayalite sample, and the fayalite sample and the molybdenum cap using the method outlined by *Miller et al.* [1991a];
4. Calculate travel times in the molybdenum cap, deduce this time from the total time as measured from streak camera record, compensate with the time due to thickness difference of the driver plate to obtain the shock travel time inside molten fayalite (Δt);
5. From Δt and the thickness of fayalite, calculate u_S and u_P for fayalite;
6. Repeat Steps 2–4 for each shot. From such obtained u_S-u_P pairs, update the linear relationship assumed in Step 1;
7. Repeat Steps 2–5 until c_0 and s converge satisfactorily. This usually takes 3–4 iterations.

The results are shown in Figures 4.8 and 4.10. There is some uncertainty in the measurement of the arrival time of the shock-wave after it has propagated through the liquid and Mo cap and this is discussed below.

Table 4.4: Hugoniot data for molten fayalite at 1573 K initial temperature.

Experimental condition				Hugoniot state			
Shot No.	Flyer/ Driver Material	Archimedian Density (300K)[1] (Mg/m^3)	Impact Velocity (km/s)	Shock Velocity (km/s)	Particle Velocity (km/s)	Pressure (GPa)	Density (Mg/m^3)
995	Al2024/ Mo	4.381 (0.004)	1.05 (0.004)	3.23 (0.02)	0.43 (0.002)	5.25 (0.03)	4.33 (0.01)
996	Al2024/ Mo	4.370 (0.004)	1.945 (0.01)	3.91 (0.31)	0.81 (0.01)	11.9 (0.7)	4.73 (0.12)
981	Ta/Mo	4.315 (0.001)	1.52 (0.02)	4.72 (0.01)	1.24 (0.02)	21.9 (0.3)	5.08 (0.03)
993	Ta/Mo	4.381 (0.002)	1.89 (0.002)	4.94 (0.01)	1.53 (0.08)	28.4 (1.5)	5.44 (0.14)
990	Ta/Mo	4.316 (0.002)	2.00 (0.01)	4.92 (0.54)	1.63 (0.04)	30.1 (2.5)	5.61 (0.34)
994	Ta/Mo	4.381 (0.004)	2.52 (0.01)	5.82 (0.01)	1.99 (0.01)	43.5 (0.2)	5.70 (0.02)
998	W/Mo	4.368 (0.001)	2.496 (0.01)	5.85 (0.14)	2.17 (0.02)	47.7 (0.9)	5.96 (0.10)

1. Initial density at 1573 K is 3.750±0.018 Mg/m^3 [*Shiraishi et al.*, 1978].

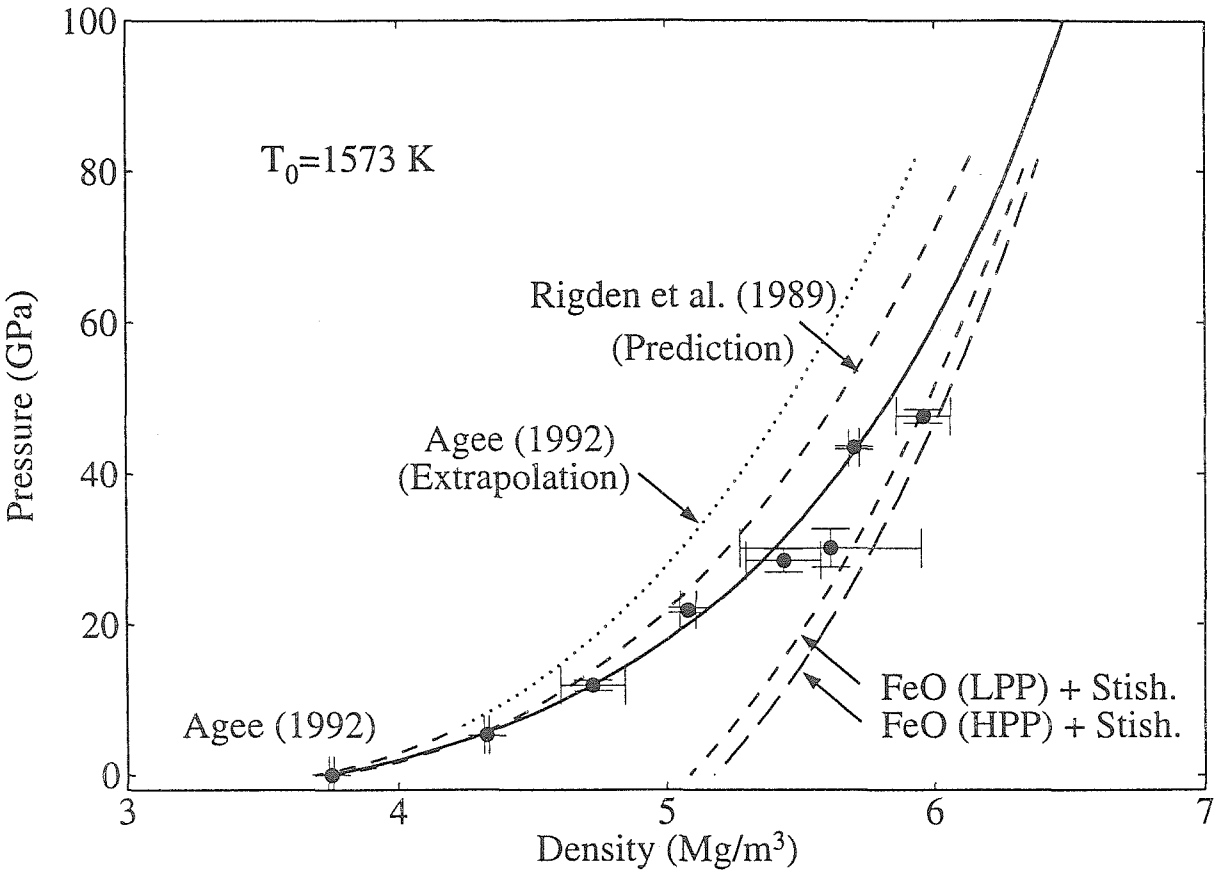

Figure 4.10: Shock-wave compression of fayalite at 1573 K. Fits calculated from the ideal oxide mixture model are shown. Isotherms of fayalitic liquid of *Agee* [1992a] (at 1773 K) and *Rigden et al.* [1989] (at 1673 K) are shown for comparison.

As described in Section 4.3, distortion of the Mo capsule occurred during pre-heating; this contributes to the uncertainties in our measurements of travel times of the shock-wave through the assembly in the experiments on fayalitic liquid. The curvature of the shock arrival (see example in Figure 4.7b), most visible near the edge of the "top hat" (the central rising of the target, see Figure A.2), is due both to the higher shock velocity in the molybdenum side wall than in the sample and to bowing during pre-heating. In a semi-quantitative analysis in which we ignore effects of the lateral release waves, the shock-wave arrives at the center of the free surface of the Mo cover plate at the time (reference time 0 is when the impact occurs):

$$t_1 = x_D/u_S^{Mo} + x_S/u_S^{Fa} + x_C/u_S^{Mo} \tag{4.6}$$

(this is what measured as ΔT in Equation 4.5).

In contrast, the shock-wave arrives at the perimeter of the Mo cover plate (which is thicker than the center) at the time:

$$t_2 = x_D/u_S^{Mo} + (x_S - \Delta x_C)/u_S^{Fa} + (x_C + \Delta x_C)/u_S^{Mo}, \tag{4.7}$$

and the shock-wave arrival on the free surface of the side wall occurs at the time:

$$t_3 = (x_D + x_W)/u_S^{Mo}, \tag{4.8}$$

in the three equations above, x_S, x_C, x_W, Δx_C and Δx_D are defined in Figure 4.7a, the u_S's are shock velocity in Fa and Mo.

The shock arrival delay can be separated into two parts:

$$\Delta t_1 \equiv t_1 - t_2 = \Delta x_C\left(\frac{1}{u_S^{Fa}} - \frac{1}{u_S^{Mo}}\right), \tag{4.9}$$

$$\begin{aligned} \Delta t_2 &\equiv t_1 - t_3 = x_S/u_S^{Fa} + x_C - x_W/u_S^{Mo} \\ &= x_S\left(\frac{1}{u_S^{Fa}} - \frac{1}{u_S^{Mo}}\right), \end{aligned} \tag{4.10}$$

in the last step we used the relation $x_W = x_S + x_C$. For a typical shot # 993,

$\Delta x_C = 0.3$ mm, $u_S^{Mo} = 5.98$ km/s, $u_S^{Fa} = 5.01$ km/s, which yields $\Delta t_1 = 0.01$ μs, $\Delta t_2 = 0.13$ μs. The actual measurement on the streak record shows the central arrival is about 0.07 μs later than the edge. This is less than that calculated because the lateral release delays the arrival to some degree. Thus our analysis shows most of the curvature of the shock arrival results from faster propagation within the molybdenum sidewall. This is quantitively evaluated by the following numerical simulation.

For the molten fayalite experiments, the fayalite liquid was contained in a metallic (molybdenum) capsule during the experiments. However, initially we studied the possibility of using iron containers in the experiments to minimize contamination of the molten Fa. The target geometry raises the question whether the shock-wave remained planar by the time it had propagated to the rear surface. We conducted two-dimensional numerical simulations with a finite element code, DYNA2D [*Whirley and Engelmann*, 1992]. Detailed discussion of the flyer plate and the target are given in Figure 4.11, and the equation of state assumed for all materials are given in the caption. In the simulation shown in Figure 4.11, a tantalum flyer plate impacts the target assembly at 2.0 km/s. The target consists of a fayalite pellet encased in an iron capsule. Pressure contours at several time steps are also shown in Figure 4.11.

At shock arrival on the free surface (about 1.0μs after impact), it can be seen that shock front is flat within a diameter of about 9 mm (or 70% of the top diameter). Therefore, our first target design ensured that the shock-wave that propagates through the sample is one-dimensional. However, we did not study the case where molybdenum was used for the capsule material as in the actual experiments. The iron capsule suffered the problem of excessive deformation from residual gas in capsule. It appears that at 1573 K iron was not mechanically sufficiently strong to resist the very slight gas pressure.

Miller and Puckett [1994] used the Godunov method to calculate the edge effects on shock-wave propagation in Mo-encapsulated molten silicates up to 90 GPa. Their results are compatible with the present results. It is also obvious in the simulation that the shock-wave is supported, *i.e.*, not overtaken by the rarefaction wave from the back of the impactor before it arrives at the free surface.

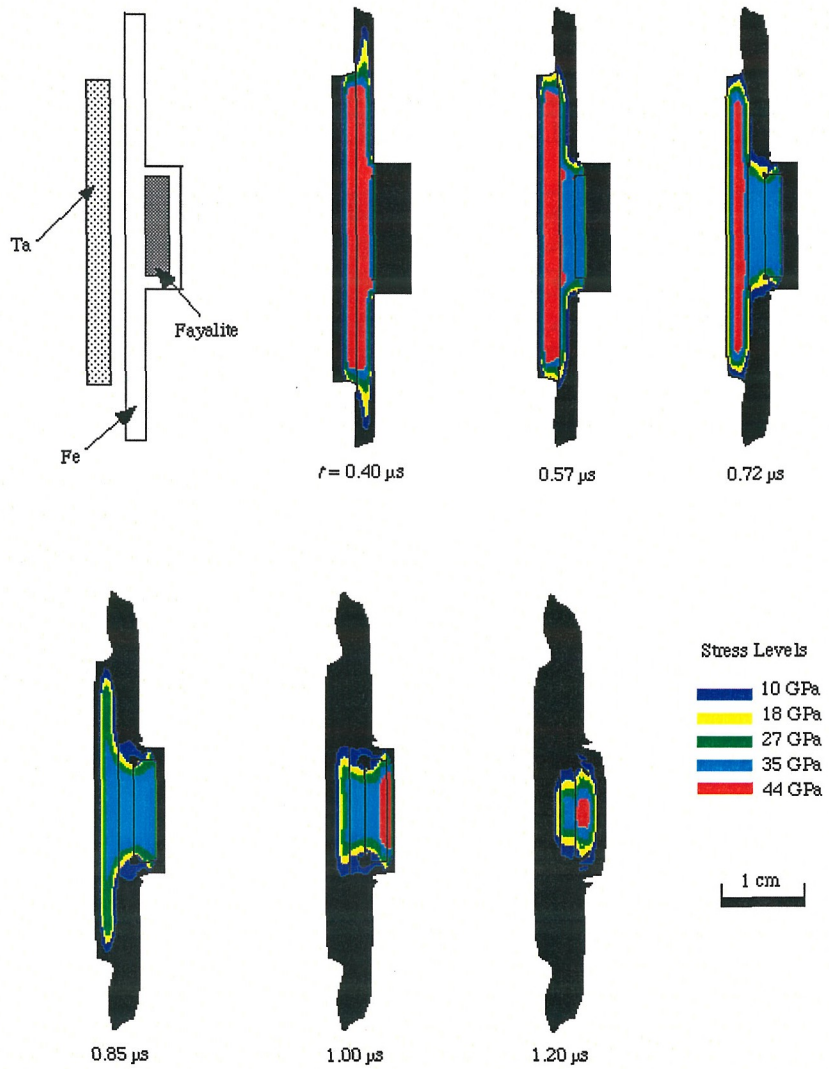

Figure 4.11: DYNA2D simulation of a disc-shaped tantalum flyer plate impacting a cylindrically symmetric fayalite sample placed inside an iron capsule at 2.0 km/s. The assembly is axial symmetric about center line. From left to right, top to bottom: Initial shock wave (44 GPa in Fe) encounters iron-fayalite interface, a reflected shock propagates into the flyer plate; Rarefaction wave propagates back into the iron driver plate, a 35 GPa amplitude shock front advances in fayalite; Shock in the flyer plate reaches its rear surface; Rarefaction wave propagates forward from the rear surface of the flyer plate; Shock wave in fayalite reaches the second fayalite-iron interface and fayalite is re-shocked to 44 GPa, shock wave arrives at the iron free surface; Rarefaction waves propagate inward from outside lateral surfaces of the capsule. Parameters used in the calculation: Ta: ρ_0=16.656 Mg/m^3, c_0=3.43 km/s, s=1.19; Fe: ρ_0=7.174 Mg/m^3, c_0=3.67 km/s, s=1.64; Fa: ρ_0=4.28 Mg/m^3, c_0=4.13 km/s, s=1.42. Grüneisen parameter γ for all three materials was assumed to be 1.0.

Table 4.5: Comparison of equation of state parameters for solid and liquid fayalite.

Phase	T_0 (K)	ρ_0 (Mg/m^3)	K_0 (GPa)	K_0'	Reference
Liquid	1673	3.766	20.5[1]	11.2[1] (1.5)	*Rigden et al.* [1989] (Predicated)
	1773	3.688[2] (0.020)	24.4[1] —[3]	10.1[1] —[3]	*Agee* [1992a] (Experiments)
	1573	3.750[2] (0.018)	25.9[4] (0.4)	5.36[4] (0.04)	This study
Solid (HPP)	300	4.375 (0.027)	72.4[4] (8.0)	4.72[4] (0.24)	This study

1. Isothermal values.
2. *Shiraishi et al.* [1978].
3. For "error bars," see Figure 4.13.
4. Isentropic values.

4.6 Discussion

Using the relations between c_0, s and K_{0S}, K'_{0S} [*Ruoff*, 1967]:

$$K_{0S} = \rho_0 c_0^2, \tag{4.11}$$

$$K'_{0S} = 4s - 1, \tag{4.12}$$

the equations of state of fayalite at T_0=300 K and 1573 K are derived and summarized in Table 4.5. Our zero pressure bulk modulus value agrees with that given by *Agee* [1992a], but its pressure derivative differs significantly. The difference is examined more closely in Figures 4.12 and 4.13 and discussed in Section 4.6.2. The 200 K temperature difference and the difference between the isothermal and isentropic bulk moduli are expected to be small, and both differences, if they have any noticeable effect, should make *Agee* [1992a]'s result even more compressible than ours.

4.6.1 Phase Diagram and Shock Temperature Calculations

Previously, Fe_2SiO_4 fayalite (Fa)'s phase diagram has been reviewed in *Liu and Bassett* [1986] (see Figure 4.14). At high pressure and room temperature, Fe_2SiO_4 olivine

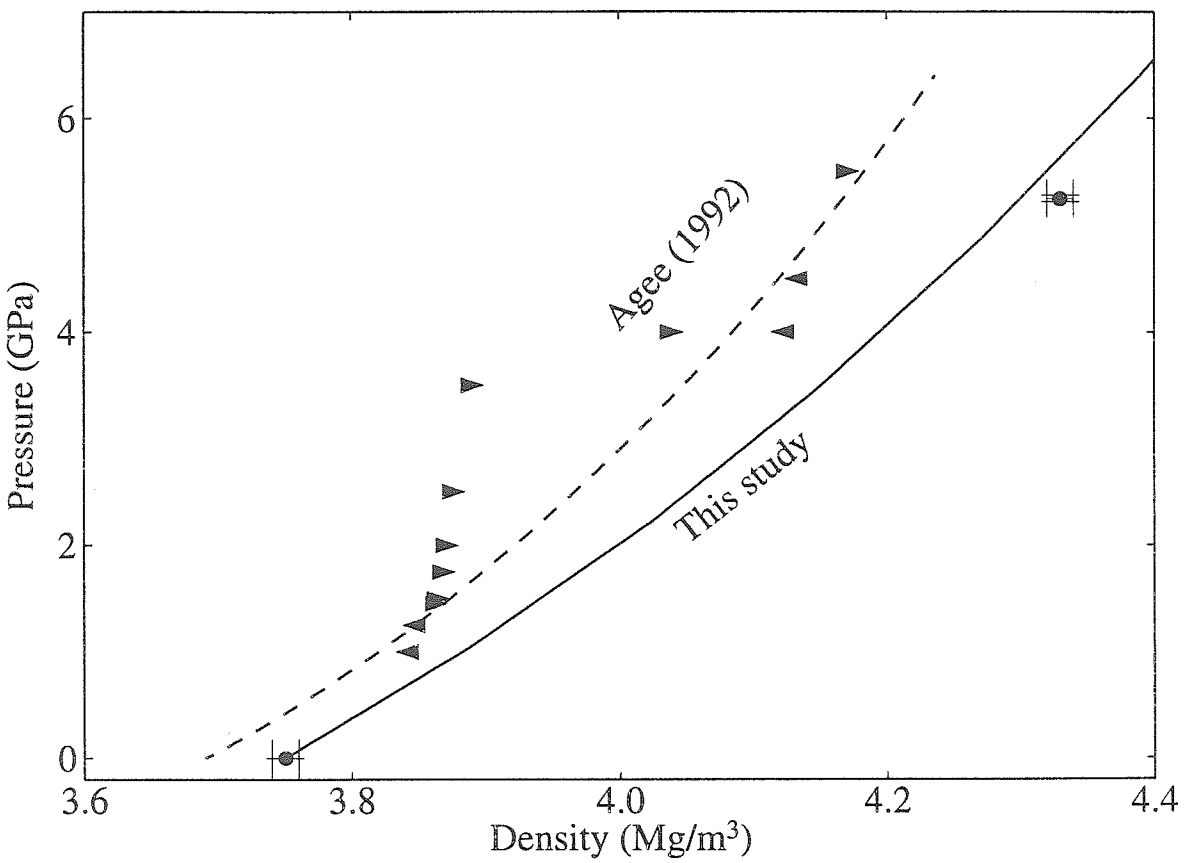

Figure 4.12: Comparison of low pressure compression of *Agee* [1992a] and this study. The arrows are sink-float markers in Agee's results, and density of fayalite is confined to between these markers. Dashed line is the best fit to isothermal compression of liquid fayalite at 1773 K. Circles are from this study. The solid curve is the best fit (same as in Figure 4.10). The difference in initial densities is listed in Table 4.5.

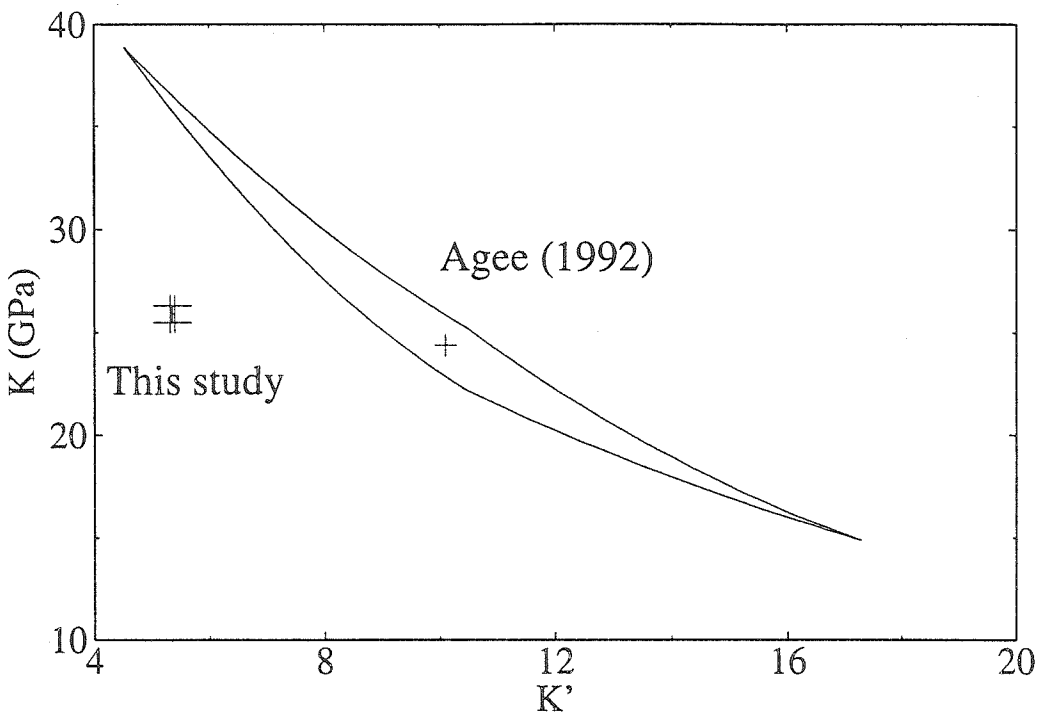

Figure 4.13: Comparison of present data of bulk modulus (K) and its pressure derivative (K') for liquid fayalite. The enclosed area is uncertainty in *Agee* [1992a]'s data.

transforms to the spinel phase at about 4 GPa, then disproportionates into FeO wüstite (Wu) and SiO_2 stishovite (St) at about 18 GPa. The melting point of Fa at 1 bar is 1478 K and increases to about 3200 K at 15 GPa (Figure 4.14). The melting behavior of Fa under high pressures is quite uncertain. Fa melts incongruently from 10^5 Pa (1 bar) and possibly up to 4 GPa [*Lindsley*, 1967; *Hsu*, 1967], *Akimoto et al.* [1967] and *Ohtani* [1979] reported that Fa melts congruently from 5 to 13 GPa. The incongruent melting zone is sketched in Figure 4.14. Calculation of liquid fayalite shock temperature (Appendix C) in Figure 4.14 also indicates that it is possible that Fa pre-heated to 1573 K could be shocked into the solid stability regimes. Crystallization is unlikely on the time scale of our experiments, and molten fayalite is likely to remain in a single (metastable) liquid phase [*Miller et al.*, 1991a]. The shock temperature of solid fayalite is also calculated and plotted in Figure 4.14. It is impossible to infer the shock pressure at which solid fayalite melts along the Hugoniot from our present data base. We infer that fayalite enters the wüstite+stishovite stability regime at about 20 GPa. The parameters used in the shock temperature calculations

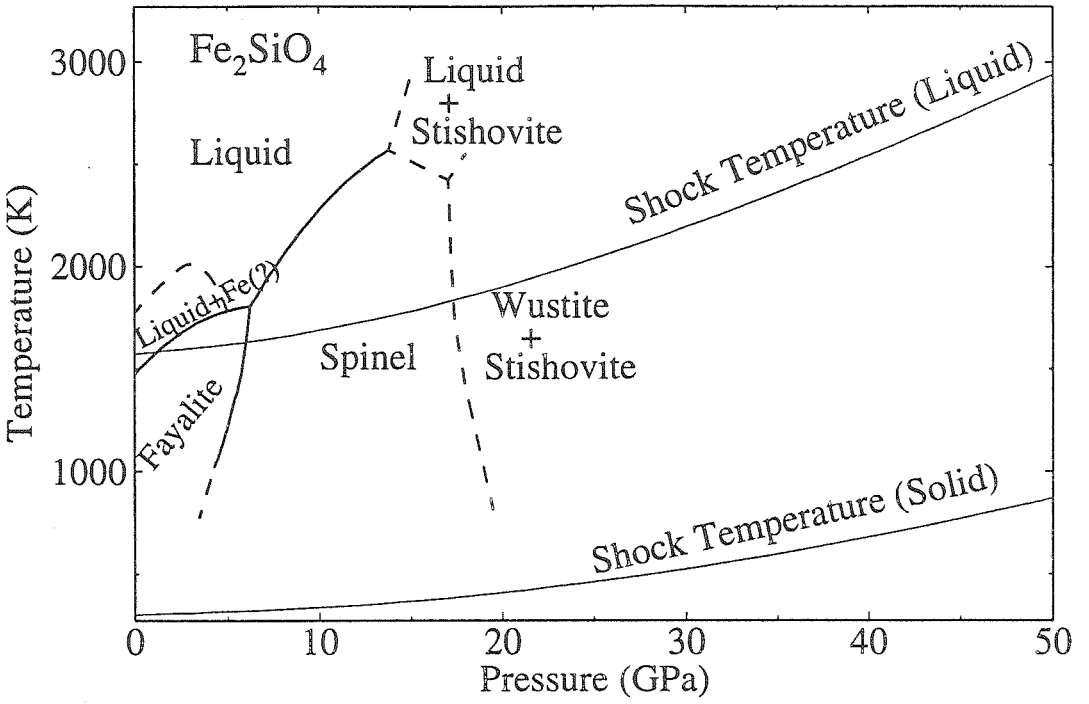

Figure 4.14: *P-T* phase diagram of fayalite [*Liu and Bassett*, 1986]. Curves give calculated shock temperatures for liquid and solid fayalite of Table 4.6.

and the results are listed in Table 4.6.

4.6.2 Fit with Oxide Mixture Models

In order to test the conjecture of *Rigden et al.* [1988] that molten silicates approach the density of an ideal mixture of dense crystalline oxides at above 40 GPa, we used a mixture model of either LPP or HPP wüstite ($Fe_{0.94}O$) [*Jeanloz and Ahrens*, 1980] and stishovite *Lyzenga et al.* [1983]. The LPP wüstite has the B1 (NaCl-type) structure and transforms to B2 (CsCl-type) structure at about 70±10 GPa. The procedure for calculating the mixture volume is as follows:

The dense oxides are first compressed separately along their respective isentropes to a given pressure P. Their volumes decrease to V_S according to the Murnaghan equation of state, and their temperatures rise according to Equation 2.11, to values T_S that may differ from the Hugoniot temperature T_H of the solid or liquid fayalite calculated in Section 4.6.1 at the same pressure. Then, with constant pressure, the temperatures of the oxides are adjusted to the Hugoniot temperature, accompanied

Table 4.6: Shock temperature calculations for solid and liquid fayalite.

Pressure (GPa)	Shock temperatures (K)[1]	
	Liquid Fa (K) $T_0 = 1573$ K, $\gamma_0 = 0.18$[2] K_{0S}=25.9 GPa, $K'_{0S} = 5.36$	Solid Fa (K) $T_0 = 300$ K, γ_0=0.76[3] K_{0S}=72.4 GPa, $K'_{0S} = 4.72$
5	1620	315
10	1688	336
15	1783	366
20	1901	408
25	2038	460
30	2192	523
35	2362	598
40	2543	679
45	2737	771
50	2943	870
55	3155	976

1. In both calculations, $\gamma\rho$=constant, $C_V = 3R$/mol atom and independent of pressure and temperature.

2. Calculated from Equation C.5, $\alpha_0 = 3.0 \times 10^{-5}$ K^{-1}, $C_{P0} = 1.179$ kJ/kg/K [*Touloukian*, 1967], $\rho_0 = 3.750$ Mg/m^3.

3. Calculated from Equation C.5, $\alpha_0 = 3.0 \times 10^{-5}$ K^{-1}, $C_{P0} = 0.652$ kJ/kg/K [*Touloukian*, 1967], $\rho_0 = 4.375$ Mg/m^3.

by thermal expansion. The volumes at (P, T_H) are given by the thermal expansion equation:

$$V_H = V_S \exp(\int_{T_S}^{T_H} \alpha dT), \tag{4.13}$$

where α is the thermal expansion coefficient at high pressure. The oxide volumes are then added linearly, weighed by their respective weight percentage in a fayalite composition, to arrive at the theoretical fayalite volume.

In the calculation, the Grüneisen parameters for HPP FeO and stishovite at STP (γ_0) are calculated from their values of ρ_0, C_{P0}, K_{0S}, and α_0 [*Jeanloz and Ahrens*, 1980; *Lyzenga et al.*, 1983]. Thermal expansion coefficient at high pressure is calculated from γ:

$$\alpha = \frac{\gamma \rho C_P}{K_S}, \tag{4.14}$$

where $K_S = K_{0S} + K'_{0S}P$. The fitting parameters are listed in Table 4.7.

An alternative mixing algorithm often used for solids is the Voigt-Reuss-Hill (VRH) average: The EOS parameters (specific volume $\overline{V_0}$, isentropic bulk modulus $\overline{K_{0S}}$ and its pressure derivative $\overline{K'_{0S}}$) of a stoichiometric mixture comprised of two oxides is [*Watt et al.*, 1976]:

$$\overline{V_0} = xV_0^s + (1-x)V_0^w, \tag{4.15}$$

$$\overline{K_{0S}} = \frac{\overline{K_{0S}^R} + \overline{K_{0S}^V}}{2}, \tag{4.16}$$

$$\overline{K'_{0S}} = \frac{\overline{K_{0S}^{\prime R}} + \overline{K_{0S}^{\prime V}}}{2}, \tag{4.17}$$

where the quantities with superscript R or V are the Reuss or Voigt averages:

$$\overline{K_{0S}^R} = \frac{\overline{V_0}}{\frac{xV_0^s}{K_{0S}^s} + \frac{(1-x)V_0^w}{K_{0S}^w}} \tag{4.18}$$

$$\overline{K_{0S}^V} = \frac{xV_0^s K_{0S}^s + (1-x)V_0^w K_{0S}^w}{\overline{V_0}}, \tag{4.19}$$

$$\overline{K_{0S}^{\prime R}} = \frac{\overline{K_{0S}^R}^2}{\overline{V_0}} \left[\frac{xV_0^s(K_{0S}^{\prime s}+1)}{(K_{0S}^{\prime s})^2} + \frac{(1-x)V_0^s(K_{0S}^{\prime s}+1)}{(K_{0S}^{\prime s})^2} \right] - 1, \tag{4.20}$$

$$\overline{K'_{0S}V} = \frac{xV_0^s K'^s_{0S} + (1-x)V_0^w K'^w_{0S}}{\overline{V_0}}, \tag{4.21}$$

the superscripts s and w denote the quantities for stishovite and wüstite. x=0.29 is the mass portion of SiO_2 in fayalite stoichiometry. The parameters are listed in Table 4.7. The fitting procedure is as follows:

1. We first calculate the parameters of the mixture using Equations 4.15–4.21, then at any given compression $\eta = \rho_0/\rho$, the isentropic pressure P_S is given by the third-order Birch-Murnaghan equation [*Poirier*, 1991]:

$$P_S = \frac{3}{2}K_{0S}[1 - \frac{3}{4}(4 - K'_{0S})(\eta^{-2/3} - 1)](\eta^{-2/3} - 1)[1 + (\eta^{-2/3} - 1)]^{5/2}. \tag{4.22}$$

2. Total work done in isentropic compression is:

$$E_S = -\int_1^{\rho_0/\rho} \frac{P_S}{\rho_0} d\eta. \tag{4.23}$$

3. Total internal energy increase by Hugoniot compression to pressure P and density ρ is:

$$E = \frac{1}{2}P\left(\frac{1}{\rho_{00}} - \frac{1}{\rho}\right) = \frac{P(1+p-\eta)}{2\rho_0}, \tag{4.24}$$

where ρ_{00} is the zero pressure density of fayalite, and $p = \rho_0/\rho_{00} - 1$ is the "porosity" of the oxide mixture.

4. By the Grüneisen equation,

$$E - E_S - E_{TR} = \frac{(P - P_S)}{\gamma\rho}, \tag{4.25}$$

and solving for P gives

$$P = \frac{2\left[\rho_0(E_S + E_{TR}) - \frac{\eta P_S}{\gamma}\right]}{1 + p - \left(1 + \frac{2}{\gamma}\right)\eta}. \tag{4.26}$$

Table 4.7: Equation of state parameters of oxides for mixture models.

	Stishovite[1]	HPP FeO[2]	LPP FeO[2]	VRH Mixture[3]
ρ_0 (Mg/m^3)	4.29	6.05	5.864	5.41
K_{0S} (GPa)	316	195	185	230
K'_{0S}	5.3	3.5	3.2	4.11
γ_0	1.38	1.8	1.63	1.6
E_{TR} (MJ/kg)	0.82	0.4	0	0.5[4]

For all phases, $\gamma\rho$ is assumed constant and $C_V = 3R$/mol atom.

1. *Lyzenga et al.* [1983].
2. *Jeanloz and Ahrens* [1980].
3. Mixture of HPP FeO and stishovite.
4. Mass weighed average.

In Figure 4.9, two fits using the ideal mixing model and the VRH model are shown. The results are very close, and above ~50 GPa, all three models fit within 3% of the compression curve of single crystal fayalite from room temperature. This supports our proposal in Section 4.5.1 that fayalite breaks down to wüstite and stishovite over the 35–55 GPa interval.

Two fits to the fayalitic liquid Hugoniot are obtained by the ideal mixing model using stishovite and either LPP or HPP wüstite as the oxide components. They are shown in Figure 4.10. Both mixing models are within 5% of the Hugoniot at pressures greater than ~ 40 GPa. This supports the hypothesis of *Rigden et al.* [1989] that coordination of Si^{4+} molten fayalite changes from tetrahedral to octahedral over a pressure range of about 40 GPa, and above 40 GPa, specific volume of fayalitic liquid can be predicted using the linear sum of the partial molar volumes of dense-packed oxide crystals (FeO and SiO_2 (stishovite)). The apparent difference in K'_0 (either isothermal or isentropic) between *Rigden et al.* [1989]'s predication and our experimental result (Table 4.5) is due to the following reasons:

1. The zero pressure density cited in [*Rigden et al.*, 1989] is higher than those used in either *Agee* [1992a] and this work (Table 4.5).

2. *Rigden et al.* [1989] assumed K_{0T}=20.5 GPa for fayalitic liquid at 1673 K and

1 bar, calculated from *Rivers* [1985] and *Rivers and Carmichael* [1987]'s result of K_{0S}=21.4 GPa. Results from work by *Agee* [1992a] and this work indicate K_0 is higher (24.4 or 25.9 GPa, Table 4.5) than that measured by *Rivers and Carmichael* [1987]. If the new values are correct, a K_0' in the 10–11 range as predicted by *Rigden et al.* [1989] and measured by *Agee* [1992a] would actually make density of fayalitic liquid less than 90% of that given by the ideal mixing model (Figure 4.10) and consequently put the premise of the predication in question.

3. *Rigden et al.* [1989] calculated K_{0T}' by requiring that the density of fayalitic liquid equals to 90% of that given by the ideal mixing model (which used the LPP equation of state for the FeO end member). Our experimental data show that the actual fit is better than the 90% assumed – fayalitic liquid density is 96.5% of the model density with the LPP EOS, and 95.4% of the model density with the HPP EOS.

4.6.3 Application to the Earth's Mantle

Our present work complements previous work by *Rigden et al.* [1988] on eutectic anorthite-diopside by providing the compressional properties of the iron end-member. We are now able to simulate the natural basalt composition with $(An_{0.36}Di_{0.64})_{0.85}Fa_{0.15}$ (Table 4.8).

The compressibility of our model basalt is calculated using the same method described by Equations 4.15–4.17. The resulting EOS parameters are: $\rho_0 = 2.719$ Mg/m^3, K_{0S}=24.4 GPa, and K_{0S}'=4.87. The addition of the ferrous iron end member causes a noticeable stiffening of the compression curve (Figure 4.15). As a result, the neutral buoyancy zone in the host (PREM [*Dziewonski and Anderson*, 1981]) mantle is at about 250–400 km depth (9–14 GPa in pressure) rather than 180–300 km depth proposed by *Rigden et al.* [1984].

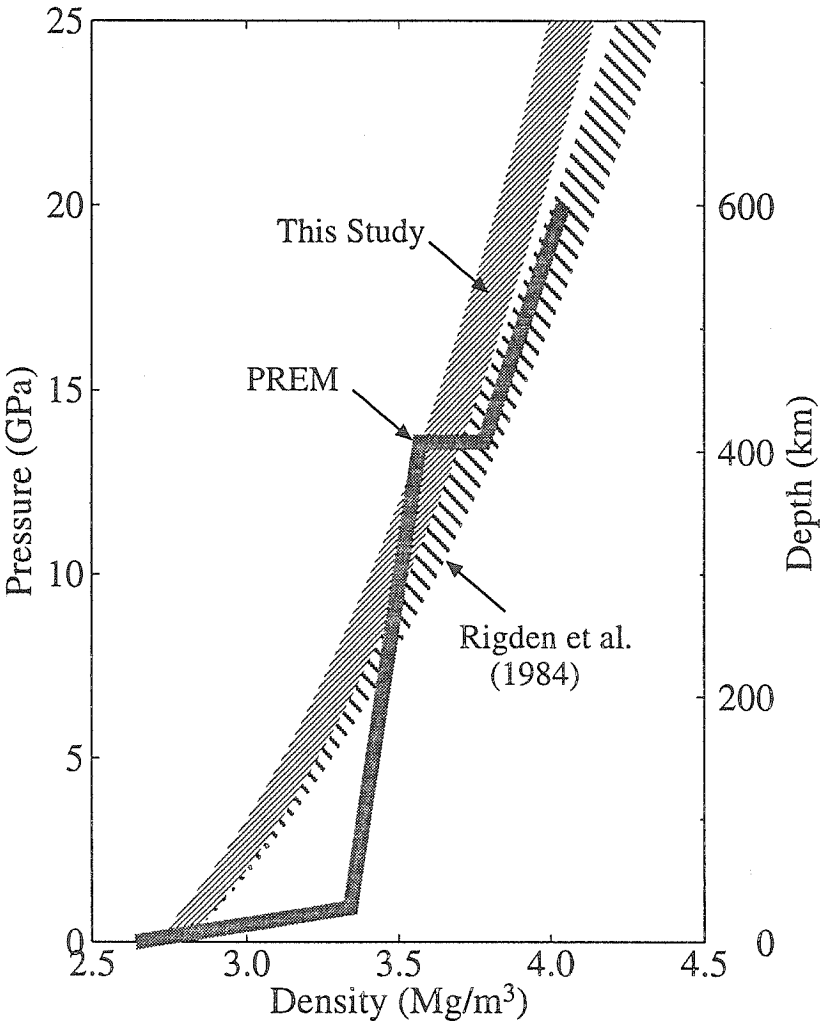

Figure 4.15: Density of model basalt ($(An_{0.36}Di_{0.64})_{0.85}Fa_{0.15}$, solid curve) compared with that of Earth's mantle [*Dziewonski and Anderson*, 1981]. The *Rigden et al.* [1984] curve is based on the compression of anorthosite-diopside eutectic composition but corrected for the density increase caused by the FeO end member. Our model is based on the values of K_{0S} and K'_{0S} of $(An_{0.36}Di_{0.64})_{0.85}Fa_{0.15}$. Uncertainties represented by the widths of the bands for both models are due to density variations of basalts (ρ_0 from 2.7 Mg/m^3 for mid-ocean ridge basalt to 2.8 Mg/m^3 for komatiite). The addition of the fayalite end member noticeably decreases the compressibility of the silicate liquid.

Table 4.8: Model and natural basalt compositions.

	$(An_{0.36}Di_{0.64})_{0.85}Fa_{0.15}$ wt%	Average MAR Basalt[1] wt%
SiO_2	47.61	49.21
TiO_2		1.39
Al_2O_3	13.37	15.81
FeO	9.23	9.18
MnO		0.16
MgO	9.38	8.53
CaO	20.41	11.14
Na_2O		2.71
K_2O		0.26
P_2O_5		0.15
Total	100.00	100.54

1. Average Mid-Atlantic Ridge basalt [*Melson and Thompson*, 1971].

4.7 Conclusions

1. Based on our shock-wave experiments on single crystalline fayalite at an initial temperature of 300 K and on fayalitic liquid at an initial temperature of 1573 K, we obtained the following equations of state for the two phases:

   The u_S-u_P relation in the high pressure regime (> 60 GPa) for fayalite shocked from room temperature can be fit with a linear function:

$$\rho_0 = 4.375(0.027)\ \mathrm{Mg/m^3}, \tag{4.27}$$

$$u_S = 4.07(0.22)\ \mathrm{km/s} + 1.43(0.06)\ u_P. \tag{4.28}$$

   This yields the isentropic bulk modulus $K_{0S} = 72.4 \pm 8.0$ GPa, and its pressure derivative K'_{0S}=4.72±0.24.

   The Hugoniot relation for liquid fayalite initially at 1573 K is:

$$\rho_0 = 3.750(0.018)\ \mathrm{Mg/m^3}, \tag{4.29}$$

$$u_S = 2.63(0.02)\ \text{km/s} + 1.59(0.01)\ u_P \qquad (4.30)$$

and $K_{0S} = 25.9 \pm 0.4$ GPa, $K'_{0S} = 5.36 \pm 0.04$.

2. The solid fayalite data at above 50 GPa can be fit with models of oxide mixture using stishovite and either LPP or HPP wüstite. We suggest fayalite breaks down to the oxides between 40–50 GPa.

3. The fayalitic liquid data at above 40 GPa can be fit with ideal mixing of partial molar volumes of stishovite and FeO (LPP or HPP), in support of the gradual Si^{4+} coordination change (from tetrahedral at 1 bar to octahedral at about 40 GPa) model [*Rigden et al.*, 1989]. The bulk modulus compares favorably with *Agee* [1992a]'s result (24.4 GPa) and is higher than that measured by *Rivers and Carmichael* [1987], but the pressure derivative is quite different (10.1 from *Agee* [1992a]). The compression curve given by *Agee* [1992a] is incompatible with the ideal mixing model. Based on this study, we suggest K'_0 is not a sensitive function of composition as suggested by *Rigden et al.* [1989].

   The linear u_S-u_P relation (r^2=0.98) indicates absence of abrupt structural change in the fayalite liquid, in agreement with the Stolper-Ahrens-Rigden model for silicate liquid compression [*Stolper and Ahrens*, 1987].

4. Our study supports the use of the ideal mixing model for the high pressure density of the iron end member in basic to ultrabasic magmas, *e.g.*, komatiite [*Miller et al.*, 1991a]. Therefore, our result agrees with the suggestion that olivine crystals become neutrally buoyant at about 8 GPa [*Stolper et al.*, 1981; *Miller et al.*, 1991a; *Agee and Walker*, 1993], contrary to *Herzberg* [1987b]'s conclusion.

5. A model basalt incorporating our liquid fayalite data shows the neutral buoyancy zone of basic silicate melts is at about 250–400 km depth.

Appendix A Design of the RF Heating Coil

The heating coil is an important part in preheated shock-wave experiments. Heating uniformity at high temperature is more critical in the present preheated iron EOS and VISAR experiments than previous studies [*Rigden et al.*, 1988; *Miller et al.*, 1991a; *Rowan*, 1993] because it is necessary to heat solid targets to as close to its melting point as possible to lower the shock pressure needed to achieve melting under shock conditions.

A.1 Maxwell Equations

We employ the Maxwell equations to develop a simple model for optimizing the radio-frequency induction in the target.

$$\mathrm{div}\mathbf{D} = \rho, \tag{A.1}$$

$$\mathrm{div}\mathbf{B} = 0, \tag{A.2}$$

$$\mathrm{curl}\mathbf{E} = -\frac{\partial \mathbf{B}}{\partial t}, \tag{A.3}$$

$$\mathrm{curl}\mathbf{H} = \mathbf{J} + \frac{\partial \mathbf{D}}{\partial t}, \tag{A.4}$$

where $\mathbf{B}$ and $\mathbf{E}$ are electric and magnetic fields, $\mathbf{H} = \mathbf{B}/\mu$ is the magnetic intensity, and μ is the magnetic permeability; $\mathbf{D} = \epsilon\mathbf{E}$ is the electric displacement, ϵ is the electric permittivity, ρ is electric charge density, and $\mathbf{J}$ is electric current density. For vacuum, $\epsilon_0 = 8.85 \times 10^{-12}$ farad/m and $\mu_0 = 4\pi \times 10^{-7}$ henry/m.

The Equation A.3 dictates that inside any medium, when there is an alternating magnetic field, an electric field is induced. If the medium is a conductor, an eddy

current:

$$\mathbf{J} = \beta \mathbf{E}, \tag{A.5}$$

where β is the conductivity, will be present. This current in turn heats up the conductor. The heat per unit volume generated by the current is:

$$q = J^2/\beta. \tag{A.6}$$

This is the basis of induction heating of metals. For a sinusoidally oscillating B field, $q \propto J^2 \propto E \propto B$.

In our pre-heated experiments, the (external) alternating magnetic field is generated by the heating coil according to the Biot-Savart law (see, e.g., *Slater and Frank* [1969]):

$$\mathbf{B} = \frac{\mu_0}{4\pi} \frac{I \mathbf{ds} \times \mathbf{r}}{r^3}, \tag{A.7}$$

where $\mathbf{r}$ is the location of interest from a length $\mathbf{ds}$ of wire carrying a current I.

This field is coupled to the inside of the metal as required by Equation A.2 and A.4. For the B component normal to the metal surface, Equation A.2 dictates that $B_\perp$ is continuous across the metal surface; for the parallel component $B_\parallel$, Equation A.4 requires $H_\parallel = B_\parallel/\mu$ is continuous (for air, $\mu = \mu_0$). Therefore, by evaluating the external magnetic field distribution at the metal surface, we can estimate the temperature field in the target, which we will do in the following section. However, we do not make an attempt to estimate the coupling efficiency of the coil and the target as this is a complex problem, and the coupling attained in our experiments is quite adequate.

A.2 Coil Design

It was found that the original coil design [*Rigden et al.*, 1988; *Miller et al.*, 1991a] (using 6 mm (1/4 inch) O.D. copper tubing, coil I.D. ~50 mm) was not suitable for

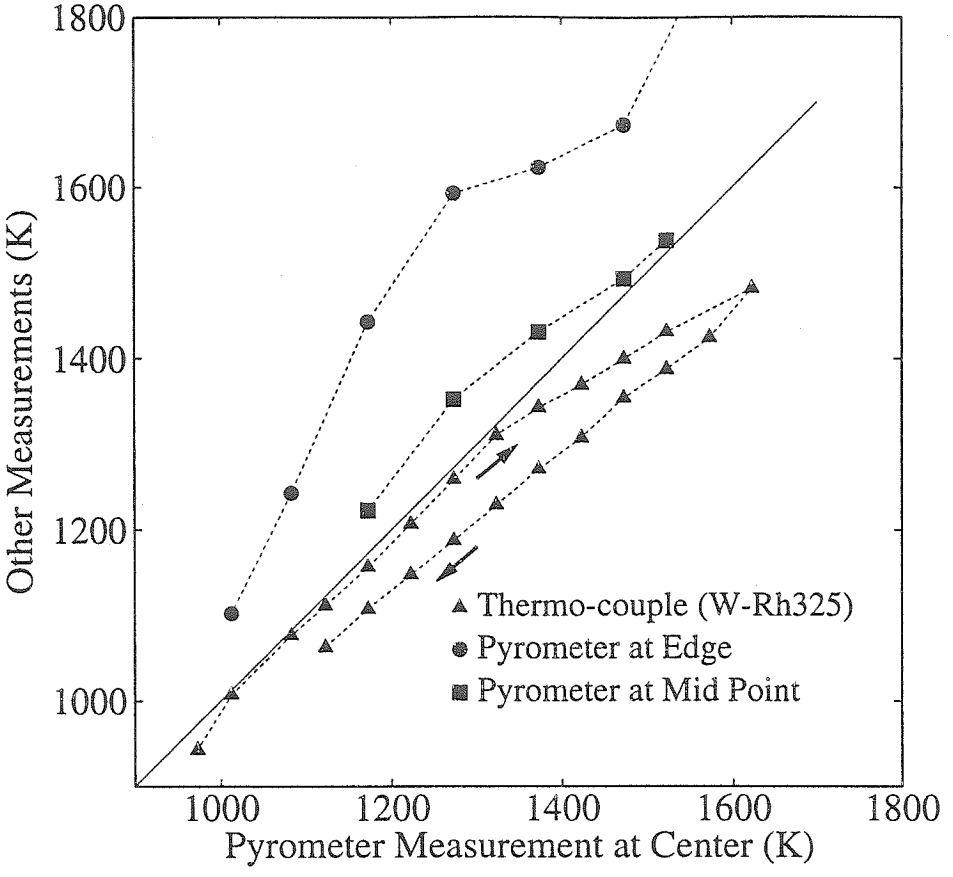

Figure A.1: Temperature distribution in an iron target heated with the 50 mm-I.D. coil. Temperature measured at target center using a Williamson 8120S-C-WD2 pyrometer (45° line) is a reference to temperatures measured by other means. Temperature gradient is shown as the deviation of the temperatures at the edge and mid-point on the driver plate from the central temperature. The target edge is molten (melting point of iron is 1811 K) when central temperature reaches ~1500 K. Measurement made with thermocouple is also shown. The arrows indicate heating history. The thermocouple well is on the driver plate, about 1 mm from the top hat (Figure A.2).

the iron experiments (Figure A.1).

To improve the heating of the target, the coil was redesigned. Unfortunately, since the geometry of the coil is complicated, only a detailed numerical solution can predict the electromagnetic field on the target surface, the generation of heat, its conduction and radiation away from the heated zone. However, we used a few simple formulae from electromagnetic theory to understand how the coil geometry affects target heating.

1. The magnetic field on the axis of the coil, approximated by a single circular

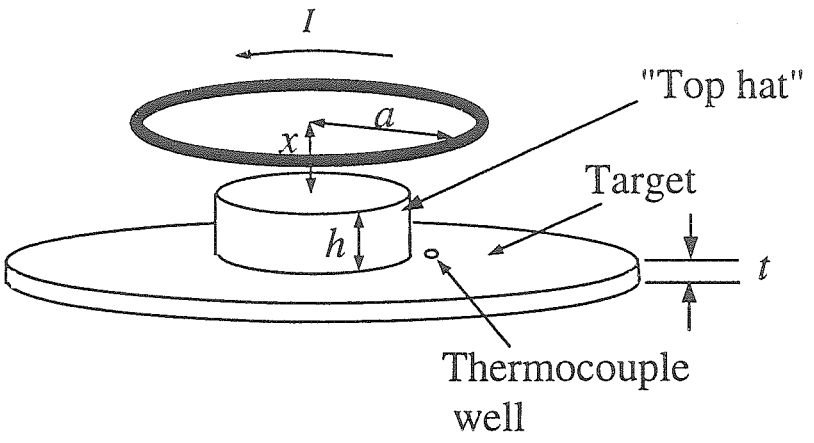

Figure A.2: Simplication of the induction current to a circular current flow I. $h \sim 4$ mm and $t \sim 2$ mm for present targets. a and x are to be determined. The thermocouple well is a ~ 1 mm diameter hole drilled ~ 1 mm deep.

current flow (Figure A.2), is given by the Biot-Savart law [*Slater and Frank*, 1969]:

$$B_{\text{center}} = \frac{\mu_0 I a^2}{2(a^2 + x^2)^{3/2}}. \tag{A.8}$$

The equation above applies to a constant current flow, or an alternating current of amplitude I, in which case B_{center} is also the amplitude of the alternating field. The latter interpretation is applicable to our problem.

2. For estimating B off center, we approximate magnetic field inducted by the coil to that by an infinite straight line current (Figure A.3). Since the coil is close to the target surface (coil-target distance $h + x \ll 2a$), we expect this approximation to be valid [*Slater and Frank*, 1969]:

$$B_{\text{edge}} = \frac{\mu_0 I}{2\pi(x + h)}. \tag{A.9}$$

B_{edge} is defined as amplitude of the alternating field.

We need to calculate a few cases using Equations A.8 and A.9 to increase the factor

$$f = B_{\text{center}}/B_{\text{edge}}. \tag{A.10}$$

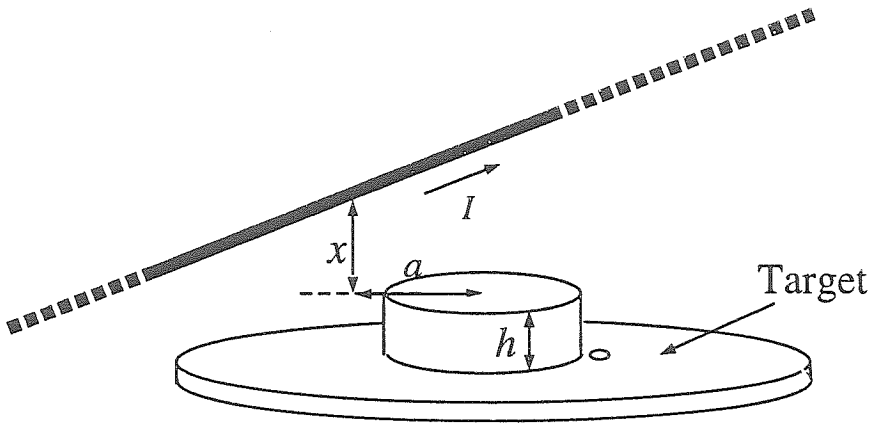

Figure A.3: Approximation of the effect of the coil at off-center positions to that of an infinite straight line current I parallel to the driver plate. Dimensions a and x are to be determined.

1. We first calculate the fields for the previous coil design. Although f >1 at x > 4.2 mm (Figure A.4), the experiments show the center of the target is under-powered. This is probably because the multiple coil windings (for the purpose of boosting heating at any given power setting) strengthen B_{edge} more than B_{center}. Notice f does not reach its maximum even when x=10 mm, where coupling between the coil and the target is unacceptably low. We need to find a solution to increase f.

2. The obvious solution is to decrease a. Calculation for a=12.5 mm is shown in Figure A.4. f reaches its maximum at x about 6 mm.

The new coil design necessitates the use of 3 mm (1/8 inch) O.D. tubing. We used a template with two Plexiglas discs and a center rod (Figure A.2) to control the coil I.D., and 3M heat shrink tubing to wrap tightly around the copper tubing to control the winding spacing. A coil, constructed in this way, and assembled with an iron target, is shown in Figure A.5. With the new coil, the temperature difference over the entire target is usually less than 30 K at 1573 K (Figure A.7). The new design also improved power coupling between the target and the coil.

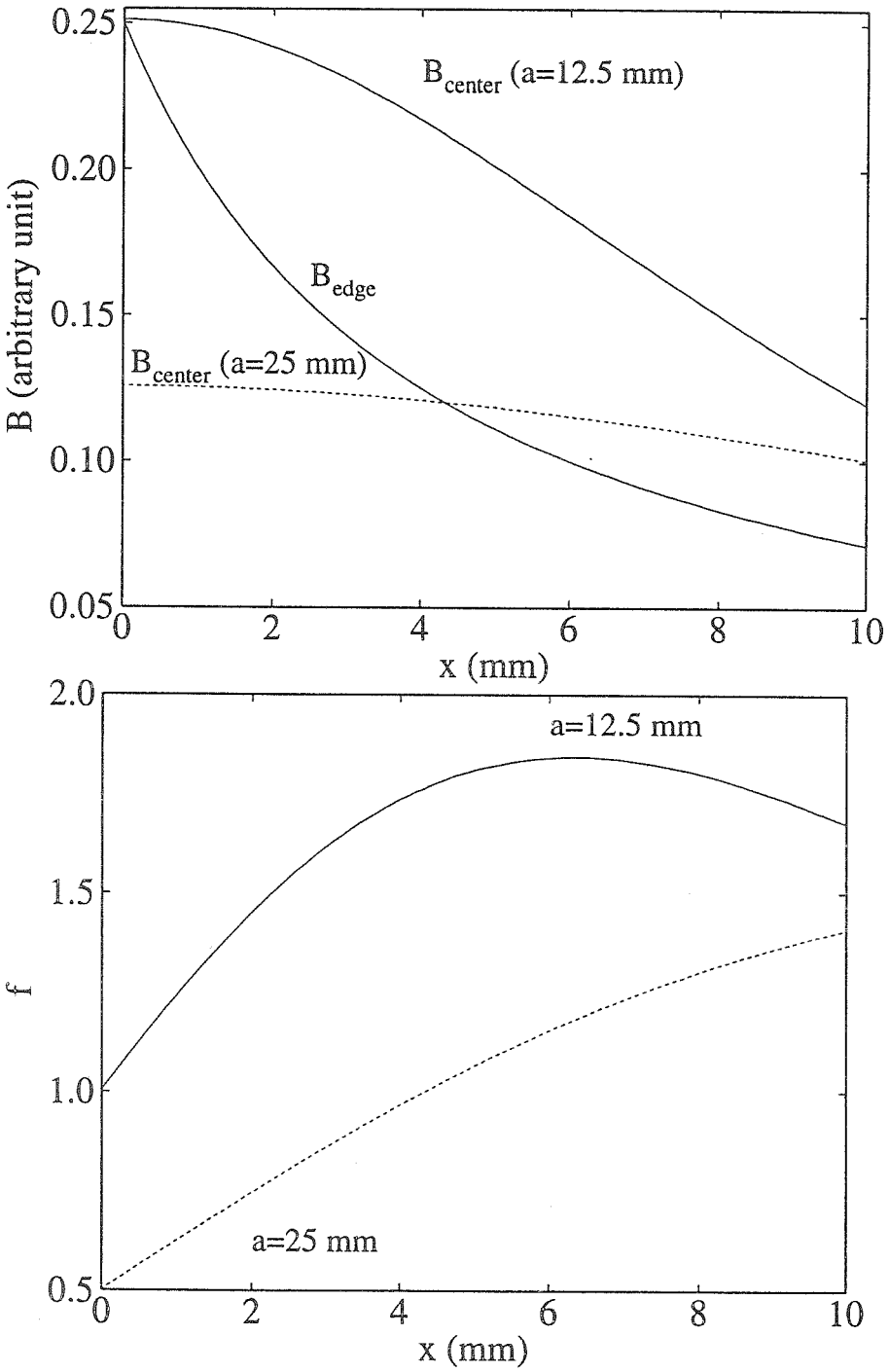

Figure A.4: Calculation of magnetic fields and the factor f for $a = 25$ mm (previous coil design) and $a = 12.5$ mm (new coil design). The edge field strengths in the two cases are identical, but the smaller coil significantly boosts central field strength.

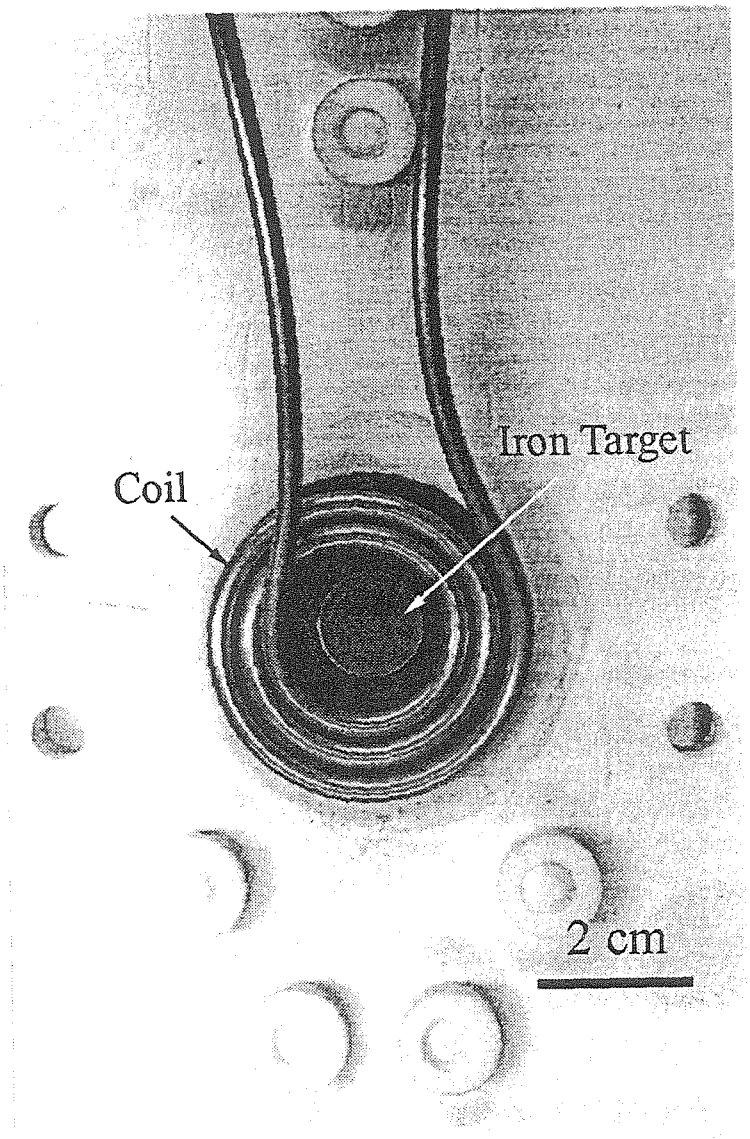

Figure A.5: The heating coil used in the preheated iron and liquid fayalite experiments.

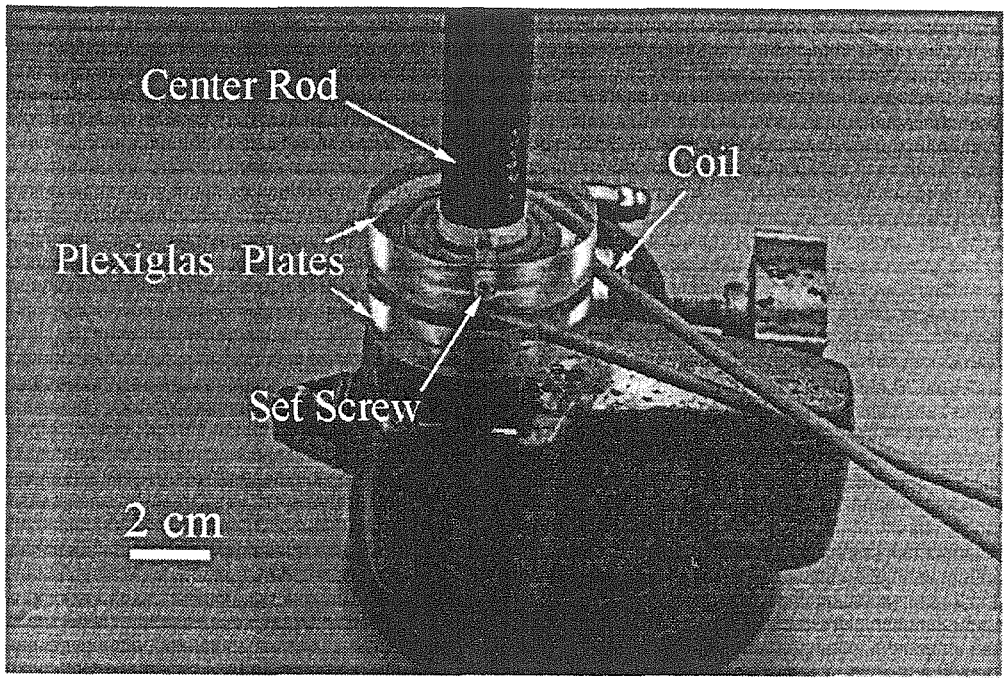

Figure A.6: Photo of the template used to make the heating coil.

A.3 Temperature Heterogeneity

The temperature gradient across the lateral surface of the target is measured experimentally as described Section A.2. However, there is also a gradient along the thickness of the target, due the the limited skin depth of the metal that the electromagnetic field can penetrate [*Slater and Frank*, 1969]:

$$\delta = \sqrt{\frac{2}{\omega\beta\mu}}, \tag{A.11}$$

where ω is the circular frequency of the oscillating field.

For an order-of-magnitude estimate, $\beta = 1.8\times10^{6}\ \Omega^{-1}\mathrm{m}^{-1}$ for iron at 800 K (values at higher temperatures are not available) [*Lide*, 1993–1994, p. 12-33]. Assuming $\mu = \mu_0$, the penetration depth is 1.0 mm at 450 kHz frequency of the RF heater. Thus, δ is much less than the target thickness used ($h + t \approx 6$ mm).

We make a simple model to estimate the effect of the penetration depth: On the unheated side of the target, the rate of energy loss by thermal radiation per unit area

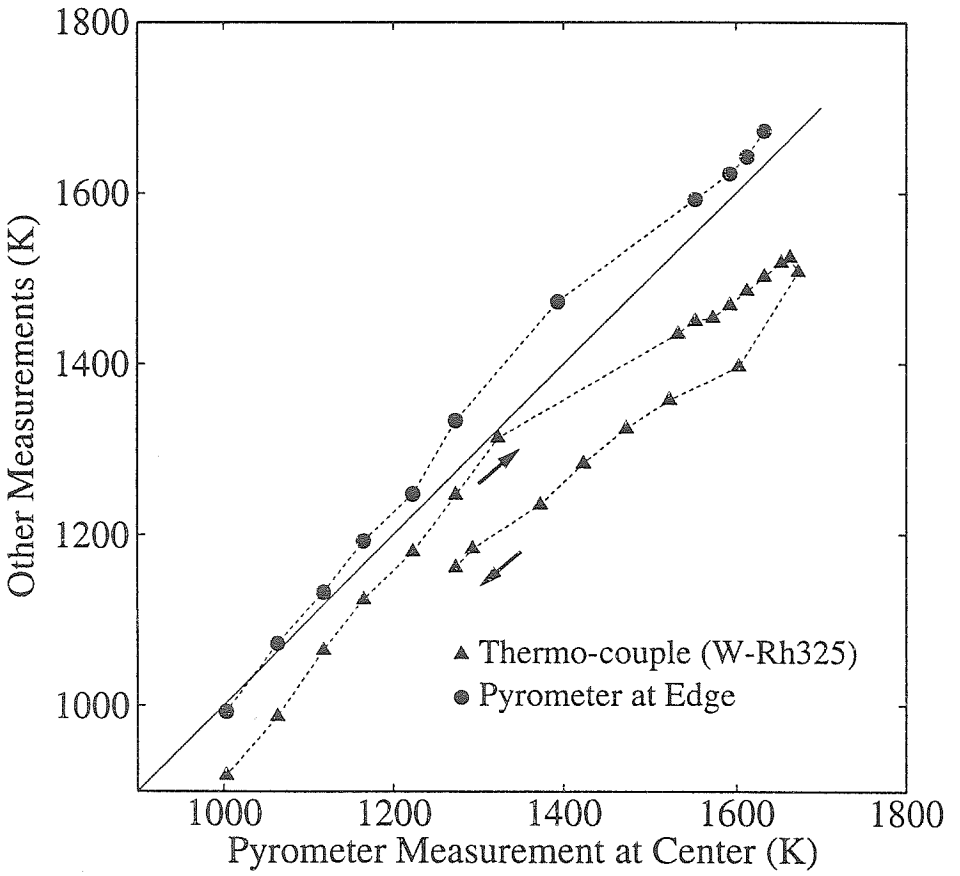

Figure A.7: Temperature distribution in an iron target heated with a 12.5 mm-radius coil. Temperature measured at target center using the pyrometer is the reference for temperatures measured by other means. Arrows indicate heating history.

of target surface is given by:

$$E_1 = \sigma T^4, \tag{A.12}$$

where $\sigma = 5.671 \times 10^{-8}$ W m^{-2}K^{-4} is the Stefan-Boltzmann constant. Assuming a temperature difference ΔT exists in the layer of iron between the penetration depth and the unheated surface (of thickness $h + t - \delta$), the rate of heat flow per unit area across the boundary at the penetration depth is:

$$E_2 = \frac{\gamma \Delta T}{h + t - \delta}, \tag{A.13}$$

where γ is iron's thermal conductivity. At equilibrium, $E_1 = E_2$ yields

$$\Delta T = \frac{\sigma T^4 (h + t - \delta)}{\gamma}. \tag{A.14}$$

For Fe, γ=32.8 W m^{-1}K^{-1} at 1573 K [*Lide*, 1993–1994, p. 12-137]. We calculate ΔT=52 K. For the Mo capsules used in the liquid fayalite experiments, the temperature difference should be less ($\approx$ 20 K) because convection within the fayalite liquid greatly reduces the temperature difference.

Appendix B Equation of State Experiment Data Reduction

This chapter is based on *Ahrens* [1987].

When a plate of material 1 (density ρ_{01}) impacts normally on another plate of material 2 (density ρ_{02}) at velocity v_f, shocks are driven into both media. In the frame of reference of the material at rest, the shock velocities are given by:

$$u_{Si} = c_{0i} + s_i u_{Pi}, \tag{B.1}$$

where u_{pi} is the associated particle velocity, c_{0i} and s_i are material properties, the second subscript $i = 1, 2$ denotes material number, the following boundary conditions must be satisfied (Figure B.1):

$$v_f - u_{P1} = u_{P2}, \tag{B.2}$$

$$P_1 = P_2, \tag{B.3}$$

where the shock pressure, P_i, is given by the momentum Rankine-Hugoniot equation:

$$P_i = \rho_{0i} u_{Si} u_{Pi}. \tag{B.4}$$

From mass conservation, the Hugoniot densities (behind the shock) are given by:

$$\rho_i = \frac{\rho_{0i}}{1 - u_{Pi}/u_{Si}}. \tag{B.5}$$

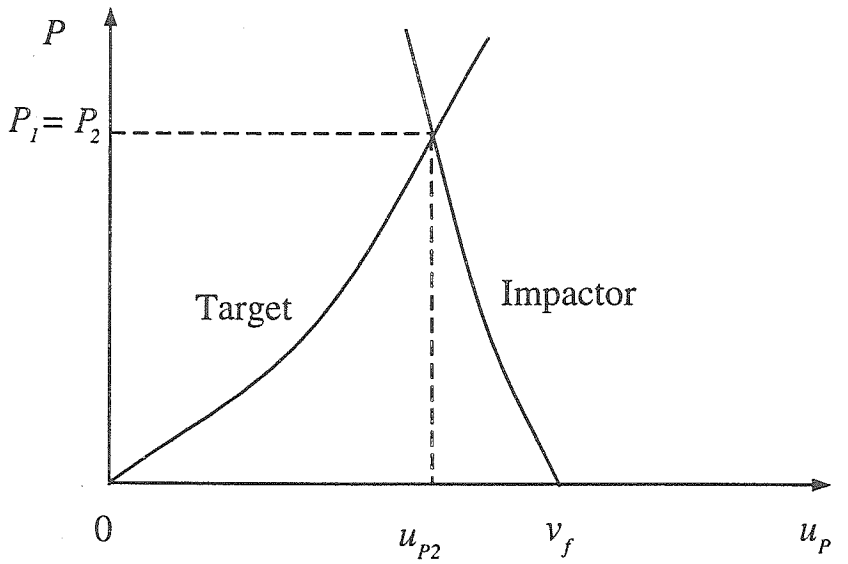

Figure B.1: Impedance match solution between an impactor and a target. Pressure and particle velocity must be continuous across the boundary.

B.1 Hugoniot State

There are two situations for which we need to find solutions. They are discussed in the following.

B.1.1 Target Hugoniot Known

This is the case when the flyer plate impacts a standard driver plate, whose properties ρ_{0i}, c_{0i} and s_i are known. It is also used in our high temperature fayalite experiments during each iteration step to calculate the time of shock propagation through the sample and Mo cap. By solving Equations B.1 to B.4, the particle velocity of the flyer plate is:

$$u_P = (-b - \sqrt{b^2 - 4ac})/2a, \tag{B.6}$$

where

$$a = s_1\rho_{01} - s_2\rho_{02} \tag{B.7}$$

$$b = -c_{01}\rho_{01} - 2s_{01}\rho_{01}v_f - c_{02}\rho_{02} \tag{B.8}$$

$$c = v_f(c_{01}\rho_{01} + s_{01}\rho_{01}v_f). \tag{B.9}$$

The other parameters (u_{Pi}, u_{Si} and P_i) can be easily obtained from Equations B.1 to B.4.

B.1.2 Target Hugoniot Unknown

This is the situation where the driver plate impacts the sample with known ρ_{02}, but unknown c_{02} and s_2. u_{S2} is measured from a streak camera record that measures the time interval required for the shock to propagate through a known thickness of sample. We need to calculate u_{P2} to derive the u_{S2}-u_{P2} relation. This is done by collection of experimental data from a series of shots that drive the sample to a range of pressures.

Solve for u_{P2} in Equations B.1 to B.4 (without invoking Equation B.1 for the sample, and express P_2 in terms of u_{P2} via Equation B.4), we obtain:

$$u_{P2} = v_f + a - \sqrt{a^2 + \rho_{02} u_{S2} v_f / (\rho_{01} s_1)}, \tag{B.10}$$

where

$$a = (c_{01} + u_{S2}\rho_{02}/\rho_{01})/(2s_1). \tag{B.11}$$

Again, the other parameters (u_{Pi}, u_{Si} and P_i) are easily derived.

B.1.3 Remark

In both of the two cases above, if the effective impactor ("Impactor" in Figure B.2) is pre-shocked to a known state 1 with particle velocity u_{P1}, as for example occurs when the driver plate drives a shock into the sample ("Target 1" or "Target 2"), the same algorithm can be used by treating the impactor as unshocked, but with an initial velocity of $2u_{P1}$. We approximate the release adiabat of the driver plate by reflecting its Hugoniot in the u_p-P plane horizontally about the initial shock state. Because the second shock or the partial release (depending on the target impedance) follow closely with the reflected Hugoniot, the points 2 and 3 shown in the figure are the impedance match solutions. Compared with Figure B.1, the construction of

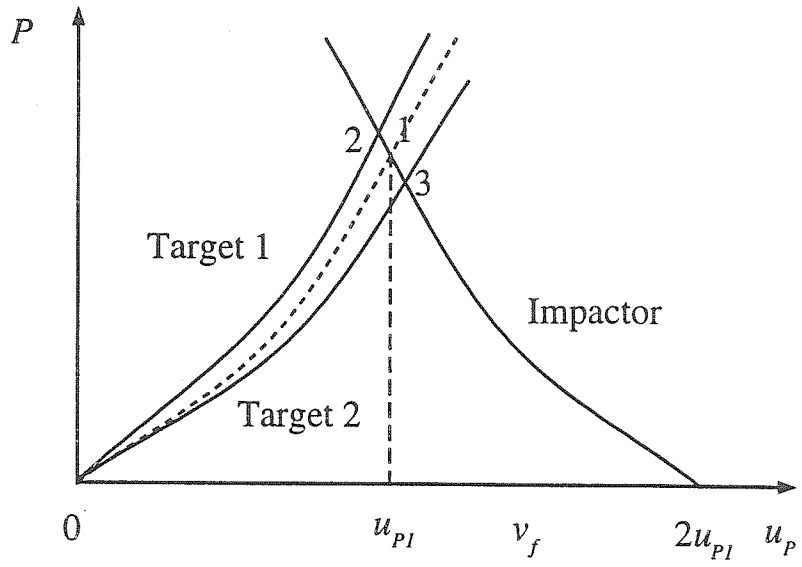

Figure B.2: Impedance match solutions between a pre-shocked impactor and two targets 1 and 2, one with lower impedance (solution 3) and the other one with higher impedance (solution 2). The Hugoniot of the impactor is reflected about the vertical dashed line centered at the shock state (1) to obtain the solutions (2 and 3).

Figure B.2 is similar to an unshocked impactor impacting at $2u_{P1}$.

B.2 Release State

The simplest method of measuring release isentrope of materials is to carry out a series of buffer experiments in which a shock wave of a certain amplitude is allowed to interact with a series of low-impedance materials. This is the method we used for the solid fayalite release isentrope measurements.

Since the Hugoniot curves for the buffers are known, a simple measurement of shock velocity determines the Hugoniot shock state in the buffer and hence the target state along the release isentrope in the pressure-particle velocity plane. To obtain the corresponding pressure-volume or pressure-density path corresponding to the pressure-particle velocity trajectory, it is necessary to assume that the release isentrope is truly isentropic and that the pressure is a single-valued function of density. Assuming that pressure-particle velocity states are measured from the Hugoniot (P, u_P) state down to the zero pressure, free surface velocity, the specific volume along

the release isentrope is given by the Riemann integral formula [*Lyzenga and Ahrens*, 1978]:

$$V_r = V - \int_{u_P}^{u_{Pr}} \left(\frac{\partial u_P}{\partial P}\right)_S du_P, \tag{B.12}$$

where $V = \rho^{-1}$ is the Hugoniot volume, and V_r is the volume along the release path where the particle velocity is u_{Pr} and the pressure is P_r. In actual experiments, the partial derivative is approximated between u_P and u_{Pr}, and the last equation becomes:

$$V_r = V - \frac{(u_{Pr} - u_P)^2}{P_r - P}. \tag{B.13}$$

Appendix C Shock Temperature Calculation

Shock temperatures for γ-iron, solid and molten fayalite are calculated in the present study. The algorithm is presented in the following.

The shock-wave internal energy is given by:

$$E = \frac{1}{2} P_H (V_0 - V), \tag{C.1}$$

where P_H is the Hugoniot pressure, V_0 and V are initial and Hugoniot volumes respectively. This energy can also be written in comparison with isentropic compression energy E_S at the same volume V:

$$E = E_S + \frac{V(P_H - P_S)}{\gamma} + E_{TR}, \tag{C.2}$$

where P_S is the isentropic pressure, E_{TR} takes in account possible internal energy changes associated with phase changes between the initial, reference pressure state and the Hugoniot state, and γ is the Grüneisen parameter:

$$\gamma = V \left(\frac{\partial P}{\partial E} \right)_V. \tag{C.3}$$

A commonly used relationship for volume dependence for γ is [*Anderson*, 1979]:

$$\gamma = \gamma_0 \left(\frac{V}{V_0} \right)^q \tag{C.4}$$

where γ_0 is the reference Grüneisen parameter, and q is found to be between 0.8 and 2.2 for the lower mantle, and a value 1.3 (average) for metals and alkali halides

[*Poirier*, 1991]. γ_0 is given by:

$$\gamma_0 = \frac{\alpha_0 K_{0S}}{\rho_0 C_{P0}} = \frac{\alpha_0 K_{0T}}{\rho_0 C_{V0}}. \tag{C.5}$$

Solving for P_H from Equations C.1 and C.2 yields:

$$P_H = \frac{2(P_S V/\gamma - E_S - E_{TR})}{V(1+2/\gamma) - V_0}. \tag{C.6}$$

If P_S is given by the Murnaghan equation [*Poirier*, 1991]:

$$P_S(V) = \frac{K_{0S}}{K'_{0S}}\left[\left(\frac{V_0}{V}\right)^{K'_{0S}} - 1\right], \tag{C.7}$$

then

$$\begin{aligned} E_S(V) &= -\int_{V_0}^{V} P_S(V)dV \\ &= \frac{K_{0S}}{K'_{0S}}\left\{\frac{V_0}{K'_{0S}-1}\left[\left(\frac{V_0}{V}\right)^{K'_{0S}-1} - 1\right] + (V - V_0)\right\}. \end{aligned} \tag{C.8}$$

The Murnaghan equation assumes that the isentropic bulk modulus, K_S, is a linear function of pressure:

$$K_S = K_{0S} + K'_{0S}P, \tag{C.9}$$

where K_{0S} is the zero (ambient) pressure bulk modulus, and

$$K'_{0S} \equiv (\partial K_S/\partial P)_S|_{P=0}. \tag{C.10}$$

The temperature along the isentrope is given by:

$$T_S = T_0 \exp\left[-\int_{V_0}^{V}\left(\frac{\gamma}{V}\right)dV\right]. \tag{C.11}$$

The Hugoniot temperature is then:

$$T_H = T_S + \frac{V(P_H - P_S)}{\gamma C_V}, \tag{C.12}$$

where C_V is the specific heat at constant volume and high pressure.

Appendix D Publications

A list of abstracts of my publications:

1. Tabosa, J. W. R., G. Chen, Z. Hu, R. B. Lee, and H. J. Kimble, Nonlinear spectroscopy of cold atoms in a spontaneous-force optical trap, *Phys. Rev. Lett., 66,* 3245-3248, 1991: Probe-wave amplification and absorption spectra are reported for cesium atoms cooled and confined in a Zeeman-shift spontaneous-force optical trap. Novel spectral features are observed with narrow frequency widths and with single-pass gain of 20mechanical consequence of optical gain and is investigated as a possible means for optical implosion of a trapped sample.

2. Chen, G. Q., J. A. Tyburczy, and T. J. Ahrens, Shock-induced devolatilization of calcium-sulfate and implications for K-T extinctions, *Earth Planet. Sci. Lett., 128,* 615-628, 1994:

   The devolatilization of calcium sulfate, which is present in the target rock of the Chicxulub, Mexico, impact structure, and dispersal in the stratosphere of the resultant sulfuric acid aerosol have been suggested as a possible mechanism for the Cretaceous-Tertiary extinctions [*Brett*, 1992; *Sigurdsson et al.*, 1992]. We measured the amount of SO_2 produced from two shock-induced devolatilization reactions of calcium sulfate up to 42 GPa in the laboratory:

   $$CaSO_4 + SiO_2 \longrightarrow CaSiO_3 + SO_3 \uparrow$$

   $$CaSO_4 \longrightarrow CaO + SO_2 \uparrow + \tfrac{1}{2}\, O_2 \uparrow$$

   We found both to proceed to a much lower extent than calculated by equilibrium thermodynamic calculations. Reaction products are found to be $\sim 10^{-2}$

times those calculated for equilibrium. Upon modeling quantity of sulfur oxides degassed into the atmosphere from shock devolatilization of $CaSO_4$ in the Chicxulub lithographic section, the resulting 6×10^{15} to 2×10^{16} g (in sulfur mass) is lower by a factor of 10 to 100 than previous upper limit estimates; the related environmental stress arising from the resultant global cooling and fall out of acid rain is insufficient to explain the widespread K-T extinctions.

3. Chen, G. Q., T. J. Ahrens, and R. Hide, Hypervelocity impacts and magnetization of small bodies in the Solar-System, *Icarus, 115*, 86-96, 1995:

   The observed magnetism of asteroids such as Gaspra and Ida (and other small bodies in the solar system including the Moon and meteorites) may have resulted from an impact-induced shock wave producing a thermodynamic state in which iron-nickel alloy, dispersed in a silicate matrix, is driven from the usual low-temperature, low-pressure, α, kaemacite, phase to the paramagnetic, ϵ (hcp), phase. The magnetization was acquired upon rarefaction and reentry into the ferromagnetic, α, structure. The degree of re-magnetization depends on the strength of the ambient field, which may have been associated with a solar-system-wide magnetic field. A transient field induced by the impact event itself may have resulted in a significant, or possibly, even a dominant contribution, as well. The scaling law of Housen *et al.* (1991) for catastrophic asteroid impact disaggregation imposes a constraint on the degree to which small planetary bodies may be magnetized and yet survive fragmentation by the same event. Our modeling results show it is possible Ida was magnetized when a large impact fractured a 125±22 km-radius proto-asteroid to form the Koronis family. Similarly, we calculate that Gaspra could be a magnetized fragment of a 45±15 km-radius proto-asteroid.

4. Chen, G. Q. and T. J. Ahrens, Equations of state of α-iron, ϵ-iron and liquid-iron and iron's melting curve - Thermodynamic calculations, *Geophys. Res. Lett., 22,* 21-24, 1995:

   The melting curve between ϵ and liquid iron (100GPa$< P <$300GPa) has been

derived by computing Gibbs free energies at high pressures and high temperatures from equations of state of the α, ϵ and liquid phases. The most uncertainty lies in the equation of state (EOS) of the ϵ phase. By comparing the calculations to experimental data, the internal thermodynamic consistency of the three phases are examined. The best fits to the melting curves of *Boehler* [1993] and *Williams et al.* [1987] can be obtained with lower bulk moduli than determined by static compression. Using available equations of state of the iron phases, our calculations indicate that if sub-solidus iron is of the ϵ phase, Boehler's melting curve is thermodynamically more consistent than Williams et al.'s. The problem is complicated by the possible existence of a new phase between the ϵ and the liquid fields.

5. Chen, G. Q. and T. J. Ahrens, High-pressure melting of iron - New experiments and calculations, *Philosophical Transactions of the Royal Society of London, Serie A, Mathematical, Physical and Engineering Sciences, 354*, 1251-1263, 1996:

   The melting curve of ϵ-iron in the pressure range of 100 GPa to 300 GPa has been derived by computing Gibbs free energies at high pressures and high temperatures from equation-of-states (EOS) of the α-, ϵ- and liquid-phases. Our calculations indicate the melting curve of iron is very sensitive to the EOS of both the solid (ϵ) and melt phase. Optimal EOS parameters for ϵ-iron are presented as well as new data for sound velocities in γ and liquid-phases. The latter provides a value for the Grüneisen parameter for liquid iron of 2.55 at 9.7 Mg/m^3 at a pressure of 74 GPa.

   Preliminary shock-wave experiments on pure iron preheated to 1300°C were conducted in 17–74 GPa range. Melting was observed in the highest pressure (74 GPa) experiment. This result supports our theoretically derived melting curve which is close to those measured by *Boehler* [1993] and *Saxena et al.* [1993].

6. Chen, G. Q. and T. J. Ahrens, Erosion of terrestrial planet atmosphere by surface motion after a large impact, *Phys. of the Earth and Planet. Inter., 100,*

21-26, 1997:

The history of atmosphere accretion has a large significance in the evolution of the Earth and other planets. Here we present a quantitative analysis of the Earth's response to large impacts (in the 10^{32}–10^{38} erg energy range), and the resulting atmosphere loss due to the global radial surface motion. Our results show that it is possible to deplete the Earth's atmosphere via this mechanism in very large (lunar-sized, $\sim 10^{38}$ erg) impacts.

7. Chen, G. Q., T. J. Ahrens, W. Yang, and J. K. Knowles, Effect of irreversible phase change on shock-wave propagation, *J. Mech. Phys. Solids*, 1997, submitted:

   New release adiabat data for vitreous GeO_2 are reported up to ~25 GPa using the VISAR technique. Numerical modeling of release isentropic waves is consistent with phase change induced increase in zero-pressure density from 3.7 to 6.3 Mg/m^3 starting at ~8 GPa. The first release adiabat data for SiO_2 (fused quartz) are presented (obtained with immersed foil technique). Above 10 GPa, the SiO_2 release adiabats are steeper than the reflected Hugoniot, indicating the presence of an irreversible phase transition (to a stishovite-like phase). We simulate propagation of a shock-waves in GeO_2, in spherical and planar symmetries, and find enhanced attenuation for shock pressures (p) above the phase change initiation pressure (8 GPa). The pressure from a spherical source decays with propagation radius r, $p \sim r^x$, where x is the decay coefficient. Modeling hysteresis of the phase change gives $x = -2.71$, whereas without the phase change, $x = -1.15$. An analytical model is also given.

8. Anderson, W. W., W. Yang, G. Q. Chen, and T. J. Ahrens, Shock wave equation of state of rhyolite, *Geophys. J. Intl.*, 1997, to be submitted:

   We have obtained new shock wave equation of state and release adiabat data for rhyolite. These data are combined with those of Swegle [1989, 1990] to give an experimental Hugoniot which is described by $U_S = 2.53(\pm 0.08) + 3.93(\pm 0.37)u_p$

for $u_p < 0.48$ km/s, $U_S = 3.85(\pm 0.05) + 0.65(\pm 0.03)u_p$ for $0.48 \leq u_p < 2.29$ km/s, $U_S = 1.52(\pm 0.08) + 1.67(\pm 0.02)u_p$ for $2.29 \leq u_p < 4.37$ km/s, and $U_S = 3.40(\pm 0.34) + 1.24(\pm 0.06)u_p$ for $u_p > 4.37$ km/s, with $\rho_0 = 2.357 \pm 0.052$ Mg/m^3. We suggest that the Hugoniot data give evidence of three distinct phases–both low and high pressure solid phases and, possibly, a dense molten phase. Equation of state parameters for these phases are $\rho_0 = 2.494 \pm 0.002$ Mg/m^3, $K_{S0} = 37 \pm 2$ GPa, $K'_S = 6.27 \pm 0.25$, and $\gamma = 1.0(V/V_0)$ for the low pressure solid phase, $\rho_0 = 3.834 \pm 0.080$ Mg/m^3, $K_{S0} = 128 \pm 20$ GPa, $K'_S = 3.7 \pm 1.4$, and $\gamma = 1.5 \pm 0.5$ for the solid high pressure phase, and $\rho_0 = 3.71 \pm 0.10$ Mg/m^3, $K_{S0} = 127 \pm 25$ GPa, $K'_S = 2.1 \pm 1.0$, and $\gamma = 1.5 \pm 1.0$ for the high density liquid. The mixed phase portions of the Hugoniot are modeled by mass weighted averages of the volumes of the end member Hugoniot states. The fraction of a given end member phase is assumed to vary linearly with pressure within the mixed-phase region. These regions cover the ranges of 9–34 GPa for the low pressure-high pressure solid mixed phase region and 90–120 GPa for the high pressure solid-liquid mixed phase region. The equation of state parameters for the three phases allow calculation of both shock and release states. Calculated release paths from high pressure states suggest that the material remains in the high pressure solid phase upon release. Release paths from the high pressure solid and liquid fall above the Hugoniot until the Hugoniot enters the low pressure-high pressure mixed phase region, when the release paths then cross the Hugoniot and fall below, ending at significantly higher zero-pressure densities than that of the low pressure phase. The low pressure release paths, as expected, fall very close to the Hugoniot.

Bibliography

Agee, C. B., A new look at differentiation of the earth from melting experiments on Allende meteorite, *Nature*, *346*, 834–837, 1990.

Agee, C. B., Isothermal compression of molten Fe_2SiO_4, *Geophys. Res. Lett.*, *19*, 1169–1172, 1992a.

Agee, C. B., Thermal-expansion of molten FE_2SIO_4 at high-pressure, *Geophys. Res. Lett.*, *19*, 1172–1176, 1992b.

Agee, C. B., Petrology of the mantle transition zone, *Annu. Rev. Earth and Planet. Sci.*, *21*, 19–41, 1993.

Agee, C. B., and D. Walker, Mass balance and phase density constraints on early differentiation of chondritic mantle, *Earth Planet. Sci. Lett.*, *90*, 144–156, 1988a.

Agee, C. B., and D. Walker, Static compression and olivine flotation in ultrabasic silicate liquid, *J. Geophys. Res.*, *93*, 3437–3449, 1988b.

Agee, C. B., and D. Walker, Olivine flotation in mantle melt, *Earth Planet. Sci. Lett.*, *114*, 315–324, 1993.

Ahrens, T. J., Shock wave techniques for geophysics and planetary physics, in *Methods of Experimental Physics*, chap. 6, pp. 185–235, Academic Press, Inc., Orlando, 1987, Vol. 24, Part A.

Akimoto, S., E. Komada, and I. Kushiro, Effect of pressure on the melting of olivine and spinel polymorph of Fe_2SiO_4, *J. Geophys. Res.*, *72*, 679–686, 1967.

Akimoto, S., T. Suzuki, T. Yagi, and O. Shimomura, Phase diagram of iron determined by high-pressure/temperature X-ray diffraction using synchrotron radia-

tion, in *High-Pressure Research in Mineral Physics*, edited by M. Manghnani and Y. Syono, pp. 149–154, American Geophysical Union, Washington, D.C., 1987.

Anderson, O. L., Evidence supporting the approximation $\gamma\rho$=const for the Grüneisen parameter of the Earth's lower mantle, *J. Geophys. Res.*, *84*, 3537–3542, 1979.

Anderson, O. L., Imperfections of the 1993 phase diagram of iron, in *High Pressure Science and Technology-1993*, edited by S. C. Schmidt, J. W. Shaner, G. A. Samara, and M. Ross, pp. 907–910, American Institute of Physics Press, New York, 1994.

Anderson, W. W., and T. J. Ahrens, An equation of state for liquid iron and implications for the Earth's core, *J. Geophys. Res.*, *99*, 4273–4284, 1994.

Anderson, W. W., and T. J. Ahrens, Shock temperatures and melting in iron sulfides at core pressures, *J. Geophys. Res.*, *101*, 5627–5642, 1996.

Andrews, D. J., Equation of state of the alpha and epsilon phases of iron, *J. Phys. Chem. Solids*, *34*, 825–840, 1973.

Asay, J. R., and L. C. Chhabildas, Determination of the shear strength of shock-compressed 6061-T6 aluminum, in *Shock Waves and High Strain-Rate Phenomena in Metals*, edited by M. Meyers and L. E. Murr, pp. 417–431, Plenum, New York, 1981.

Asay, J. R., L. C. Chhabildas, G. I. Kerley, and T. G. Trucano, High pressure strength of shocked aluminum, in *Shock Compression in Condensed Matter – 1985*, edited by Y. M. Gupta, pp. 145–149, Plenum, New York, 1986.

Bancroft, D., E. L. Peterson, and S. Minshall, Polymorphism of iron at high pressure, *J. Appl. Phys.*, *27*, 291–298, 1956.

Barker, L. M., and R. E. Hollenbach, Shock-wave studies of PMMA, fused silica, and sapphire, *J. Appl. Phys.*, *41*, 4208–4226, 1970.

Barker, L. M., and R. E. Hollenbach, Laser interferometer for measuring high velocities of any reflecting surface, *J. Appl. Phys.*, *43*, 4669–4675, 1972.

Barker, L. M., and R. E. Hollenbach, Shock wave study of the $\alpha \leftrightarrow \epsilon$ phase transition in iron, *J. Appl. Phys.*, *45*, 4872–4887, 1974.

Bass, J. D., Elasticity of minerals, glasses and melts, in *Mineral Physics & Crystallography: A Handbook of Physical Constants*, edited by T. J. Ahrens, vol. 1, pp. 45–63, American Geophysical Union, Washington, D. C., 1995.

Bass, J. D., B. Svendsen, and T. J. Ahrens, The temperatures of shock-compressed iron, in *High Pressure Research in Mineral Physics*, edited by M. Manghnani and Y. Syono, pp. 393–402, American Geophysical Union, Washington, D.C., 1987.

Bassett, W. A., and L. C. Ming, Disproportionation of Fe_2SiO_4 to $2FeO+SiO_2$ at pressures up to 250 kbar and temperatures up to 3000°C, *Phys. of the Earth and Planet. Inter.*, *6*, 154–160, 1972.

Belonoshko, A. B., Atomic simulation of shock wave-induced melting in argon, *Science*, *275*, 955–957, 1997.

Besson, J. M., and M. Nicol, An equation of state of γ-Fe and some insights about magnetoelastic effects on measurements of the α-γ-ϵ triple point and other transitions, *J. Geophys. Res.*, *95*, 21717–21720, 1990.

Boehler, R., Adiabats of quartz, coesite, olivine, and magnesium oxide to 50 kbar and 1000 k and the adiabatic gradient in the Earth's mantle, *J. Geophys. Res.*, *87*, 5501–5506, 1982.

Boehler, R., Temperatures in the Earth's core from melting-point measurements of iron at high static pressures, *Nature*, *363*, 534–536, 1993.

Boehler, R., and J. Ramakrishnan, Experimental results on the pressure dependence of the Grüneisen parameter: a review, *J. Geophys. Res.*, *85*, 6996–7002, 1980.

Boehler, R., J. M. Besson, M. Nicol, M. Nielsen, J. P. Itie, G. Weill, S. Johnson, and F. Grey, X-ray diffraction of γ-iron at high temperatures and pressures, *J. Appl. Phys.*, *65*, 1795–1797, 1989.

Boness, D. A., J. M. Brown, and A. K. McMahan, The electronic thermodynamics of iron under Earth core conditions, *Phys. of the Earth and Planet. Inter.*, *42*, 227–240, 1986.

Boness, D. A., J. M. Brown, and J. W. Shaner, Rarefaction velocities in shocked lead, in *Shock Waves in Condensed Matter 1987*, edited by S. C. Schmidt and N. C. Holmes, pp. 115–118, North-Holland Physics Publishing, Amsterdam, The Netherlands, 1988.

Bottinga, N., and D. F. Weill, Density of liquid silicate systems calculated from partial molar volumes of oxide components, *Am. J. Sci.*, *269*, 169–182, 1970.

Bottinga, Y., D. Weill, and P. Richet, Density calculations for silicate liquids. I. Revised method for aluminosilicate compositions, *Geochim. Cosmo. Acta*, *46*, 909–919, 1982.

Brown, J. M., and R. G. McQueen, The equation of state for iron and the Earth's core, in *High Pressure Research in Geophysics*, edited by S. Akimoto and M. H. Manghnani, pp. 611–623, Center for Academic Publications, Tokyo, 1982.

Brown, J. M., and R. G. McQueen, Phase transitions, Grüneisen parameter, and elasticity for shocked iron between 77 GPa and 400 GPa, *J. Geophys. Res.*, *91*, 7485–7494, 1986.

Brown, J. M., and J. W. Shaner, Rarefaction velocities in shocked tantalum and the high-pressure melting point, in *Shock Waves in Condensed Matter–1983*, edited by J. Asay, R. Graham, and G. K. Straub, pp. 91–94, Elsevier, New York, 1984.

Bukowinski, M. S. T., Quantum geophysics, *Annu. Rev. Earth Planet. Sci.*, *22*, 167–205, 1994.

Bundy, F. P., Pressure-temperature phase diagram of iron to 200 kbar, 900°C, *J. Appl. Phys.*, *36*, 616–620, 1965.

Duffy, T. S., Elastic properties of metals and minerals under shock compression, Ph.D. thesis, California Institute of Technology, Pasadena, CA, 1992.

Duffy, T. S., and T. J. Ahrens, Sound velocities at high-pressure and temperature and their geophysical implications, *J. Geophys. Res.*, *97*, 4503–4520, 1992.

Duffy, T. S., and T. J. Ahrens, Thermal expansion of mantle and core materials at very high pressures, *Geophys. Res. Lett.*, *20*, 1103–1106, 1993.

Duffy, T. S., and T. J. Ahrens, Dynamic response of molybdenum shock compressed at 1400°C, *J. Appl. Phys.*, *76*, 835–842, 1994a.

Duffy, T. S., and T. J. Ahrens, The temperature sensitivity of elastic-wave velocity at high-pressure: New results for molybdenum, *Geophys. Res. Lett.*, *21*, 473–476, 1994b.

Duvall, G. F., and G. R. Fowles, Shock waves, in *High Pressure Physics and Chemistry*, edited by R. S. Bradley, pp. 209–291, Academic Press, New York, 1963.

Dziewonski, A. M., and D. L. Anderson, Preliminary reference Earth model, *Phys. of the Earth and Planet. Inter.*, *25*, 297–356, 1981.

Falzone, A. J., and F. D. Stacey, Second-order elasticity theory: Explanation for the high Poisson's ratio of the inner core, *Phys. of the Earth and Planet. Inter.*, *21*, 371–377, 1980.

Finch, C. B., G. W. Clark, and O. C. Kopp, Czochralski growth of single-crystal fayalite under controlled oxygen fugacity conditions, *Amer. Mineral.*, *65*, 381–389, 1980.

Hemsing, W., Velocity-sensing interferometer (visar) modification, *Rev. Sci. Instrum.*, *50*, 73–78, 1979.

Herzberg, C. T., Magma density at high pressure Part 1: The effect of composition on the elastic properties of silicate liquids, in *Magmatic processes: Physicochemical*

principles, edited by B. Mysen, pp. 25–46, The Geochemical Society, University Park, Pennsylvania, 1987a.

Herzberg, C. T., Magma density at high pressure Part 2: A test of the olivine flotation hypothesis, in *Magmatic processes: Physicochemical principles*, edited by B. Mysen, pp. 47–58, The Geochemical Society, University Park, Pennsylvania, 1987b.

Hixson, R. S., M. A. Winkler, and M. L. Hodgdon, Sound speed and thermophysical properties of liquid iron and nickel, *Phys. Rev. B*, *42*, 6485–6491, 1990.

Holland, K. G., Phase changes and transport properties of geophysical materials under shock loading, Ph.D. thesis, California Institute of Technology, Pasadena, CA, 1997.

Hsu, L. C., Melting of fayalite up to 40 kilobars, *J. Geophys. Res.*, *72*, 4235–4244, 1967.

Huang, E., W. A. Bassett, and P. Tao, Pressure-temperature-volume relationship for hexagonal close packed iron determined by synchrotron radiation, *J. Geophys. Res.*, *92*, 8129–8135, 1987.

Jackson, W. E., J. M. de Leon, G. E. B. Jr., G. A. Waychunas, S. D. Conradson, and J. M. Combes, High-temperature XAS study of Fe_2SiO_4 liquid: Reduced coordination of ferrous iron, *Science*, *262*, 229–233, 1993.

Jeanloz, R., and T. J. Ahrens, Equations of state of FeO and CaO, *Geophys. J. R. astr. Soc.*, *62*, 505–528, 1980.

Jeanloz, R., and S. Morris, Temperature distribution in the crust and mantle, *Annu. Rev. Earth Planet. Sci.*, *14*, 377–415, 1986.

Jephcoat, A., and P. Olson, Is the inner core of the Earth pure iron?, *Nature*, *325*, 332–335, 1987.

Katahara, K. W., M. H. Manghnani, and E. S. Fisher, Pressure derivatives of the elastic moduli of BCC Ti-V-Cr, Nb-Mo, and Ta-W alloys, *J. Phys. F: Metal Phys.*, *9*, 773–790, 1979.

Kerley, G. I., Multiphase equation of state for iron, *Tech. Rep. SAND93-0027*, Sandia National Laboratories, Albuquerque, New Mexico, 1993.

Kubicki, J. D., and A. C. Lasaga, Molecular dynamics simulations of pressure and temperature effects on $MgSiO_3$ and Mg_2SiO_4 melts and glasses, *Phys. Chem. Miner.*, *17*, 661–673, 1991.

Kurz, W., and B. Lux, Die Schallgeswindigkeit von Eisen und Eisenlegierungen in festen und flüssigen Zustand, *High Temp. High Pressures*, *1*, 387–399, 1969.

Kusabiraki, K., and Y. Shiraishi, The infrared spectrum of vitreous fayalite, *J. Non Cryst. Solids*, *44*, 365–368, 1981.

Lange, R. A., and I. S. E. Carmichael, Densities of Na_2O-K_2O-CaO-MgO-FeO-Fe_2O_3-Al_2O_3-TiO_2-SiO_2 liquids: New measurements and derived partial molar properties, *Geochim. Cosmo. Acta*, *51*, 2931–2946, 1987.

Lide, D. R., *Handbook of Chemstry and Physics*, CRC Press, Boca Raton, Florida, 1993–1994, 74th edition.

Lindsley, D. H., Pressure-temperature relations in the system FeO-SiO_2, *Carnegie Inst. Wash. Yearb.*, *65*, 226–230, 1967.

Liu, L., and W. A. Bassett, *Elements, Oxides, Silicates: High-Pressure Phases with Implications for the Earth's Interior*, Oxford University Press, New York, 1986.

Lyzenga, G. A., and T. J. Ahrens, The relation between the shock-induced free-surface velocity and the postshock specific volume of solids, *J. Appl. Phys.*, pp. 201–204, 1978.

Lyzenga, G. A., T. J. Ahrens, and A. C. Mitchell, Shock temperatures of SiO_2 and their geophysical implications, *J. Geophys. Res.*, *88*, 2431–2444, 1983.

Manghnani, M. H., L. C. Ming, and N. Nakagiri, Investigation of the α-Fe $\leftrightarrow$ ϵ-Fe phase transition by synchrotron radiation, in *High-Pressure Research in Mineral Physics*, edited by M. Manghnani and Y. Syono, pp. 155–163, American Geophysical Union, Washington, D.C., 1987.

Mao, H. K., Y. Wu, L. C. Chen, J. F. Shu, and A. P. Jephcoat, Static compression of iron to 300 GPa and $Fe_{0.8}Ni_{0.2}$ alloy to 260 GPa: Implications for composition of the core, *J. Geophys. Res.*, *95*, 21737–21742, 1990.

Marsh, S. P., ed., *LASL Shock Hugoniot Data*, University of California Press, Berkeley, California, 1980.

Matsui, M., Computer simulation of the structural and physical properties of iron under ultra high pressures and high temperatures, *Central Core of the Earth*, *2*, 79–82, 1992.

Matsui, Y., and K. Kawamura, Instantaneous structure of an $MgSiO_3$ melt simulated by molecular dynamics, *Nature*, *285*, 648–649, 1980.

Matsui, Y., and K. Kawamura, Computer simulation of structures of silicate melts and glasses, in *Materials Science of the Earth's Interior*, edited by I. Sunagawa, pp. 3–23, Terra Scientific, Tokyo, 1984.

Matsui, Y., K. Kawamura, and Y. Syono, Molecular dynamics calculations applied to silicate systems: Molten and vitreous $MgSiO_3$ and Mg_2SiO_4 under low and high pressures, in *High Pressure Research in Geophysics*, edited by S. Akimoto and M. H. Manghnani, pp. 511–524, Center for Academic Publications, Tokyo, 1982.

McQueen, R. G., S. P. Marsh, and J. N. Fritz, Hugoniot equation of state of twelve rocks, *J. Geophys. Res.*, *72*, 4999–5036, 1967.

McQueen, R. G., S. P. Marsh, J. W. Taylor, J. N. Fritz, and W. J. Carter, The equation of state of solids from shock wave studies, in *High-Velocity Impact Phenomena*, edited by R. Kinslow, chap. 7, pp. 293–417, Academic Press, New York, 1970.

Melson, W. G., and G. Thompson, Petrology of a transformation fault zone and adjacent ridge segments, *Philos. Trans. Royal Soc. London Ser. A*, *268*, 423–441, 1971.

Miller, G. H., and E. G. Puckett, Edge effects in molybdenum-encapsulated molten silicate shock wave targets, *J. Appl. Phys.*, *75*, 1426–1434, 1994.

Miller, G. H., T. J. Ahrens, and E. M. Stolper, The equation of state of molybdenum at 1400°C, *J. Appl. Phys.*, *63*, 4469–4475, 1988.

Miller, G. H., E. M. Stolper, and T. J. Ahrens, The equation of state of a molten komatiite 1. shock-wave compression to 36 GPA, *J. Geophys. Res.*, *96*, 11831–11848, 1991a.

Miller, G. H., E. M. Stolper, and T. J. Ahrens, The equation of state of a molten komatiite 2. application to komatiite petrogenesis and the Hadean mantle, *J. Geophys. Res.*, *96*, 11849–11864, 1991b.

Mirward, P. W., and G. C. Kennedy, The Curie point and the α-γ transition of iron to 53 kbar – A reexamination, *J. Geophys. Res.*, *84*, 656–658, 1979.

Mitchell, A. C., and W. J. Nellis, Shock compression of aluminum, copper, and tantalum, *J. Appl. Phys.*, *52*, 3363–3374, 1981.

Nasch, P. M., M. H. Manghnani, and R. A. Secco, Sound-velocity measurements in liquid-iron by ultrasonic interferometry, *J. Geophys. Res.*, *99*, 4285–4291, 1994.

Ohtani, E., Melting relation of Fe_2SiO_4 up to about 200 kbar, *J. Phys. Earth*, *27*, 189–208, 1979.

Ohtani, E., F. Taulelle, and C. A. Angell, Al^{3+} coordination changes in liquid aluminosilicates under pressure, *Nature*, *314*, 78–81, 1985.

Omel'chenko, A. V., V. I. Soshnikov, and E. I. Estrin, Effect of high pressures on the Curie point and $\alpha \leftrightarrow \gamma$ transformation point of iron, *Fiz. metal. metalloved*, *28*, 77–83, 1969.

Poirier, J. P., *Introduction to the Physics of the Earth's Interior*, Cambridge University Press, Cambridge, U.K., 1991.

Rigden, S. M., T. J. Ahrens, and E. M. Stolper, Densities of liquid silicates at high-pressures, *Science*, *226*, 1071–1074, 1984.

Rigden, S. M., T. J. Ahrens, and E. M. Stolper, Shock compression of molten silicate: Results for a model basaltic composition, *J. Geophys. Res.*, *93*, 367–382, 1988.

Rigden, S. M., T. J. Ahrens, and E. M. Stolper, High-pressure equation of state of molten anorthite and diopside, *J. Geophys. Res.*, *94*, 9508–9522, 1989.

Rivers, M. L., Ultrasonic studies of silicate liquids, Ph.D. thesis, Univ. of Calif., Berkeley, 1985.

Rivers, M. L., and I. S. E. Carmichael, Ultrasonic studies of silicate melts, *J. Geophys. Res.*, *92*, 9247–9270, 1987.

Robie, R. A., B. S. Hemingway, and J. R. Fisher, Thermodynamic properties of minerals and related substances at 298.15k and 1 bar (10^5 pascals) pressure and at higher temperatures, *U. S. Geol. Survey Bull.*, p. 1452, 1979.

Rowan, L. R., I. Equation of state of molten Mid-Ocean Ridge basalt; II. Structure of Kilauea volcano, Ph.D. thesis, California Institute of Technology, Pasadena, California, 1993.

Ruoff, A. L., Linear shock-velocity-particle-velocity relationship, *J. Appl. Phys.*, *38*, 4976–4980, 1967.

Sato, M., An electrochemical method of oxygen fugacity control of furnace atmosphere for mineral syntheses, *Am. Mineral.*, *55*, 1424–1431, 1970.

Saxena, S. K., and L. S. Dubrovinsky, Detecting phases of iron, *Science*, *275*, 94–96, 1997.

Saxena, S. K., G. Shen, and P. Lazor, Experimental evidence for a new iron phase and implications for Earth's core, *Science*, *260*, 1312–1314, 1993.

Saxena, S. K., G. Shen, and P. Lazor, Temperatures in Earth's core based on melting and phase transformation experiments on iron, *Science*, *264*, 405–407, 1994.

Saxena, S. K., L. S. Dubrovinsky, P. Häggkvist, Y. Cerenius, G. Shen, and H. K. Mao, Synchrotron X-ray study of iron at high-pressure and temperature, *Science*, *269*, 1703–1704, 1995.

Saxena, S. K., L. S. Dubrovinsky, and P. Häggkvist, X-ray evidence for the new phase beta-iron at high-temperature and high-pressure, *Geophys. Res. Lett.*, *23*, 2441–2444, 1996.

Shankland, T. J., and J. M. Brown, Homogeneity and temperatures in the lower mantle, *Phys. of the Earth and Planet. Inter.*, *38*, 51–58, 1985.

Shiraishi, Y., K. Ikeda, A. Tamura, and T. Saito, On the viscosity and density of the molten FeO-SiO_2 system, *Trans. Jap. Inst. Metal.*, *19*, 264–274, 1978.

Slater, J. C., and N. H. Frank, *Electromagnetism*, Dover Publications, Inc., New York, 1969.

Smyth, J. R., and T. C. McCormick, Crystallographic data for minerals, in *Mineral Physics & Crystallography: A Handbook of Physical Constants*, edited by T. J. Ahrens, vol. 2, pp. 1–17, American Geophysical Union, Washington, D. C., 1995.

Song, X., and T. J. Ahrens, Pressure-temperature range of reactions between liquid iron in the outer core and mantle silicates, *Geophys. Res. Lett.*, *21*, 153–156, 1994.

Stixrude, L., and R. E. Cohen, Constraints on the crystalline structure of the inner core: Mechanical instability of bcc iron at high pressure, *Geophys. Res. Lett.*, *22*, 125–128, 1995.

Stolper, E. M., and T. J. Ahrens, On the nature of pressure-induced coordination changes in silicate melts and glasses, *Geophysical Research Letters*, *14*, 1231–1233, 1987.

Stolper, E. M., D. Walker, B. H. Hager, and J. F. Hays, Melt segregation from partially molten source regions: The importance of melt density and source region size, *J. Geophys. Res.*, *86*, 6261–6267, 1981.

Strong, H. M., R. E. Tuff, and R. E. Hanneman, The iron fusion curve and γ-δ-l triple point, *Metal. Trans.*, *4*, 2657–2661, 1973.

Sur, S., and T. F. Cooney, Electron paramagnetic resonance study of iron (III) and manganese (II) in the glassy and crystalline environments of synthetic fayalite and tephroite, *Phys. Chem. Miner.*, *16*, 693–696, 1989.

Thomas, J. F., Third-order elastic constants of aluminum, *Phys. Rev.*, *175*, 955–962, 1968.

Touloukian, Y. S., ed., *Thermophysical Properties of high temperature solid material*, vol. 4, pp. 1243–1246, The MacMillan Company, New York, 1967.

Touloukian, Y. S., ed., *Thermophysical properties of matter*, vol. 12, pp. 157–158, Plenum, New York, 1970.

Tsu, Y., K. Takano, and Y. Shiraishi, The velocities of unltrasound in molten iron, cobalt, and nickel (in Japanese), *Bull. Res. Inst. Miner. Dressing Metall. Tohoku Univ.*, *41*, 1–8, 1985.

Vassiliou, M. S., and T. J. Ahrens, Limited aperture light-source streak photography, *Rev. Sci. Ins.*, *53*, 108–109, 1982.

Waff, H., Pressure-induced coordination changes in magmatic liquids, *Geophys. Res. Lett.*, *2*, 193–196, 1975.

Wang, G., An empirical expression of elastic sound speed of materials at high pressure, *Chinese J. High Pressure Phys.*, *2*, 92–95, 1988.

Waseda, Y., and J. M. Toguri, The structure of molten binary silicate systems CaO-SiO_2 and MgO-SiO_2, *Met. Trans.*, *8B*, 563–568, 1977.

Watt, J. P., G. F. Davies, and R. J. O'Connell, The elastic properties of composite materials, *Rev. Geophys. Space Phys.*, *14*, 541–563, 1976.

Whirley, R. G., and B. E. Engelmann, DYNA2D–A nonlinear, explicit, two-dimensional finite element code for solid mechanics–User manual, *Tech. Rep. UCRL-MA-110630*, Lawrence Livermore National Laboratory, Livermore, CA, 1992.

Williams, Q., and T. F. Cooney, Cation field effects on orthosilicate glass vibrations, *Am. Mineral.*, *95*, 19299–19310, 1990.

Williams, Q., and E. J. Garnero, Seismic evidence for partial melt at the base of Earth's mantle, *Science*, *273*, 1528–1530, 1996.

Williams, Q., R. Jeanloz, J. Bass, B. Svendsen, and T. J. Ahrens, The melting curve of iron to 250 gigapascals: A constraint on the temperature at the Earth's center, *Science*, *236*, 181–182, 1987.

Williams, Q., E. Knittle, R. Reichlin, S. Martin, and R. Jeanloz, Structural and electronic-properties of Fe2SiO4-fayalite at ultrahigh pressures - amorphization and gap closure, *J. Geophys. Res.*, *95*, 21549–21563, 1990.

Williams, Q., E. Knittle, and R. Jeanloz, The high-pressure melting curve of iron - a technical discussion, *J. Geophys. Res.*, *96*, 2171–2184, 1991.

Woodhouse, J. H., and A. M. Dziewonski, Mapping the upper mantle – three-dimensional modeling of Earth structure by inversion of seismic waveforms, *J. Geophys. Res.*, *89*, 5953–5986, 1984.

Yang, W. B., and T. J. Ahrens, Impact jetting of geological-materials, *Icarus*, *116*, 269–274, 1995.

Yin, C. D., M. Okuno, H. Morikawa, and F. Marumo, Structure analysis of $MgSiO_3$ glass, *J. Non Cryst. Solids*, *55*, 131–141, 1983.

Yoo, C. S., N. C. Holmes, M. Ross, D. J. Webb, and C. Pike, Shock temperatures and melting of iron at Earth core conditions, *Phys. Rev. Lett.*, *70*, 3931–3934, 1993.

Yoo, C. S., J. Akella, A. J. Campbell, H. K. Mao, and R. J. Hemley, Phase diagram of iron by in situ X-ray diffraction: Implications for Earth's core, *Science*, *270*, 1473–1475, 1995.